8-2021

Measurements of Radiation Pressure on Diffractive Films

Ying-Ju Lucy Chu
yxc8175@rit.edu

Measurements of Radiation Pressure on Diffractive Films

by

Ying-Ju Lucy Chu

B.S. National Cheng Kung University, Taiwan, 2013
M.S. Biomedical Engineering, 2015

A dissertation submitted in partial fulfillment of the
requirements for the degree of Doctor of Philosophy
in the Chester F. Carlson Center for Imaging Science
College of Science
Rochester Institute of Technology

[August, 2021]

Signature of the Author _____

Accepted by _____
Coordinator, Ph.D. Degree Program Date

CHESTER F. CARLSON CENTER FOR IMAGING SCIENCE
COLLEGE OF SCIENCE
ROCHESTER INSTITUTE OF TECHNOLOGY
ROCHESTER, NEW YORK

CERTIFICATE OF APPROVAL

Ph.D. DEGREE DISSERTATION

The Ph.D. Degree Dissertation of Ying-Ju Lucy Chu
has been examined and approved by the
dissertation committee as satisfactory for the
dissertation required for the
Ph.D. degree in Imaging Science

_____
[Dr. Grover Swartzlander], Dissertation Advisor

_____
[Dr. Karl Hirshman], External Chair

_____
[Dr. Zoran Ninkov]

_____
[Dr. Mihail Barbosu]

_____
Date

Measurements of Radiation Pressure on Diffractive Films

by

Ying-Ju Lucy Chu

Submitted to the
Chester F. Carlson Center for Imaging Science
in partial fulfillment of the requirements
for the Doctor of Philosophy Degree
at the Rochester Institute of Technology

Abstract

One of the few ways to reach distant stars is by radiation pressure, in which photon momentum is harnessed from free sunlight or extraordinarily powerful laser systems. Large but low mass light-driven sails reflect photons and transfer momentum to the sailcraft, providing large velocity from continuous acceleration. Over the past decade, demonstrative reflective light sail missions were enabled by cost-efficient small satellites and the emerging private space economy. The maneuver of these metal-coated polyimide films is mechanically cumbersome because the sail must be rapidly tilted towards and away from the sun line during navigation. Modern diffractive films such as high-efficiency single-order gratings, liquid crystal cycloidal diffractive wave-plates, and meta-material gratings may provide enhanced control schemes with radiation pressure tangential to the sail surface. The potential to replace motorized control components with all-optical components also offers a reduction in mass and the risk of mission failure.

Before spending considerable resources sending a rocket to deploy a solar sail, it must be verified that the sail will behave as expected in a lab on Earth. This is challenging since Earths gravity, electro-static forces, thermal effects, and environment vibrations

exceed the relatively weak effects of radiation pressure. In this dissertation, we designed and constructed an opto-mechanical torsional pendulum in a vacuum environment that measures radiation pressure on diffraction films with sub-nano-Newton precision. With the system, we observed a large component of force parallel to the surface of a diffraction grating owing to grating momentum. Furthermore, we proposed, designed, and validated Diffractive Beam-Rider structures that enable spatially varying forces to pull and align the sailcraft to the beam. We parametrically cooled the turbulence on the Beam-Rider, which demonstrates its potential for implementation on a laser sail. This experimental stability verification was performed on a centimeter-sized bi-grating and a diffractive axicon with one and two-dimensional restoring force, respectively.

Acknowledgements

I thank my advisor, Prof. Grover Swartzlander, who lead, guided, and stood by me through this journey pursuing the unknown. He has shown me how to make a wild dream come true using hard and soft skills, confidence and perseverance.

I thank my lab mates Prateek Srivastava, Jacob Wirth, Alexandra Artusio-Glimpse, Xiaopeng Peng, and the heartwarming people throughout the whole RIT Center for Imaging Science department, Semiconductor & Microsystems Fabrication Laboratory (SMFL) for support on research and life in and out of the laboratory.

I thank and Taiwanese student society, RIT SPIE/OSA student chapter (SPIE: The International Society of Optics and Photonics, OSA: The Optical Society) which enriched the student activities in my life as a Taiwanese student at RIT.

Part 1. Measurements of Radiation Pressure on a Diffraction Grating We thank Peter, Lihong, and Eric Jansson (Hockessin,Delaware) for guidance and the hospitable use of their laboratory, and Sydor Optics (Rochester, New York) for thinning and dicing the diffraction grating. This research was partially supported by the National Science Foundation under the Directorate for Engineering (ENG) (Grant No. ECCS-1309517), the NASA Innovative Advanced Concepts Program (NIAC)
(Grant No. 80NSSC18K0867), and the Taiwanese Ministry of Education Study Abroad Scholarship (Grant No. 1061110054).

Part 2. Experimental Verification of a Bi-grating Beam-Rider We thank Nelson Tabirian for collaborating in the process of design and fabrication the beam-rider sample. We thank Prateek Srivastava on the co-development on theories of the Diffractive Beam-Rider. We thank the RIT Semiconductor & Microsystems Fabrication Laboratory (SMFL) for providing lab space on low vibration floor. This research was supported by NASA Innovative Advanced Concepts Program (NIAC) (Grant No. 80NSSC18K0867) and the

Taiwanese Ministry of Education Study Abroad Scholarship (Grant No. 1061110054).

Part 3. Axicon Verification of a Bi-grating Beam-Rider We thank Monjurul Meem, Rajesh Menon, on the axicon sample design and fabrication, and Prateek Srivastava on the theories of an axicon beam-rider. We thank the RIT Semiconductor & Microsystems Fabrication Laboratory (SMFL) for providing lab space on low vibration floor. This research was supported by NASA Innovative Advanced Concepts Program (NIAC) (Grant No. 80NSSC18K0867) and the Breakthrough Starshot program.

Dedicated to..

The nothingness and everythingness of the universe.

The excitement and eagerness to create and the expand knowledge.

The valuable people and events that I encountered along this journey.

Contents

List of Figures

List of Tables

Chapter 1

Introduction

1.1 Motivation

One of the few ways to reach distant stars is by using radiation pressure as light sails, in which photon momentum is harnessed from free sunlight [51,56] or extraordinarily powerful laser systems [47, 95]. Although the magnitude of radiation pressure may seem relatively weak owing to its inverse relation to the speed of light, the force may be comparable to the gravitational force in outer space. Compared to chemical rockets that require a burn for each acceleration "push" for orbit transferring, light sails experience continuous acceleration as long as there is light on the sail. Yakov Perelman first proposed the concept of utilizing radiation pressure as a means of propulsion in space in 1915 in the book Interplanetary Journeys. The first detailed solar sail design was developed in the early 1980s by Jet Propulsion Laboratory for a rendezvous mission with Halleys Comet [71, 99, 168]. The idea is to use large but lightweight sails to reflect solar photons, transferring their momentum to an attached spacecraft. Solar sails was only successfully deployed in

the past decade. In May 2010, the first-ever solar sailcraft, IKAROS (Interplanetary Kitecraft Accelerated by Radiation of the Sun), was deployed by the JAXA (Japan Aerospace Exploration Agency). The 196 m^2 sail achieved attitude control by using reflective control devices (RCD) and completed a Venus flyby mission. A few months later, NASA deployed a solar sail demonstration mission NanoSail-D2 from a Cubesat to low Earth orbit. The sail was made of CP-1, a thin aluminum coated polymer, with a thickness of 7.5 μm, and a surface area of about 10 m^2 [67]. The sail was wound tightly around a central hub. When the sail deployed, four booms sprang out to unfurl the sail and support its structure. In May 2015, the Planetary Society deployed the LightSail-1, made of mylar reflective sheet with a thickness of 4.5 μm, area of 32 m^2 stowed in a 3-Unit Cubesat [4]. Following, LightSail-2 withe the same size dimensions was deployed in 2019 [124]. The LightSail-1 mission demonstrated that the Society's lightsail could be successfully unfurled in space, whereas the LightSail-2 sail demonstrated the use of torque rods for attitude control as the sail orbited in low-Earth orbit (LEO).

Numerous solar sailing project was proposed. NASA partnered with L'Garde to launch the Sunjammer project, demonstrating the ability to make a 38 m $\times$ 38 m solar sail, a surface area of 1444 m^2. It would be used to provide early detection and warning of the geomagnetic storms on the Sun that can damage power and communication systems on earth and orbiting spacecrafts. Although the mission was unfortunately canceled in October 2014, it was the largest solar sail made and tested in a vacuum chamber on ground [118]. England's Surrey Space Centre (SSC) has partnered with University of Surrey to develop CubeSail, DeorbitSail, and InflateSail projects that will be launched in the near future [115].

NASA's next step is the Near-Earth Asteroid scout program, to launch a controllable

sailcraft that is capable of encountering near-Earth asteroids and collect data [101]. This 86 m^2 CP-1 solar sail, which is 2.5 μm thick, will be stowed in a 6U Cubesat, and is planned to launch in 2021. To demonstrate small satellite technologies to improve science observations in deep space, solar sail is also proposed to for sun observation as the Solar Cruiser. This large 1200 m^2, 90 kg solar sail is proposed to be launched in 2024 to cruise along vantage points off the Sun-Earth Line and provide views of the Sun not easily accessible with current technology such as coronographs. In early 2020, NASA also completed a study for a Solar Polar Imager (SPI) mission, where its science goal is to better understand the Sun and the heliosphere by observing the Sun from a high heliographic latitude. A highly inclined orbit (of 75) allows helioseismology observations from a high latitude, providing measurements in the high latitude regions for the first time.

At this early stage of solar sailing development, light sails are making rapid advancement in design and concepts from the lessons learned from demonstrative missions. There are important yet challenging missions identified to become practical with solar sailing, such as asteroid station keeping [58], near Earth asteroid rendezvous [122], terrestrial planet sample return missions [61], and planetary pole sitters [161]. With the potential to reach relativistic speeds and the maturity of directed energy [88], the idea of light-driven sails using phased-locked laser arrays opened up the possibility for interstellar travel. There is potential to implement lasers that provide irradiance that exceed 100 [MW/m^2] to a solar sail, whereas the sun provides 1361 [W/m^2] at 1 [AU]. The Breakthrough Starshot and NASA laser-sail projects [39, 66, 67] are generating excitement and broad interest as interstellar solar-sailing probes. The proposed probes could provide the means to overcome the limits of chemical rockets and nuclear rockets, and the anticipated sail sizes will increase from the tens of meters in diameter, to kilometers in diameter [66].

At this early stage of solar sailing development, light sails are making rapid advancement in design and concepts from the lessons learned from demonstrative missions. There are important yet challenging missions identified to become practical with solar sailing, such as asteroid station keeping [58], near Earth asteroid rendezvous [122], terrestrial planet sample return missions [61], and planetary pole sitters [161].

It is convenient here to introduce an expression of radiation pressure to illustrate the needs in a reflective solar sail (the detailed derivation from the photon momentum point of view will be provided later in the background section). A beam reflecting from a solar sail imparts a radiation force F due to the change in photon momentum, which is proportional to the optical power

$$F_R = 2(IA/c)r\cos\theta_i \ , \tag{1.1}$$

where $r = R + (1R)\alpha/2$ accounts for the fact that an absorbed photon imparts all its momentum, and a reflected photon imparts twice its momentum. R is the mirror reflectivity, α indicates the fraction of non-reflected light absorbed by the sail, θ_i is the angle of incidence, and c is the speed of light.The reflective sail is maneuvered by controlling the tilt of the sail (the cosine term), as depicted in Fig. 1.1, thus turning the solar thrust on while moving along the orbit direction and off while opposing the orbit direction. For example, on IKAROS, a liquid crystal reflectivity control device was placed on four edges and could be switched between diffuse/specular reflective states to tune r asymmetrically.

Diffraction gratings [146, 148] as a light sail material provide new opportunities, as optical radiation pressure provides both tangential and normal force to the sail surface, unlike the purely normal force exerted on a reflective sailing surface [33]. The tangential force component is parallel to the direction of the orbit (show in Fig. 1.2), so a diffractive

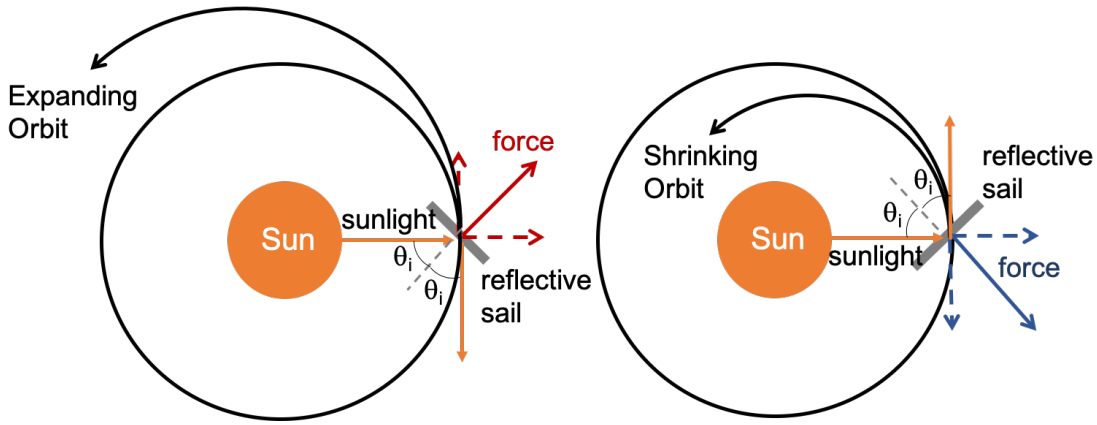

Figure 1.1: The maneuver of a reflective sail. The reflective sail faces the sun to receive thrust, and tilts to achieve an expanding or shrinking orbit [1], the sun incident angle is typically $\theta_i = 35°$.

solar sail can accelerate or decelerate by having the radiation pressure force acting along or opposite to the orbiting velocity, which can be flexibly controlled electro-optically. This avoids mechanical maneuvering (i.e., to tilt the entire sail), which could become an excessive burden as the sail size increases, and further provide higher efficiency on the use of photon momentum from sunlight. In the case where the sunlight is always normally incident to a diffraction sail maximum force is achieved ($\theta_i = 0°$). Comparing between Fig. 1.1 and 1.2, a reflective sail is unable to navigate in a sun-facing configuration, where as a diffractive sail can efficiently change orbital speed while in a sun-facing configuration.

At the time I joined this thesis project in 2016, not much research was conducted on exploring solar sailing apart from purely reflective materials, besides the stable optical lift [149] on dielectric semi-cylindrical arrays. After proposing the idea of diffractive sails [146], emerging designs applying refractive micro-prism arrays [46] and meta-material [7] to solar sails were proposed. Nevertheless, none of afore-mentioned radiation pressure

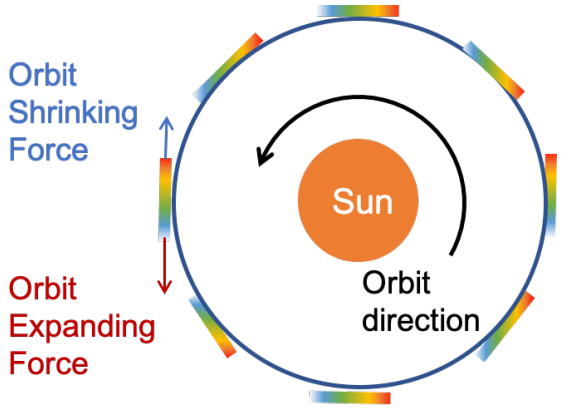

Figure 1.2: The maneuver of a sun-facing diffractive sail. The diffractive sail always faces the sun in orbit, receiving light with its full surface area. The sail expands or shrinks orbit by increasing or reducing the transverse radiation pressure force component on the sail.

forces have not been experimentally verified and demonstrated in the laboratory. This has become the main objective of my Ph.D. thesis research, which serves as a fundamental step to gain experimental understanding of these radiation pressure forces.

Furthermore, a diffractive sail may also be beneficial to a laser light sail in terms of stability. An important problem for laser light sails is ensuring that the sail remains centered on the laser beam despite disturbances and misalignment [62, 92]. It is ideal to have a passive, restoring force on the sail when a deviation from the beam occurs. It is possible to structurally design a refraction, diffraction, or meta-material sail that reacts to beam misalignment by providing an opposite force component to re-align the beam and the sail. We have come up with a "diffractive beam-rider" structure design that possesses this quality, and experimentally verified it with a time modulation of the laser.

These diffractive sail studies, accompanied with the roadmap of NASA [66], international space-agencies and private entities, utilize the low-cost Cubesats as opportunities to setup test flights and further testing space-qualified material and mission-oriented optimal

designs will be grand goals in the future for realizing solar sails into space.

1.2 Overview

In the following chapters of the thesis, Chapter 2 provides the literature background for optical radiation pressure and its measurements to support the motivation of measurements of radiation pressure on a diffractive solar sail. Furthermore, the chapter details the theories and methods of quantifying momentum transfer on a diffraction grating. A single order diffraction grating, instead of multiple order diffraction, concentrates the photon momentum transfer instead of spreading the power out, so we then discuss candidates for single order diffraction gratings.

Chapter 3 describes a model of how a single-order diffraction grating may be beneficial in a space mission of orbit lowering and inclination raising. Further more, we discuss how the diffraction and birefringent properties of liquid crystal cycloidal diffraction gratings (CDWs) may be utilized, and how its limits may be overcome for the application of a diffractive solar sail.

Chapter 4 describes the experiment setup that I built for force measurements on prototype diffractive light-sail samples. Since all force measurements were performed on small prototype sails with the forcing laser power under 5 Watts, the setup was designed to be sensitive enough to measure a corresponding force magnitude of sub-nanoNewtons, while also allowing the sail samples to exhibit motion. The system behaviour can be mathematically described as an harmonic oscillator driven by optical radiation pressure. After an unforced system was characterized, I describe the experiment that verifies the "grating momentum" quantitatively.

Chapter 5 describes experimental verification of diffractive lightsail applications as a diffractive "beam-rider". This is a key demonstration for both solar sailing and laser sailing. We discuss the demonstration the "cooling" effects on a "Diffractive Beam-Rider" , on a "bi-grating" prototype and an "axicon" proptotype, proving one-dimensional and two-dimensional restoring force that pulls the sail towards the beam path when displacement occurs, respectively.

Chapter 6 provides my thoughts and recommendations on further improvements of the experimental setup.

Chapter 2

Background

With the application of diffractive sails laid out, great importance directs to studying the radiation pressure property and limits on diffractive sails. We aim to set this foundation on understanding and measuring radiation pressure of a diffractive material in a laboratory setup. This chapter gives the background knowledge on the basic radiation pressure properties and its measurements (Section 2.1), then explores how the radiation pressure interacts on a diffraction grating (Section 2.2). High efficiency single order diffraction gratings are then discussed (Section 2.3).

2.1 Radiation Pressure

The optical radiation pressure is rather weak and was not trivial to observe. In this section, we lay out the theoretical expression as well as the experimental methods that scientists developed over the years to understand and measure this small force that is easily

overwhelmed by other forces on Earth. Furthermore, by controlling different modulations of a laser beam, it is made possible using optical radiation pressure to trap, manipulate, propel, or modify objects. Since a homogeneous light source (i.e., sunlight) is a prerequisite for solar sailing, it is of interest to modulate the object receiving the radiation pressure.

2.1.1 Theory

It has been observed that light exerts pressure since 1619, when Kepler used it to explain why the comet's tail is pointed away from the sun [80]. Not until 1873, Maxwell [97] in his Treatise on electricity and magnetism, expressed the mechanical pressure of a transverse electromagnetic wave in its direction of propagation in free space with a complete theory. The pressure is determined by the energy density U(energy per unit volume)

$$U = \frac{1}{2}(\epsilon_0 E^2 + \nu_0 H^2) = \epsilon_0 E^2 = \mu_0 H^2, \text{ as } H = \sqrt{\frac{\epsilon_0}{\mu_0}} E. \tag{2.1}$$

where ϵ_0 and μ_0 are the permittivity and permeability of free space, respectively.

The existence of radiation pressure shows that electromagnetic waves also carry momentum. In the beginning of 1900's, Poynting [87, 126] considered light as a 'stream of momentum'; Minkowksi [104] and Abraham [5] each followed up with expressions based upon the classic electromagnetic theory of that linear momentum in a dielectric medium. Both theories reduce to the expression for light momentum of $p = h\nu/c$ for a single photon in free space, where h is the Planck's constant, ν is the frequency of light, and $c = 2\pi\nu/k$.

A useful expression is to rewrite with wave vectors as

$$p = \hbar k \tag{2.2}$$

where $\hbar = h/2\pi$, is the speed of light and $k = 2\pi/\lambda$ is the wave number. A packet of N such photons passing through a plane over a time t carries a net momentum $N\hbar k$. If the packet is elastically deflected by a material in another direction characterized by the wave vector $\vec{k'}$, the net momentum changes to $N\hbar\vec{k'}$. From Newtons third law, the force on the material is

$$\vec{F} = N(\vec{k} - \vec{k'})/t = (P/ck)(\vec{k} - \vec{k'}) \ , \tag{2.3}$$

where $P = Nh\omega/c\Delta t = N\hbar k/\Delta t$ is the power of the beam of photons, $\vec{k}$ is the incident wave vector of light and $\vec{k'}$ is the final wave vector of light. The momentum transferred to the object is small and derived in Appendix B.

The simplest example of this force would be the radiation pressure force exerted on a perfect reflector, when the beam comes in normal to the surface. In this case,

$$\vec{F} = N(\vec{k} - \vec{k'})/t = (2P/c)\hat{k} \ . \tag{2.4}$$

From these expressions we learn that the radiation pressure of light is extremely small compared to those we exert on daily known objects. For a typical laser pointer power of 0.5 mW, the radiation pressure force exerted on a perfect mirror will be on the order of pN. The gravitational force on a small spherical water droplet of 2 mm diameter is 10^7 times more than the radiation pressure force we just calculated from the laser pointer.

2.1.2 Measurements

To measure the weak optical radiation pressure, a torsion pendulum was used, where a thin bar is hung at the center from a torsion filament in an evacuated chamber, and the asymmetry of torque created by sun or a bright light source would cause the filament and

bar to rotate. This design helped to eliminate the effect of gravity, which is perpendicular to the direction of torque on the pendulum.

However, the convection forces from residual gas in the chamber dominates the cause of the torque in this type of experiments [38,41,48,170]. Improvement in vacuum technology and careful calculations to rule out the heat effects, enabled the efforts of Russian physicist Pyotr Lebedev in 1900 [96] and by Ernest Fox Nichols and Gordon Ferrie Hull in 1901 [112, 113], to measure the radiation pressure of light quantitatively and closely agreed to Maxwell's expressions.

Lasers allowed the radiation pressure experiments to shrink in size, and with better concentrated power. Micromechanical systems, such as microcantilevers and atomic force microscope (AFM) detection, can perform force measurements in ambient conditions and are high in sensitivity and commercial availability [29]. In Atomic force microscopes, a sample is scanned by a tip mounted on a cantilever spring. While scanning, the force between the tip and the sample is measured by monitoring the deflection of the cantilever. The cantilever can also be dynamically excited. Either the shift in resonance frequency is detected using a feedback system [9,160] or the change in amplitude at constant excitation frequency and excitation amplitude is measured [49, 79]. The resonant signal provides benefits for force measurements under ambient conditions, water, and different gases. For an optical radiation pressure measurement, although heat induced thermal-elastic strains and surface charge density induced electronic deformation exists [156], scientists are able to differentiate between the radiation pressure excitation and excitation driven by other sources by analyzing the oscillating spectrum [90].

Thanks to the advancement of micro-electronic-mechanical-systems (MEMS) fabrication technology, micro/nano-mechanical transducers have become sensitive enough that

radiation pressure can influence them greatly. Dynamic resonance driving techniques can be applied in various forms of micro-resonators and micro-oscillators [30, 63, 85, 106].The availability of these MEMs devices capable of probing tiny forces with atomic spatial resolution benefited research fields of interest include active cooling of mechanical resonators in cavity optomechanics, cantilever spring constant calibration, enhanced radiation force in a microwave resonant unit, etc. From these research areas, we gained a more detailed understanding of the mechanical effects of light that were exploited in laser trapping and cooling [103].

High laser powers over 1000W have become commercially available for industrial laser processing applications and brought radiation pressure measurements to a macroscopic level. Scientists have developed a relatively portable radiation pressure power meter: using a vertically mounted scale and mirror to measure micro-Newton forces for 100 to 100kW lasers [133, 166, 167]. These radiation-pressure power meters enable accurate and traceable power measurements without the error from beam splitting, or having mutually exclusive beam power measurements and the use of the laser beam.

Torsion pendula are most classically known for Cavendish experiments of measuring the Newtonian gravitation constant G [55]. They are applied to a rich spectrum of weak force measurements because of its ability to place the Earth's gravitational force orthogonal to the force of interest, eliminating the competition between the weak force and the Earth's. The pendulum motion, including the static component–change of equilibrium position; and the dynamic component–oscillation of the pendulum over time, are both used for the determination of force. Fundamental optical forces have been measured using a torsion pendulum, such as using a fiber-suspended quarter-wave plate for the determination of the angular momentum of light [20], and also constructing a dual rotational axis to be an

absolute laser power meter using radiation pressure force [131].

2.1.3 Applications

There are two components in a light-matter interaction like optical radiation pressure exerting force on objects. As lasers come into play with the collimated and coherent properties of light , Arthur Ashkin was able to identify that there are two basic forces in a focused laser beam: 1. a scattering force in the direction of incidence of the light beam 2. a gradient force along the direction of the intensity gradient of a Gaussian beam profile [14]. In 1986 a new field opened up when Ashkin trapped dielectric particles of various sizes in a single-beam gradient force trap known as optical tweezers, in the medium of water, air, and vacuum [15]. The pico-Newton force is specifically applicable for manipulating small-neutral particle, atoms, and molecules.

Optical tweezers and optical traps have allowed researchers have investigated a wide range of important biological interactions [19, 26, 45, 57] as well as classical statistical mechanics [105, 136] in a way that was not previously possible.

The optical tweezer also enabled measurements of other small forces. For example, an optically trapped particle displacement was monitored by deflection, reflection, or interferometry [44, 53, 70, 140]. Combined with total internal reflection microscopy (TIRM), the scattered intensity distribution can be used for measuring the Casimir force on particles [60].

Following the focused Gaussian optical trap, the modulation and control of the beam with diffractive optics is one of the most powerful enhancements of the single trap The research and engineering of these synthesized beam shapes bloomed for its versatility. Since a highly focused optical tweezer can be destructive to absorptive particles, solutions such as

optical vortex beams, i.e., a donut-shaped beam with a null at the center, form traps where a low refractive index particle can be trapped on the optical axis a short distance above the focal plane [52]. Certain propagation-invariant beams help to increase the depth of focus along with their special properties, e.g., Airy beam that enhances transverse acceleration and Bessel beams that has a self-healing central lobe as it propagates [127].

Complex modulation is achieved by holographic optical tweezers (HOTs) and space light modulators (SLMs) that forms arbitrary traps. The advantages include: complex traps can be two or three dimensional; larger traps can have multiple independent trap points, and traps can be updated in real-time by controlling the electro-optic pixels in an SLM. The traps can be virtually anything – the only limits are the spatial resolution of the SLM and the range of spatial frequencies that are passed by the microscope objective. Few examples are line traps that confine the tweezer manipulation in a single direction; dynamic and real-time control of cell growth [42].

In addition to the extensive focus on controlling the light, attention was drawn to the matter in the recent decade. Asymmetry in the shapes or guided light deflections [119] of an object can affect the direction of force, e.g., a stable light lift [149]. Furthermore, when the object is more complex and carefully designed [13, 94, 169], it may act as an optical motor when illuminated by a light beam.

Modern materials such as electro-optic materials [158, 159] provide tunable control of reflectivity, which also tunes the linear momentum changing rate, i.e., force. Channeled waveguides [69] and micro-ring resonators [84] can be designed for controlling particles. Meta-materials, materials with size structures smaller than the wavelengths of the incident wave, can be designed to have a surface with phase-gradient and generate surface waves to manipulate nanoparticles. Anisotropic phase gradient structures may also be used to

control the direction of motion by tuning the polarization of the illumination [6].

2.2 Diffraction from a Grating

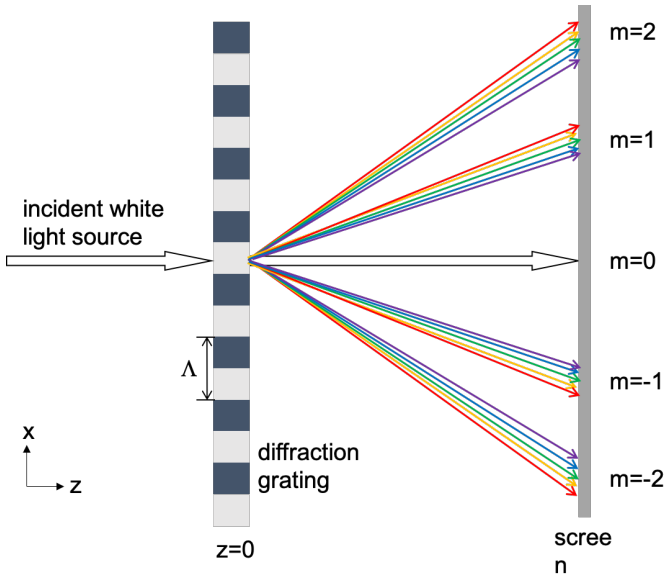

Figure 2.1: A white light source normally incident to a diffraction grating.

A diffraction grating is a periodic optical element that splits light, based on its wavelength composite and incident angle to the grating, into several different beams directions. Diffraction gratings can be made transmissive or reflective, and the periodic structure can be embedded in amplitude or phase, while all following the same diffractive rules. We may start from a transmissive diffraction grating with a consider a single transverse dimension, x, as an example (Fig. 2.1): when incident light is normal to the grating surface, the diffracted angle θ_m can be described by $\sin\theta_m = m\lambda/\Lambda$, where m is the diffractive order of the light, λ is the wavelength, and Λ is the grating period.

The angular spectrum of light may be illustrated by examining monochromatic light transmitted through such diffraction grating as well. The incident electric field may be expressed $E(x, z < 0) = A\exp(i2\pi z/\lambda)$, whereas the transmitted field at the exit face of the grating may be expressed as a Fourier series because the grating is infinitely periodic:

$$E(x, z = 0) = \sum_{m=-\infty}^{\infty} a_m \exp(imKx) \tag{2.5a}$$

$$\text{where } a_m = (1/\Lambda)\int_{-\Lambda/2}^{\Lambda/2} E(x, z = 0)\exp(imKx)dx \tag{2.5b}$$

where $K = 2\pi/\Lambda$ is the fundamental harmonic and mK are higher harmonics. Note that this initial field is independent of the wavelength of light. We must consider wavelength, however, if we want to describe the propagation of light. Let us assume that we know the exit field distribution immediately after the thin period grating $E(x, z = 0)$ so that we can calculate the Fourier coefficients a_m. The angular spectrum may then be computed for each harmonic component, $E_m = a_m \exp(imKx)$.

Physical arguments suggest that $|\theta_m|$ can not exceed 90°, which occurs when the denominator equals zero: $m\lambda/\Lambda = \pm 1$. Therefore the maximum allowed diffractive order $|m|$ is $m_{max} = \text{int}(\Lambda/\lambda)$ (where int is the integer function). If $|m| < m_{max}$ then $E_m(x, z)$ propagates forward. If $|m| > m_{max}$ then $E_m(x, z)$ is an evanescent wave that does not propagate forward.

For a diffraction grating with fixed period Λ, the same physical argument poses limits on the allowed propagation if the incident angle θ_i or wavelength varies. The incidence angle falls in the range of $\sin^{-1}(1 - m\lambda/\Lambda) \leq \theta_i \leq 90°$, and the maximum diffracted wavelength is $\lambda_{\max} = (\Lambda/m)(1 + \sin\theta_i)$.

The relative intensity or efficiency of the mth diffracted order of the grating is

$$\eta_m = |a_m^2|/|A^2|. \tag{2.6}$$

2.2.1 Momentum Transfer on a diffraction grating

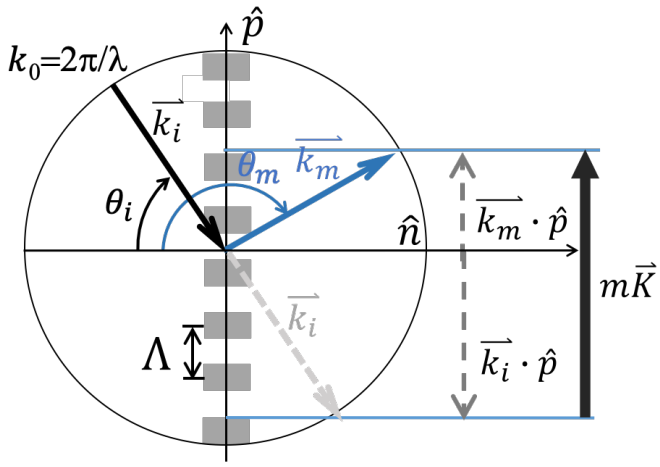

Figure 2.2: Momentum transfer and k-vector relations on a single-order diffraction grating. On the unit circle with magnitude $k_0 = 2\pi/\lambda$, the tangential component of incident and diffracted wave vectors $\vec{k_i}\cdot\hat{p}$ and $\vec{k_m}\cdot\hat{p}$ differs by $m\vec{K}$ for any incident angle other than cut-off angles.

A beam of light with wavelength λ is diffracted from a grating having a period Λ according to a phase matching condition along the the grating boundary, as dictated by Maxwells equations. Assume a grating momentum vector $\hat{K} = 2\pi/\Lambda\ \hat{p}$ that is tangential to the grating surface, where and $\hat{p}(\hat{n})$ is the unit vector parallel(normal) to the grating surface. The boundary condition at the surface maybe expressed

$$(\vec{k_i} + m\vec{K})\cdot\hat{p} = \vec{k_m}\cdot\hat{p}, \tag{2.7}$$

where $\vec{k_i}/k_0 = -\sin\theta_i\ \hat{p} + \cos\theta_i\ \hat{n}$ is the incident wave vector, $\vec{k_m}/k_0 = \sin\theta_m\ \hat{p} - \cos\theta_m\ \hat{n}$ is the diffracted wave vector, and $k_0 = 2\pi/\lambda$ is the wave number. The phase-matching condition is in agreement to the conservation of momentum (Fig. 2.2), and also leads to the well-known grating equation:

$$\sin\theta_m = -\sin\theta_i + m\lambda/\lambda. \tag{2.8}$$

The diffraction angle θ_m may be expressed in terms of sine and cosine functions:

$$\sin\theta_m = m\lambda/\Lambda - \sin\theta_i;\ \cos\theta_m = \pm(1-\sin^2\theta_m)^{1/2} \tag{2.9}$$

where the plus (minus) sign corresponds to a reflected (transmitted) order.

The conservation of momentum may be rewritten based on vector properties

$$k_{m,p} = k\ (m\lambda/\Lambda - \sin\theta_i) \tag{2.10a}$$

$$k_{m,n} = \pm k\ (1-(m\lambda/\Lambda - \sin\theta_i)^2)^{1/2} \tag{2.10b}$$

The vector relationships can be visualized in Fig. 2.2, depicting the common case where incident angle exceeds the cut-off angle ($|\theta_i| > \theta_{i,c}|$), the incident and diffracted wave vector has equal length $|\vec{k_i}| = |\vec{k_m}| = k = 2\pi/\lambda$, Eq. 2.10 reduces to $k_{m,p} = k\sin\theta_m$, $k_{m,n} = k\cos\theta_m$. When $|\theta_i| \leq \theta_{i,c}|$, $|k_{m,p}|$ has a value larger than $|k|$, and $k_{m,n}$ becomes an imaginary number falling outside the $|\vec{k}|$ circle.

The general expression for radiation pressure force on a non-absorbing grating may be

expressed as the mechanical reaction to optical diffraction (see Appendix A):

$$\vec{F} = (P_i/ck)(\vec{k}_i - \sum_m \eta_m \vec{k}_m), \tag{2.11}$$

where $\eta_m = P_m/P_i$ is the efficiency of the mth diffracted beam, P_i (P_m) is the incident (diffracted) beam power; energy conservation requires $\sum_m \eta_m = 1$.

From Eq. 2.11 and the given expressions for $\vec{k_i}, \vec{k_m}$, for a given wavelength the radiation pressure force on a grating may be expressed

$$\vec{F}_\lambda = \frac{IA\cos\theta_i}{c} \sum_m \eta_m (C_{i,m}\hat{n} - S_{i,m}\hat{p}) \tag{2.12}$$

when the beam over-fills the grating ($P_i = IA\cos\theta_i/c$), where $C_{i,m} = \cos\theta_i + \cos\theta_m$, $S_{i,m} = \sin\theta_i + \sin\theta_m = m\lambda/\Lambda$, η_m is the fraction of incident beam power that is diffracted to the m-th order, I is the irradiance, A is the area of the grating, and c is the speed of light.

2.2.2 Maxwell's Stress Tensor

The forces from a plane wave on a flat optical element can be found by using the Maxwell's Stress Tensor. This method is useful when we know the electromagnetic wave expressions in and out of the element. The momentum between the incident wave, reflected wave, and transmitted wave would be conserved, described by

$$\mathbf{f} + \epsilon\mu\partial\mathbf{S}/\partial t = \nabla \cdot \vec{T}\ , \tag{2.13}$$

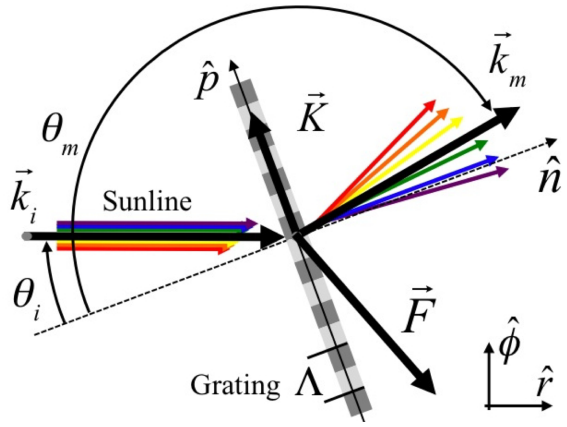

Figure 2.3: Sunlight as an example of broadband light incident upon a diffraction grating of period Λ, with a fixed beam in direction $\hat{r}$ and surface normal $\hat{n}$ subtending the angle θ_i. Incident, diffracted, grating wave vectors: $\vec{k}_i$, $\vec{k_m}$,$\vec{K}$. Surface unit vector $\hat{p}$. Diffraction angle, θ_m . Radiation pressure force imparted to the grating, $\hat{F}$. Adapted from [148]

where $\mathbf{f}$ is the force density, ϵ is the electric permittivity, μ the magnetic Permeability, $\mathbf{S}$ is the Poynting vector (energy flow) and $\vec{T}$ is the Maxwell's stress tensor. Since we are only observing the forces at a specific instant in time, $\partial\mathbf{S}/\partial t$ will be zero. The Maxwell's stress tensor represent the interaction between electromagnetic forces and mechanical momentum as

$$\vec{T} = \epsilon_0\epsilon\mathbf{EE} - \mu_0\mu\mathbf{HH} - \frac{1}{2}(\epsilon_0\epsilon E^2 + \mu_0\mu H^2)\vec{I} \tag{2.14}$$

where $\mathbf{E}$ is the electric field strength, $\mathbf{H}$ is the magnetic field strength, and $\vec{I}$ denotes the unit tensor.

We may consider a transverse electric (electric field polarization perpendicular to) incident wave plane wave incident to the normal of the diffraction grating with an incident

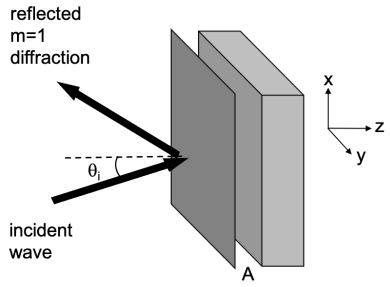

Figure 2.4: Configuration used to derive radiation pressure on a reflective diffraction grating by Maxwell's Stress Tensor.

angle θ_i:

$$\mathbf{E}_i = E_0 e^{-ik_0(x\sin\theta_i + z\cos\theta_i)}\hat{\mathbf{y}} \tag{2.15a}$$

$$\mathbf{H}_i = \frac{E_0}{\eta_0}\cos\theta e^{-ik_0(z\cos\theta_i - x\sin\theta_i)}\hat{\mathbf{x}} + \frac{E_0}{\eta_0}\sin\theta_i e^{-ik_0(z\cos\theta_i - x\sin\theta_i)}\hat{\mathbf{z}}\ . \tag{2.15b}$$

Using the divergence theorem, the volume integral of the Maxwell stress tensor gradient can be set equal to the closed surface integral of the Maxwell stress tensor through the solar sail. The time averaged mechanical force is then

$$\langle F\rangle = \int_V \nabla\cdot\langle\vec{T}\rangle\ dV = \oint_{\partial V}\langle\vec{T}\rangle\cdot\hat{\mathbf{n}}\ da \tag{2.16}$$

where ∂V denotes the surface of V, $\hat{\mathbf{n}}$ is the unit vector perpendicular to the surface, and da is an infinitesimal surface element. We may now find the Maxwell stress tensor for the

incident field

$$\vec{T_i} = \frac{E_0^2 \epsilon}{2\eta_0^2} \begin{bmatrix} \cos(2\theta_i) - \epsilon\eta_0^2 & 0 & -\mu_0 \sin(2\theta_i) \\ 0 & \epsilon_0\eta_0^2 - \mu_0 & 0 \\ -\mu_0 \sin(2\theta_i) & 0 & \cos(2\theta_i)\mu_0 - \epsilon_0\eta_0^2 \end{bmatrix}, \tag{2.17}$$

where $\epsilon = \exp^{-2ik_0(\sin\theta_i x + \cos\theta_i z)}$, and the integration on the planar surface with area A normal (n) and parallel (p) to the element surface is

$$\langle F_{i,z} \rangle = \frac{1}{2}\epsilon_0 A E_0^2 \cos^2(2\theta_i)\ \hat{\mathbf{z}} \tag{2.18a}$$

$$\langle F_{i,x} \rangle = \frac{1}{4}\epsilon_0 A E_0^2 \sin(2\theta_i)\ \hat{\mathbf{x}} \tag{2.18b}$$

where A is the surface area of the grating.

In the Fourier series expression of diffracted waves in Eq. 2.5, we know that a diffraction grating introduces a linear phase of $\Phi = mKx$ parallel to the grating, and if $m = 1$, $\psi_x = Kx$. In this case we look for a reflective, first order diffraction. The Maxwell's Stress Tensor for the diffracted field then may be expressed

$$\vec{T_d} = \frac{E_0^2 \alpha}{2k_0^2\eta_0^2} \begin{bmatrix} -(k_0^2\epsilon_0\eta_0^2 + \beta\mu_0) & 0 & \delta \\ 0 & k_0^2(\epsilon_0\eta_0^2 - \mu_0) & 0 \\ \delta & 0 & -(k_0^2\epsilon_0\eta_0^2 - \beta\mu_0) \end{bmatrix} \tag{2.19}$$

where,

$$\alpha = e^{-2ik_0[-(K/k_0-\sin\theta_i)x+\sqrt{(1-(K/k_0-\sin\theta_i)^2}z)}$$

$$\beta = 2K^2 + 4\sin\theta_i k_0 K - \cos(2\theta_i)k_0^2$$

$$\delta = 2k_0^2\mu_0(K/k_0 - \sin\theta_i)\sqrt{(1-(K/k_0-\sin\theta_i)^2}$$

The plane forces are found to be

$$\langle F_{r,z}\rangle = \frac{E_0^2 A}{4\eta_0^2 k_0^2}\left[\mu_0(-2K^2 - 4Kk_0\sin\theta_i + k_0^2\cos(2\theta_i) + \eta^2 k_0^2\epsilon_0)\right]\hat{\mathbf{z}} \tag{2.20a}$$

$$\langle F_{r,x}\rangle = -\mu_0\frac{E_0^2 A}{2\eta_0^2}\left[(K/k_0 + \sin\theta_i)\sqrt{(1-(K/k_0-\sin\theta_i)^2}\right]\hat{\mathbf{x}} \tag{2.20b}$$

Combining the forces influenced by both the incident and reflected fields, the force parallel to the reflective diffraction grating may be expressed

$$\langle F_z\rangle = \langle F\rangle_{i,z} + \langle F\rangle_{r,z} = \frac{\mu_0 A E_0^2}{2\eta_0^2}\left(\sin\theta_i\cos\theta_i - (K/k_0 + \sin\theta_i)\sqrt{(1-(K/k_0-\sin\theta_i)^2}\right) \tag{2.21a}$$

$$\langle F_x\rangle = \langle F\rangle_{i,x} + \langle F\rangle_{r,x} = \frac{E_0^2 A}{4\eta_0^2 k_0^2}\left(\mu_0(-2K^2 - 4Kk_0\sin\theta_i + k_0^2\cos(2\theta_i)) + 2\eta_0^2 k_0^2\epsilon_0(\cos^2\theta_i + 1/2)\right) \tag{2.21b}$$

2.3 High efficiency single-order diffraction gratings

The linear momentum carried by incident photons transfers to an object and imparts linear radiation pressure. A single order diffraction grating concentrates this momentum change as the majority of incident photon direction goes towards a single direction. The resulting

radiation force can be designed towards arbitrary directions, as the grating period can be flexibly made. However, according to Fourier theories, a general periodic surface without special engineering would always have multiple diffractive orders in the far field, which spreads out the incoming photons and reduces the force.

Special designs such as meta-materials with structures smaller than the light wavelength can be designed to bend light in unconventional ways. Liquid crystal thin film gratings with its thickness on the order of the wavelengths has properties to provide only single order diffraction. In my thesis work, I have the chance to access the types of gratings below: 1. A commercially available sub-wavelength grating designed for Littrow transmission order; 2. Polarization-sensitive liquid crystal cycloidal diffractive waveplates; 3. Flat multi-level diffractive surfaces; 4. Metasurface designed for perfect refraction, i.e., bending light as in ideal single order diffraction.

Diffraction Efficiency can be divided into two types: "relative diffraction efficiency" and "absolute diffraction efficiency." The absolute diffraction efficiency is the ratio of the diffracted light intensity, of a given order, to the incident light intensity. The relative diffraction efficiency is obtained by dividing the absolute diffraction efficiency by the reflectance of the coating material for a reflective grating, or transmittance of the grating for a transmissive grating. In most literature and diffraction grating manufacturers, the term of relative diffractive efficiency is adopted.

The diffraction efficiency of a grating can vary significantly with the polarization of incident light, because the grooves in a grating are all etched in one direction. With S-polarization (TM waves), where the direction of the grating grooves and the oscillation direction of an electric field is perpendicular, anomalies exist in the efficiency curve (efficiency vs. wavelength curve, as shown in Fig. 2.5). Anomalies are locations that the curve

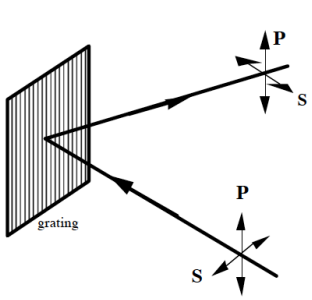

(a) P-polarization has the electric oscillation direction parallel to the grating grooves; S-polarization has the electric oscillation direction perpendicular to the grating grooves.

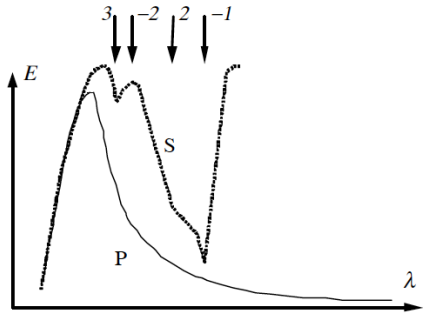

(b) A typical efficiency curve that peaks at the blazed wavelength λ. The efficiency curve for S-polarization has more anomalies, but the efficiency is higher for loner wavelengths. Adapted from [86]

Figure 2.5: Polarized light and blazed grating efficiency

changes abruptly. In a typical efficiency curve, within the long-wavelength regions, higher diffraction efficiency is exhibited. With P-polarization (TE waves), where the direction of the grating grooves and the oscillation direction of electric field vectors is parallel, there is not as much fluctuation as with S-polarization. In general, for unpolarized light, the efficiency curve would fall between the curves of TE and TM polarizations.

2.3.1 Blazed Grating

A blazed grating consists of micro-prisms made of glass that refracts light into a certain angle based on its geometry, to achieve maximum efficiency at a single diffraction order. The surface geometry forms a sawtooth profile described in Fig. 2.6a, where the slanted normal with angle γ provides a match for both the Snell's law and the grating equation. The geometry design enables most of the diffracted light to go to one designated order,

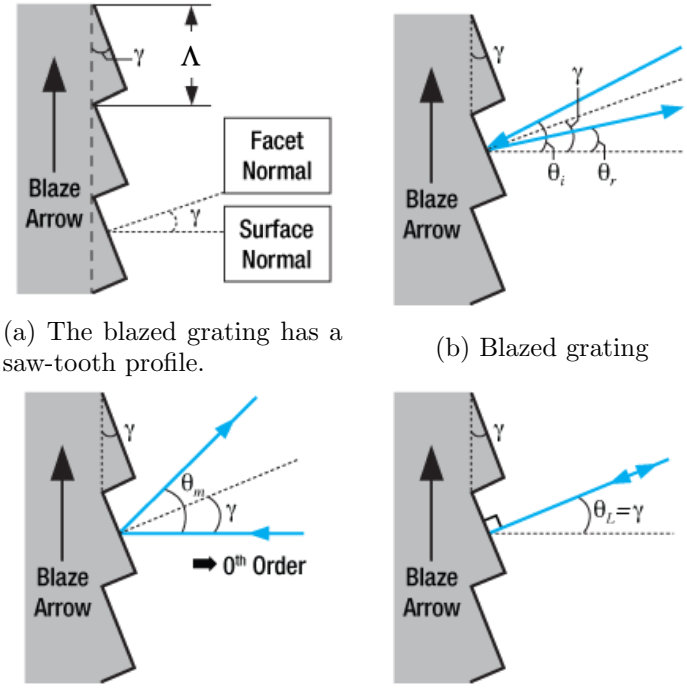

(a) The blazed grating has a saw-tooth profile.

(b) Blazed grating

(c) Blazed grating under normal incidence light.

(d) Blazed grating under Littrow configuration.

Figure 2.6: Blazed grating properties. Image adapted from [153].

and the zero order is minimized at the blaze wavelength. A blazed grating can be reflective or transmissive, and here we look at a reflective example in Fig. 2.6b where the incident angle θ_i forms a relation between the reflected(diffracted) θ_r angle by

$$\theta_i - \theta_r = 2\gamma \tag{2.22}$$

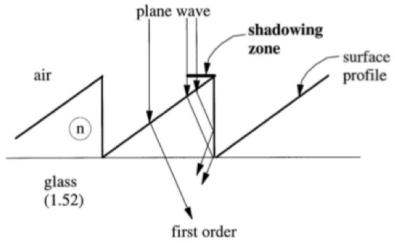

Figure 2.7: The shadowing effect on a saw-tooth profile. In the shadowing zone, incident rays are not diffracted into the desired order. Adapted from [86].

. At normal incidence to the grating $\theta_i = 0°$ as in Fig. 2.23, we can combine the above Eq. 2.22 and the grating equation Eq. 2.8, which results in

$$\sin(-2\gamma) = m\lambda/\Lambda. \tag{2.23}$$

The Littrow configuration is another interesting case where the diffracted beam lies directly on top of the incident beam, i.e., the incident and diffracted angle is the same (Fig. 2.6d). The grating equation can now be re-written as

$$2\sin(\theta_L) = m\lambda/\Lambda, \text{where } \theta_L = \gamma. \tag{2.24}$$

The efficiency behavior of a blazed grating depends on the grating period λ/Λ, peaking at the blazed wavelength. In general, the efficiency curve can be derived from the scalar diffraction theory. For larger blaze angles (grooves depth for sinusoidal gratings), scalar theory becomes less applicable, and the diffraction efficiency varies significantly with the polarization. Manufactured from mechanical ruling or ion etching, the idea of a blazed grating is straightforward, yet due to geometrical "shadowing" effects, absolute diffraction efficiency is limited to limited to 50% at the blazed order [86].

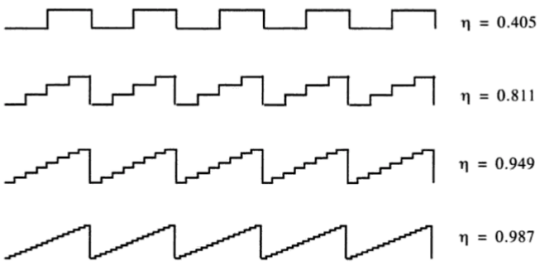

(a) N-level binary phase grating structure can achieve a high efficiency blazed grating effect. The diffractive efficiency can be described in Eq. 2.26. Adapted from [43].

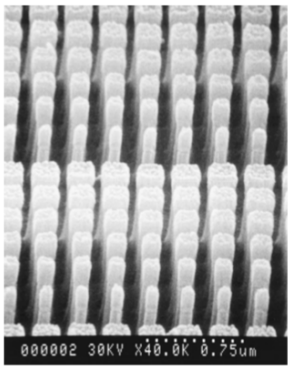

(b) A realized N-level binary phase grating structure that can achieve a high efficiency blazed grating effect. Adapted from [76].

2.3.2 Binary Phase Grating

The binary phase grating has been described as a crude approximation of a blaze grating. and the transmission function, take binary phase grating as an example, has the modulation purely in phase

$$g_0(x) = \begin{cases} 1, 0 \leq |x| \leq \Lambda/4 \\ -1, \Lambda/4 < |x| \leq \Lambda/2 \end{cases} \tag{2.25}$$

The periodic transparencys complex amplitude transmission may be expressed as a Fourier series expansion, where the amplitude of an order is $c_m = \frac{1}{\Lambda}\int_{-\Lambda/2}^{\Lambda/2} g_0(x)\exp(i2\pi mx/\Lambda)dx = \text{sinc}(m/2)$, and $\text{sinc}(\xi) = \sin(\pi\xi)/(\pi\xi)$. The efficiency for odd orders is the absolute squared of the Fourier series amplitude, so $\eta_{\pm m} = (\frac{2}{\pi m})^2$, and the first order efficiency will be $\eta_{\pm 1} = 40.53\%$ based on symmetry. By increasing the numbers of etched steps into a N-level binary grating structure, as depicted in Fig. 2.8a, the diffractive efficiency

expression can be rewritten as

$$\eta = |\frac{\sin(\pi/N)}{\pi/N}|^2 \ , \tag{2.26}$$

where the number of levels N may be limited by the binary etching process, and the theoretical diffraction efficiency goes up to around $80 - 90\%$ [43], derived by the scalar diffraction theory.

Furthermore, a sub-wavelength structure can achieve single order diffraction by limiting the propagated diffraction orders. The incident light wavelength is smaller so that only one order is allowed, and other orders are evanescent. We consider the grating equation with the grating refractive index n_g. Since the incidence is in air, we can rewrite Eq. 2.8 as

$$-\sin\theta_i + m\lambda/\Lambda = n_g \sin\theta_m \ . \tag{2.27}$$

For a single order diffraction grating, for the first order $m = 1$ to propagate, $|\sin\theta_1| \leq 1$

$$\lambda/\Lambda \leq \sin\theta_i + n_g \tag{2.28}$$

For a the $m = 2$ to not propagate, $|\sin\theta_2| \geq 1$

$$\lambda/\Lambda \geq \frac{1}{2}(\sin\theta_i + n_g) \tag{2.29}$$

The collocation of a sub-wavelength structure and N-level pillar grating forms a blazed binary grating. This is realized with the design of appropriate constant thickness h and variable pillar width, as shown in Fig. 2.8b. With a blazed refractive index profile, it is successful to achieve efficiency higher than a ruled blazed grating up to 87% [75, 76]. The

optimal thickness of blazed binary gratings is given by

$$h = \frac{N-1}{N} \frac{\lambda}{n_{max} - 1} \ , \tag{2.30}$$

where n_{max} is the largest refractive index in the modulation profile.

2.3.3 Liquid Crystal Cycloidal Diffractive Waveplates (CDWs)

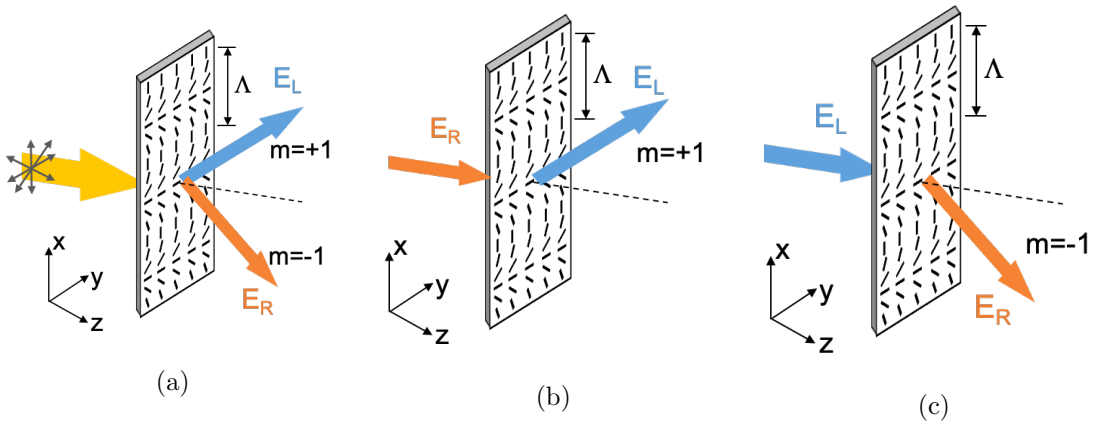

Figure 2.9: The polarization properties of a cycloidal diffractive waveplate with a grating momentum vector $\mathbf{K} = 2\pi/\Lambda\ \hat{x}$. (a) Unpolarized incident beam. Purely (b)right-circular (c) left-circular polarized incident beam

For liquid crystals, refractive indexes are dynamically adjustable, which enable the design of very high efficiency phase gratings. Furthermore, instead of tuning the refractive index, liquid crystals are also able to form another type of gratings that tunes the fast/slow anisotropy axis. The birefringence of the material could be constant, while the direction of fast/slow anisotropy axis is periodically modulated along the transverse plane of the waveplate, resulting in polarization gratings that selectively diffract light based on its polarization state, as shown in Fig. 2.9. This group of liquid crystal gratings are sometimes

also called optical axis gratings (OAG), liquid crystal polarization gratings(LCPG), or cycloidal diffractive waveplates (CDW).

Liquid crystal polarization gratings are thin and and has high efficiency diffraction single orders, used as beam-splitters [116], polarimeters [74], imaging display [108], and VR/AR systems to split images between eyes [31,82]. Its functionally expands further with electro-optically switching between diffraction orders for non-mechanical beam steering and control [32, 72, 111], or switch grating period [37].

Nematic liquid crystals (NLC) are used to realize these single-order polarization gratings, with circularly polarized incident light, and liquid crystal rotating in a transverse direction in the grating plane at a full rotation period Λ. The thickness of the grating Δz satisfies a half wave-plate (i.e. $k \cdot \Delta z = \pi/2$, where $k = 2\pi/\lambda$), where the diffracted beam switches to its opposite handedness [108, 135]. Since the thickness of these waveplates are on the order of the optical wavelength, the effects of multiple reflection is reduced and the absolute diffraction efficiency was reported to reach 95%.

These waveplates are holographically made by exposing photo-aligning nematic liquid crystals to two interfering orthogonal circularly polarized beams. The birefringence is induced as a product of photochemical reaction, and may be interpreted by the superposition

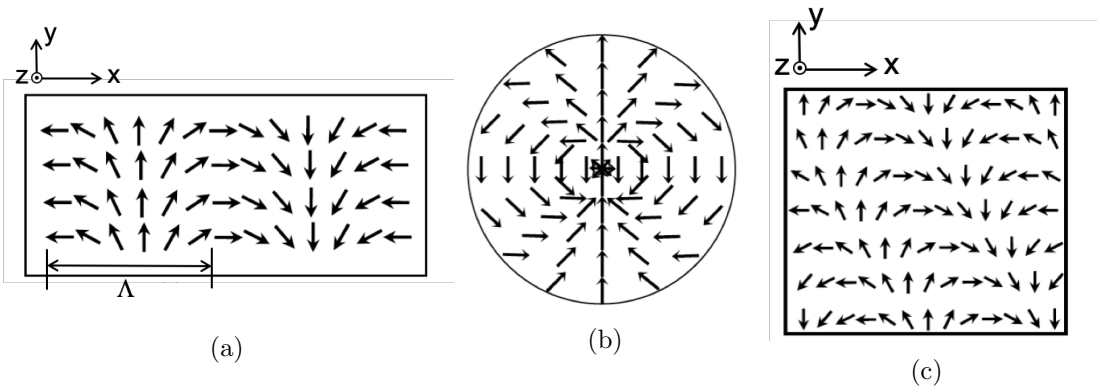

(a) (b) (c)

Cycloidal Diffractive waveplates that are cycloidal along (a) x-direction (b) Axial (vector vortex plate, q-plate) (c) 2-D Cycloidal, along any axis in the xy plane. Adapted from [111]

Figure 2.10: Cycloidal Diffractive Waveplates

of a left and right circularly polarized beams:

$$E_L = (E_0/2) \begin{pmatrix} 1 \\ i \end{pmatrix} \exp(i\pi x/\Lambda) \tag{2.31a}$$

$$E_R = (E_0/2) \begin{pmatrix} 1 \\ -i \end{pmatrix} \exp(-i\pi x/\Lambda) \tag{2.31b}$$

$$E_L + E_R = E_0 \ (\cos \pi x/\Lambda, \sin \pi x/\Lambda)^T, \tag{2.31c}$$

where $\Lambda = \lambda_R/(2 \sin \theta_C)$ is the modulation period, λ_R is the wavelength of the recording beams, and θ_C is the incident angle of the recording beams [116].

The director in neumatic liquid crystal polarization gratings has the azimuth of the

director $\mathbf{n}$ rotating along the x-direction:

$$\mathbf{n}(x) = (\cos(\theta_C(x)), \sin(\theta_C(x)), 0) \tag{2.32}$$

where $\theta_C(x) = \mathbf{K}x/2$, $\mathbf{K} = \pm 2\pi/\Lambda\hat{x}$ is the grating momentum, and Λ is the optical grating period.

The Jones Transfer Matrix expresses the polarization transfer on every x-point of the waveplate

$$M(\theta_{C(x)}, \Gamma) = R(-\theta_C(x))\ G(\Gamma)\ R(\theta_C(x)) \tag{2.33a}$$

$$= e^{-i\frac{\pi}{2}} \cdot \begin{pmatrix} \cos(\mathbf{K}x) & \sin(\mathbf{K}x) \\ \sin(\mathbf{K}x) & -\cos(\mathbf{K}x) \end{pmatrix}, \tag{2.33b}$$

where in this expression, the first and third are rotational matrices

$$R(\theta_C(x)) = \begin{pmatrix} \cos(\theta_C(x)) & \sin(\theta_C(x)) \\ -\sin(\theta_C(x)) & \cos(\theta_C(x)) \end{pmatrix} \tag{2.34}$$

and

$$G(\Gamma) = \begin{pmatrix} \exp(+i\Gamma/2) & 0 \\ 0 & \exp(-i\Gamma/2) \end{pmatrix}. \tag{2.35}$$

The wave-plate retardation $\Gamma(\lambda_0) = k_0(n_e(\lambda_0) - n_o(\lambda_0))d = \pi$ meets the half wave condition at λ_0 (a full wave is 2π), where $k_0 = 2\pi/\lambda_0$, and d is the wave-plate thickness, $d = \pi/k_0(n_e(\lambda_0) - n_o(\lambda_0))$.

Now we may prepare an incident electric field entering the wave-plate, starting from the definition of a Jones vector expression from an electric field

$$\vec{\mathbf{E}} = [E_{0x}e^{i\phi_x}\hat{x} + E_{0y}e^{i\phi_y}\hat{y}]\ e^{i(kz-\omega t)} \tag{2.36a}$$

$$= \tilde{\mathbf{E}}_0\ e^{i(kz-\omega t)} \tag{2.36b}$$

where $k = 2\pi/\lambda$, speed of light $c = \omega/k$. The Jones vector expresses the polarization in $\hat{x}, \hat{y}$

$$\tilde{\mathbf{E}}_0 = \begin{pmatrix} \tilde{E}_{0x} \\ \tilde{E}_{0y} \end{pmatrix} = \begin{pmatrix} E_{0x}e^{i\phi_x} \\ E_{0y}e^{i\phi_y} \end{pmatrix} = E_0 e^{i\phi_x} \begin{pmatrix} \cos\chi \\ e^{i\phi}\sin\chi \end{pmatrix} \tag{2.37}$$

, where $\chi = \tan^{-1}(\mathrm{E}_{0y}/\mathrm{E}_{0x})$and $\phi = \phi_y - \phi_x$.

With an incident to a polarization element with transfer matrix $M(\theta_C(c), \Gamma)$, the output electric field will have the relation $\tilde{\mathbf{E}}_{\text{out}} = M(\theta_C(x), \Gamma)\tilde{\mathbf{E}}_{\text{in}}$. We may then express a circularly polarized incident beam and its output through a single CDW by

$$\tilde{\mathbf{E}}_{\text{in}} = \frac{1}{\sqrt{2}}E_0 \begin{pmatrix} 1 \\ \pm i \end{pmatrix} \tag{2.38a}$$

$$\tilde{\mathbf{E}}_{\text{out}} = \frac{1}{\sqrt{2}}E_0 e^{-i\pi/2} e^{\pm i\mathbf{K}x} \begin{pmatrix} 1 \\ \mp i \end{pmatrix} \tag{2.38b}$$

Since we assume the incident is perfectly circularly polarized light, $\cos\chi = \sin\chi = 1/\sqrt{2}$ is applied.

The emerging polarization from the wave-plate thus changes into the opposite polarization handedness, carrying a linear phase of $\psi_x = \pm\mathbf{K}x$ and a constant phase $\pi/2$ due

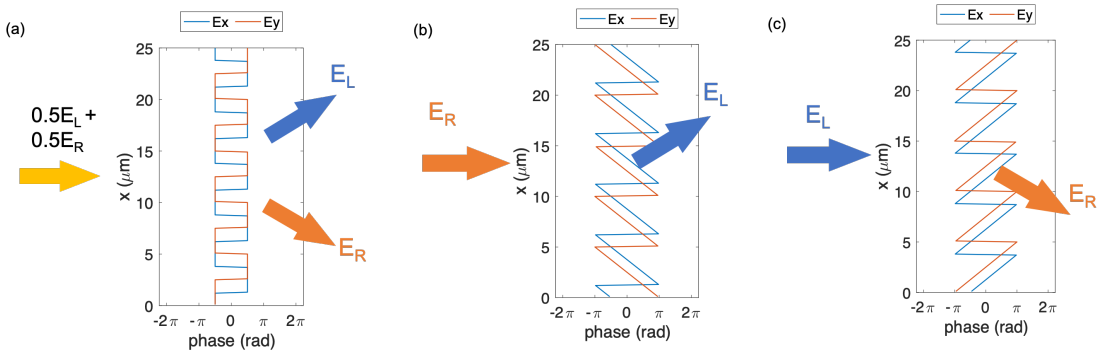

Figure 2.11: The x and y components of the output electric field phase of a $\Lambda = 5\mu$m CDW with a positive $\mathbf{K}$ vector, when the incident fields are (a) non-polarized (b) right-circularly polarized and (c) left circularly polarized. The circularly polarized inputs (b-c) results in output linear phase of $\psi_x = \pm\mathbf{K}x$, wrapped from $-\pi$ to π.

to the half-wave plate condition. A simple example visualization for the output linear phase along x for a CDW with $\mathbf{K} = 2\pi/\Lambda$ where $\Lambda = 5\mu$m is provided in Fig. 2.11 to show cases when the incident electric fields are either handed circular polarization, $E_R = 1/\sqrt{2}E_0(1; -i)$, $E_L = 1/\sqrt{2}E_0(1; i)$, and a uniform combination of both, which is unpolarized. It may be observed that the output linear phase changes sign when switched between two circular polarization inputs. The output linear phase cancels out and behaves like a regular ruled grating when the incident light is unpolarized.

By using the Fourier series expansion on the emerging electric field,

$$\tilde{\mathbf{E}}_{\text{out}} = \sum_{m=-\infty}^{m=\infty} a_m \exp\left(im\mathbf{K}x\right), \text{ where} \tag{2.39a}$$

$$a_m = \Lambda^{-1} \int_{-\Lambda/2}^{\Lambda/2} |\tilde{E}_{\text{out}}| \exp(im\mathbf{K}x)dx, \tag{2.39b}$$

we may define the diffraction efficiency of the m-th order is defined as $\eta_m = |a_m|^2/|\tilde{\mathbf{E}}_0|^2$.

By calculation, the diffraction efficiency $\eta_m = 1$ into a single diffractive order, while the diffraction efficiencies into other orders are zero. For example in Fig. 2.11 where $\mathbf{K} = 2\pi/\Lambda\hat{x}$, a right-hand circularly polarized incidence beam diffracts into $m = +1$ and a left-hand circularly polarized incidence beam diffracts the $m = -1$, both with 100% efficiency.

Cycloidal diffractive wave-plates directors can also be aligned under different symmetries. Besides rotating along linear x-axis as a linear diffraction grating, it can also rotate with respect to the azimuth angle as $\mathbf{n}(\theta_C)$ (see Fig. 2.10(b)) under polar coordinates, or along a tilted axis in the xy-plane as $\mathbf{n}$(x,y) to be an 2-D cycloidal grating. The axial director alignment forms a radial diffraction grating, where the diffraction forms a conical shape, diffracting either inwards (-r direction) or outwards ($+r$ direction) as an positive or negative axicon. Under the context of a diffractive sail, photon momentum transfer along the radial direction may be useful for sail stability purposes.

2.3.4 Bianisotropic Metamaterial Grating

Metamaterials composites of sub-wavelength units, which manipulates electromagnetic wave propagation with its geometry and arrangement, and forms captivating devices with optical properties that are not present in materials available in nature. The unique properties of these metamaterials can be attributed to their effective electrical permittivity and their magnetic permeability, which can be tuned, allowing for a variety of interesting effects. One interesting phenomena is that metamaterial gratings have the ability to support multiple resonances, and shown to be crucial for asymmetric light scattering.

Owing to the small structure of the units, the polarization in a specific location inside material depends not only on the local electric field at that location, but also on the field at

other neighboring locations. This enables controllable strong spatial dispersion, i.e. non-local polarization response, which achieves two important phenomena: artificial magnetism and bianisotropy [12] Artificial magnetism provides the possibility of creating materials with strong magnetic properties in an arbitrary frequency range, enabling negative-index materials, subwavelength focusing and other. Metasurfaces which exhibit a magnetic (electric) polarization current when excited by an electric (magnetic) field are named bianisotropic, which enables perfect refraction and reflection of incident plane wave [11, 123].

The bianisotropic behavior is modeled by cross-coupling magnetoelectric and electromagnetic parameters such as effective susceptibilities, polarizabilities, etc. The full synthesis and analysis is out of the scope of this thesis, but below we provide an illustrative example of the susceptibility tensor analysis on a bianisotropic metasurface with an incident p-polarized light, which can be tailored to three different sets of incident angles [8].

$$P = \chi_{ee} \cdot \boldsymbol{E}_{av} + \chi_{em} \cdot \boldsymbol{H}_{av}/c_0, \tag{2.40a}$$

$$M = \chi_{mm} \cdot \boldsymbol{H}_{av} + \chi_{me} \cdot \boldsymbol{E}_{av}/\eta_0, \tag{2.40b}$$

where P and M are the polarization density and the magnetization density; $\boldsymbol{E}_{av}$ and $\boldsymbol{H}_{av}$ are the average (local) electric and magnetic fields on both sides of the metasurface; χ_{ee}, χ_{mm} , χ_{em} and χ_{me} are the electric, magnetic, electromagnetic, and magneto-electric polarizability tensors of the metamaterial unit. The boundary conditions for a bianisotropic metasurface may be described by zero-thickness continuity conditions. For a

metasurface lying on the xy-plane (z=0), the conditions are

$$\hat{z} \times \triangle \boldsymbol{H} = j\omega P_{\parallel} - \hat{z} \times \bigtriangledown_{\parallel} M_z, \tag{2.41a}$$

$$\triangle \boldsymbol{E} \times \hat{z} = j\omega\mu_0 M_{\parallel} - \bigtriangledown_{\parallel} (P_z/\epsilon_0) \times \hat{z} \tag{2.41b}$$

where $\triangle \boldsymbol{E}$ and $\triangle \boldsymbol{H}$ are the differences of the electric and magnetic fields on the both sides of the metasurface.

As an example we can consider a p-polarized incident plane wave to the surface, where non-zero electromagnetic field components are E_x, E_z, and H_y. The relevant susceptibilities (consider Eq.2.40b) are

$$\chi_{ee} = \begin{bmatrix} \chi_{ee}^{xx} & 0 & \chi_{ee}^{xz} \\ 0 & 0 & 0 \\ \chi_{ee}^{zx} & 0 & \chi_{ee}^{zz} \end{bmatrix}, \chi_{em} = \begin{bmatrix} 0 & \chi_{em}^{xy} & 0 \\ 0 & 0 & 0 \\ 0 & \chi_{ee}^{zy} & 0 \end{bmatrix}, \quad \chi_{me} = \begin{bmatrix} 0 & 0 & 0 \\ \chi_{me}^{yx} & 0 & \chi_{me}^{yz} \\ 0 & 0 & 0 \end{bmatrix}, \chi_{mm} = \begin{bmatrix} 0 & 0 & 0 \\ 0 & \chi_{mm}^{yy} & 0 \\ 0 & 0 & 0 \end{bmatrix}, \tag{2.42a}$$

If we substitute the above susceptibilities into Eq. 2.40b with the conditions Eq. 2.41b, the original equation can be reduced to two equations of

$$\triangle H_y = -j\omega\epsilon_0(\chi_{ee}^{xx} E_{x,av} + \chi_{ee}^{xz} E_{z,av}) - jk_0 \chi_{em}^{xy} H_{y,av} \tag{2.43a}$$

$$\triangle E_x = -j\omega\mu_0 \chi_{mm}^{yy} H_{y,av} + jk_0(\chi_{em}^{xy} E_{x,av} + \chi_{em}^{zy} E_{z,av}) - \chi_{ee}^{xz} \partial_x E_{z,av} - \eta_0 \chi_{em}^{zy} \partial_x H_{y,av} \ , \tag{2.43b}$$

These two equations can be solved for 6 unkown susceptibilities for three independent sets of incident, reflected and transmitted waves, and the transmission and reflection

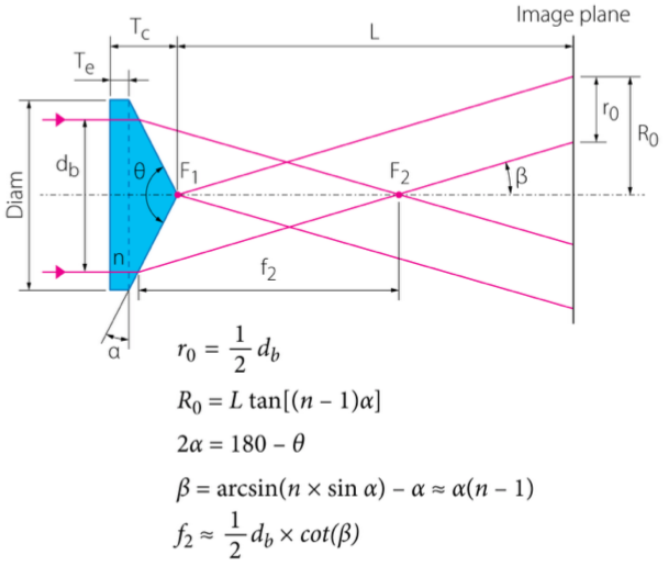

Figure 2.12: Schematic of a conventional refractive axicon, characterized by the apex angle θ. Image adapted from [10].

coefficients can be specified.

2.3.5 Axicon Radial Grating

First proposed in 1954 by John McLeod [100], axicons are conventionally achieved by a cone glass with an apex angle, which like a rotationally symmetric prism it refracts light inwards. Unlike lens that creates a focal point, an axicon creates a focal line extended along the optical axis for a certain range. The far-field diffraction of the refracted light becomes a ring-shaped beam, which is of interest in applications including laser manipulation of microscopic objects [93, 138], laser corneal surgery [128], laser machining [129], etc.

The extended focal depth of the beams are sometimes referred to as "diffraction-free" Bessel beams, for that the transverse beam intensity profile doesn't change with elongated

propagation. Bessel beam imaging is distinguished from Gaussian beam imaging in that it enables extension of the focusing range without loss of resolution [81]. A conventional refractive axicon is shown in Fig. 2.12, where θ is the apex angle, β is the cone angle. With a incident beam of diameter d_b, depth of focus f_2 (the elongated focal length) may be determined, and R_0 is the outer radius of the ring that the beam forms.

Unlike a refractive axicon, which is defined with an apex angle or a cone angle, a diffractive axicon can be viewed as essentially a radial grating is defined by its diffractive angle, which can be calculated from the diffraction grating equation:

$$\theta_d = \sin^{-1}(m\lambda/\Lambda) \tag{2.44}$$

The first diffractive order of an axicon may be defined as $m = |m|\hat{r} = +1$ where light is diffracted radially outwards or $m = -|m|\hat{r} = -1$ where light is diffracted radially inwards.

While a cone glass axicon refracts light towards the optical axis(Fig.2.13), a blazed axicon grating could have $m = -1$ or $m = +1$ as a positive or negative axicon (Fig. 2.13(b-c)), and diffractive orders $m = \pm 1$ both exists for a regular axicon grating with pillared phase profile (Fig. 2.13(d)). Although all (a-d) cases form a ring diffraction pattern, if we point a beam at the same coordinate on respective diffractive axicon gratings, they would experience different radiation pressure force determined by Eq. 4.2. For example, the top-half an positive axicon experiences an upward tangential force, while the top-half of a negative axicon experiences a downward tangential force; for a radial grating with pillared phase profile equally diffracting into $m = \pm 1$ orders, zero tangential force is experienced, as force towards opposite tangential directions cancel another.

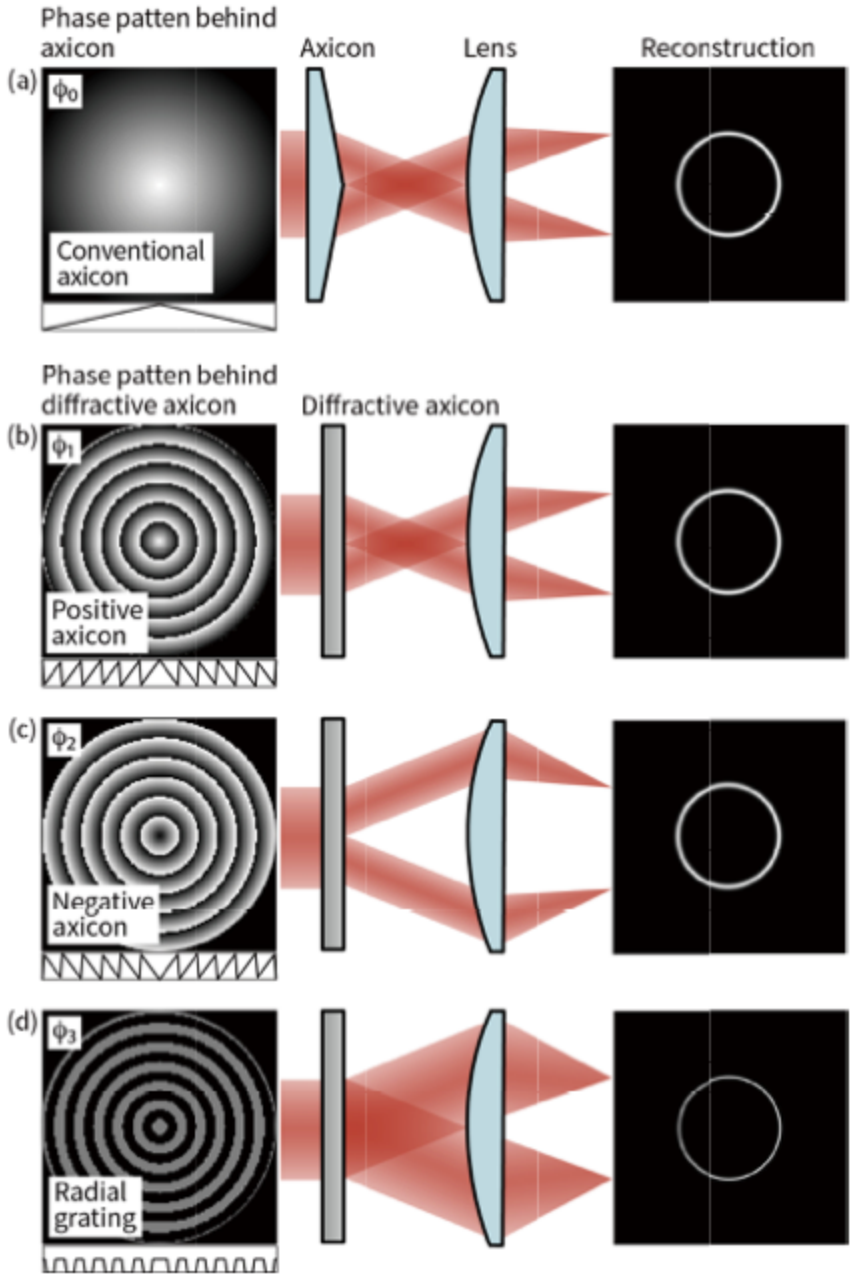

Figure 2.13: The phase profile and diffraction patterns from (a) Conventional axicon. (b) Positive diffractive axicon, diffracts inwards. (c) Negative diffractive axicon, diffracts outward. (d) Radial grating. adapted from [59]

Chapter 3

Radiation Pressure on Diffractive Solar Sails

3.1 Momentum Transfer on a Sun-facing diffractive sail

Having explored the governing radiation pressure force on a diffraction grating, we further explore the performance of an ideal sail on orbital trajectories. The goal is to explore space missionary cases where a diffractive sail may be beneficial over a reflective sail through modelling the orbital trajectories. Decadal survey of NASA for Solar and Space Physics advocated for the importance of advanced solar sails for solar polar imaging to enable heliophysics studies [22]. To date, the Ulysses spacecraft is the only mission to have focused on the solar poles, ending in 2009 at 1.3AU [73]. While Ulysses did not hold any imagers, the European Space Agency (ESA) has stitched together the only image of solar north pole using data from Proba-2 satellite observatory. This will change in the near future, as the joint NASA-ESA Solar Orbiter lauched in Feburary 2020 will reach a

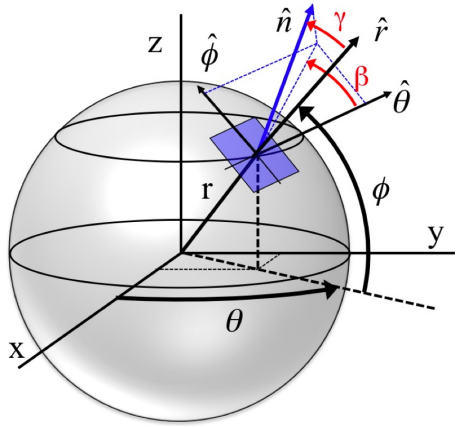

Figure 3.1: A solar sail in a heliocentric spherical coordinate. The solar sail surface normal $\hat{n}$ makes an angle γ to the radial vector $\hat{r}$ of the spherical coordinate. The tangential surface of the solar sail lies in the plane formed by $\hat{\theta}$ and $\hat{\phi}$, where the $\hat{p}$ vector (not shown) forms a control angle β to $\hat{\theta}$.

24 degree inclination in 7 years [3, 107].

Motivated by a sun-facing diffractive sail (as depicted in Fig. 1.2), we consider a simple system of the sun and a light sail placed in heliocentric spherical coordinates, as depicted in Fig. 3.1. The r, θ, and ϕ respectively represent the radial distance from the sun, longitude, and latitude of the sailcraft. Recall in the last chapter, Fig.2.2, we defined the unit vectors parallel and normal to the diffraction grating as $\hat{p}$ and $\hat{n}$ respectively. Now they can be re-expressed as $\hat{p} = \cos\beta\hat{\theta} + \sin\beta\hat{\phi}$and $\hat{n} = \cos\gamma\hat{r} + \sin\gamma\cos\beta\hat{\theta} + \sin\gamma\sin\beta\hat{\phi}$, considering $\hat{p}$ lies parallel to the surface formed by $\hat{\theta}$ and $\hat{\phi}$, and $\hat{n}$ makes an angle γ to the radial vector $\hat{r}$.

In general the solar radiation pressure force $\vec{F_{rp}}$ on the light sail is directly proportional to the solar irradiance $I(r)$, sail area A_s, and the momentum transfer efficiency vector

$\eta = \eta_r \hat{r} + \eta_\theta \hat{\theta} + \eta_\phi \hat{\phi}$. For a reflective sail,

$$\vec{\eta_R} = 2\cos^2\gamma \hat{n} = 2\cos^2\gamma(\cos\gamma \hat{r} + \sin\gamma(\cos\beta_R \hat{\theta} + \sin\beta_R \hat{\phi}) \tag{3.1}$$

The maximum transverse component of force (perpendicular to $\hat{r}$) occurs when $\gamma = 35.25°$, providing a transverse (radial) efficiency value of $\eta_{R,\perp} = 2\cos^2\gamma\sin\gamma = \pm 0.77$ ($\eta_{R,r} = 2\cos^3\gamma = 1.09$) [99].

For a diffractive sail given by Chap 1,

$$\vec{\eta_D} = (1 \pm (1 - (m\lambda/\Lambda)^2)^{1/2})\hat{r} - (m\lambda/\Lambda)(\cos\beta_D \hat{\theta} + \sin\beta_D \hat{\phi}) \tag{3.2}$$

A diffractive sail, assumed to have 100% incident power diffracted to a single order, has maximum tangential efficiency when $m\lambda/\Lambda$=1, and $\eta_\perp = 1.00$, the corresponding radial efficiency is η_r=1.00.

We may now combine the two forces that affects the light sail, the radiation pressure and the gravitational force between the sun and light sail, and express them as

$$F_r = -GMm_s/r^2 + (I_E R_E^2 As/cr^2)\eta_r = -(GMm_s/r^2)(1 - \alpha_r) \tag{3.3a}$$

$$F_\theta = (I_E R_E^2 As/cr^2)\eta_\theta = (GMm_s/r^2)\alpha_\theta \tag{3.3b}$$

$$F_\phi = (I_E R_E^2 As/cr^2)\eta_\phi = (GMm_s/r^2)\alpha_\phi, \tag{3.3c}$$

where we expressed $I(r) = I_E R_E^2/r^2$, $I_E = 1.37\text{kW/m}^2$ is the so-called solar constant. Here we may incorporate the definition of a lightness number σ^*, where $\sigma^* = \sigma_{cr}/\sigma$, $\sigma_{cr} = 2I_E R_E^2/GMc = 1.54\text{g/cm}^2$ and $\sigma = m_s/A_s$. The equal signs in the equations give $\alpha_r = \sigma^*\eta_r/2$, $\alpha_\theta = \sigma^*\eta_\theta/2$, and $\alpha_\phi = \sigma^*\eta_\phi/2$.

The equation of motion incorporating the combined forces can then be written:

$$\ddot{r} = r\dot{\theta}^2 \cos^2\phi + r\dot{\phi}^2 - (1-\alpha_r)\mu/r^2 \tag{3.4a}$$

$$\ddot{\theta} = 2\dot{r}\dot{\theta}/r - 2\dot{\phi}\dot{\theta}\tan\phi - |\sin\theta|\alpha_\theta\mu/(r^3\cos\phi) \tag{3.4b}$$

$$\ddot{\phi} = (2\dot{r}\dot{\phi} + r\dot{\theta}^2 \sin\phi\cos\phi - \alpha_\phi\mu\cos\theta/r^2)/r \tag{3.4c}$$

The equations are solved with the MATLAB ode23t Runge-Kutta solver under initial conditions of position and velocity components: $[r,\theta,\phi,\dot{r},\dot{\theta},\dot{\phi}]=[0,0,R_E,0,v_E,0]$, where $v_E = (G/R_E^3)^{1/2}$ is the Earth velocity and G is the gravitational constant. We consider a 6U CubeSat sailcraft, similar to the NASA NEA-Scout design, where sail mass m_s=14 kg but with a larger sail area (400 m^2 instead of 86 m^2), and so the lightness number $\sigma^\star = 0.044$. Using the maximum transfer efficiencies for a reflective sail, we have $(\alpha_r, \alpha_\theta, \alpha_\phi) = (0.022, -0.0169, 0.0169)$; for a maximum transfer efficiency diffractive sail $(\alpha_r, \alpha_\theta, \alpha_\phi) = (0.022, -0.022, 0.022)$.

Simulation results are shown in Fig.3.2. A diffractive sail reaches 60° inclination and lowers to 0.32 AU in 5 years, where as the reflective sail reaches 33° and lowers to 0.42 AU in the same time. The results show that a diffractive sail are more efficient on a inclination inclination cranking and orbit lowering mission, which makes it a strong candidate for a solar polar imaging mission, working its way towards the poles of the sun and getting near to it faster than a reflective sail.

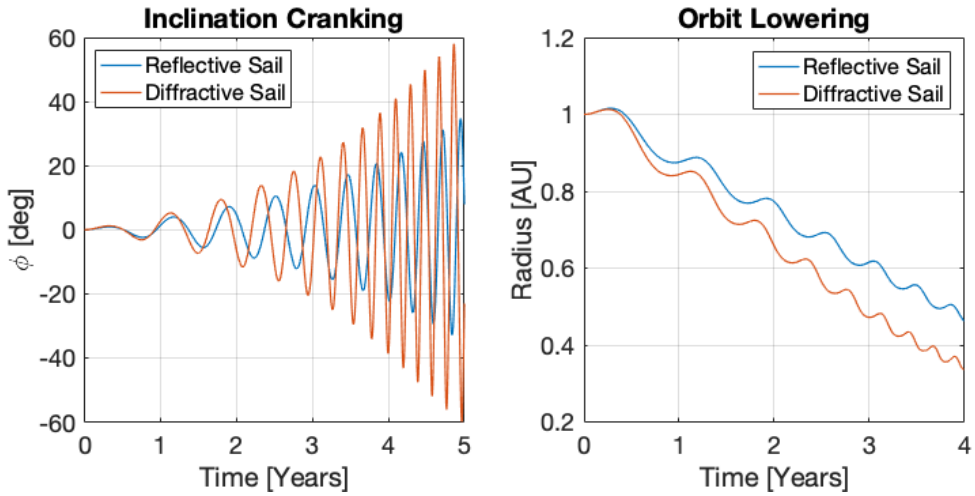

Figure 3.2: Inclination cranking and orbit lowering simulation results for maximum transfer efficiencies. Diffractive sail reaches 60° inclination and lowers to 0.32 AU in 4 years, where as the reflective sail reaches 33° and lowers to 0.42 AU in the same time.

3.2 Liquid Crystal CDW Solar Sails

Liquid crystal cycloidal diffractive waveplates (CDW) are relatively mature candidate to realize a light sail due to its ability to be made in large areas upon exposure, and that liquid crystal are able to hold on flexible substrates [151]. In Section 2.3.3, we also described how CDWs meet the half-wave condition at the designed wavelength, making its ultrathin and lightweight as the thickness is the order of wavelength. Theoretical diffraction efficiency is unity into a single diffractive order, which is ideal for momentum transfer efficiency. The constraints of CDWs are diffraction efficiencies wavelength-dependent, and that the diffraction requires the incident beam being only left (or right) circularly polarized. We discuss the polarization dependent momentum transfer and the possibility to achieve polarization independent momentum transfer. Furthermore, assuming single polarization incidence, we discuss the achromatic properties of an beam.

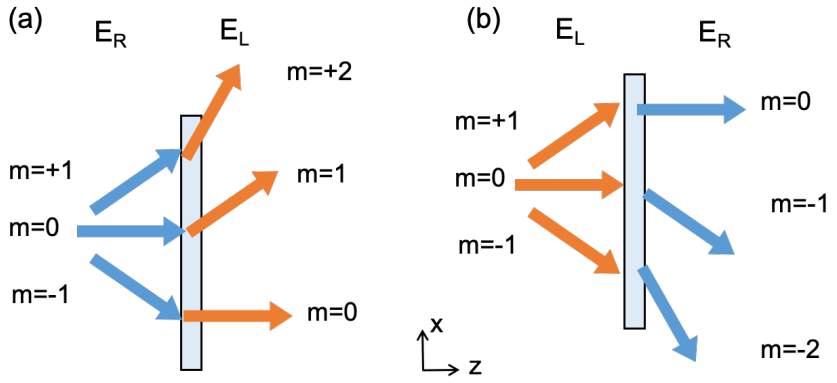

Figure 3.3: For a CDW with $\mathbf{K} = 2\pi/\Lambda\ \hat{x}$, where (a) incident right-hand circularly polarized beam experiences a raise in diffractive mode order, while (b) left- hand polarized beam experiences a drop in diffractive mode order. Blue arrows stand for E_R beams and orange arrows stand for E_L beams.

3.2.1 Polarization Independent CDW Sails

Since CDWs are polarization sensitive, the perfect diffraction efficiency could only be applied to half of the flux from an unpolarized incident light, e.g., under the case of solar sailing with sunlight as the light source. We propose a method to achieve polarization independent diffraction, i.e., utilizing both the left and right circularly polarized portion of the incident light for momentum transfer. This method contains three layers – two identical CDW grating layers, sandwiching a birefringent phase retarder that is incident-angle selective. We will first discuss the sandwiched retardation layer from the definition of its birefringent properties, and then describe the three layered system.

Polarization Dependent Momentum Transfer

We've discussed in Section 2.3.3 that for CDWs are polarization selective as well as that only m=+1,0,=1 diffractive modes exist. By far, the discussion surrounds normal incident

beams (middle rays in Fig. 3.3). It could be pointed out that even with beams of different incident angles, if we assume a fixed circular incident polarization, the momentum transfer equation $(\vec{k}_i + m\vec{\mathbf{K}}) \cdot \hat{p} = \vec{k}_m \cdot \hat{p}$ indicates a constant momentum change when diffracted into the same order. Diffractive angles such as second mode diffraction may exist, for example, when normal incidence $\theta_i = 0°$, we have $\sin\theta_1 = \lambda/\Lambda$ diffracted into m=1. If we further take $\theta_i = \theta_1$, the diffracted angle to first order $\sin\theta_1' = \sin\theta_1 + \lambda/\Lambda = 2\lambda/\Lambda$, is equal to a second order diffraction under normal incidence $\sin\theta_2 = 2\lambda/\Lambda$. For the purpose of convenience in deriving a polarization independent sail, we label the incident ray with $\theta_i = \theta_1$ as m=1 , and the diffracted ray as m=2 (top ray, Fig. 3.3(a)). Similarly, an incident ray of $\theta_i = -\theta_1$ is labelled as m=-1, its diffracted ray is normal to the sail surface and labelled as m=0 (bottom ray, Fig. 3.3(a)). The summary of labels are provided in Fig. 3.3 , but note that all momentum changes with right circular polarized incident remains $\vec{\mathbf{K}}$, and left circular polarized incident remains $-\vec{\mathbf{K}}$.

Below we derive and discuss in terms of electric fields with Jone's Matrix analysis. Since CDWs are polarization sensitive to left and right circularly polarized light, it is convenient to express the electric fields on to the Left-circular and Right-circular basis,

$$\hat{R} = \frac{1}{\sqrt{2}} \begin{pmatrix} 1 \\ -i \end{pmatrix} \begin{pmatrix} \hat{x} \\ \hat{y} \end{pmatrix}, \hat{L} = \frac{1}{\sqrt{2}} \begin{pmatrix} 1 \\ +i \end{pmatrix} \begin{pmatrix} \hat{x} \\ \hat{y} \end{pmatrix} \tag{3.5}$$

As an example, a purely right-circular polarized input electric field and its output field

from a single cycloidal diffractive waveplate may be rewritten from Eq. 2.38b:

$$\tilde{\mathbf{E}}_{\text{in}} = \frac{1}{\sqrt{2}} E_0 \begin{pmatrix} 1 \\ -i \end{pmatrix} = E_0 \hat{R} \tag{3.6a}$$

$$\tilde{\mathbf{E}}_{\text{out}} = \frac{1}{\sqrt{2}} E_0 e^{-i\pi/2} e^{-i\mathbf{K}x} \begin{pmatrix} 1 \\ +i \end{pmatrix} = E_0 e^{-i\pi/2} e^{-i\mathbf{K}x} \hat{L} \ , \tag{3.6b}$$

where the linear phase $e^{-i\mathbf{K}x}$ indicates a $m = 1$ order diffraction. If the same calculation is performed on an incident right-circular polarized electric field carrying $e^{(-i\mathbf{K}x)}$as if already diffracted to the $m = 1$ mode,

$$\tilde{\mathbf{E}}_{\text{in}} = E_0 e^{-i\pi/2} e^{-i\mathbf{K}x} \hat{R} \tag{3.7a}$$

$$\tilde{\mathbf{E}}_{\text{out}} = E_0 e^{-i\pi} e^{-i2\mathbf{K}x} \hat{L} \ , \tag{3.7b}$$

the linear phase $e^{-i2\mathbf{K}x}$ indicates a diffraction towards the $m = 2$ angle when normal incidence. Similarly, an incident field carrying $e^{(i\mathbf{K}x)}$ travelling towards $-\hat{x}$ as if already diffracted to $m = -1$ mode, would have linear x phase cancelled and we have the diffracted output normal to the surface ($m = 0$).

It is tempting to increase the momentum transfer efficiency by stacking layers alternating between $\pm\vec{K}$ to add up the effects of $\vec{K}$ and achieve the momentum transfer of higher orders. However, for an unpolarized incident light, momentum transfer would always be cancelled for CDW's beam-splitting behavior. The required single circular polarization incidence for single-order diffraction indicates that in practice, two pre-layers, linear polarizer and quarter waveplate layer, would be required before the CDW. Since only 50%

of unpolarized irradiance is being used for redirection of beam power, potential problems may regard absorption of half of the solar irradiance. Polarization independent diffraction that utilizes both orthogonal polarization components is far more practical and desirable for solar sailing purposes.

Three-Layer Polarization Independent Diffraction Layout

Optically anisotropic material has optical properties that are not the same in all directions. If a light beam enters into anisotropic crystal, the electric displacement vector $\vec{D} = [\epsilon_{ij}]\vec{E}$, where ϵ_{ij} is a tensor. By rotating the coordinate system, the tensor may be simplified to have only diagonal elements ϵ_{ii}, where the rotated coordinate system now defines the principal axes of the crystal. The principal dielectric constants ϵ_{ii} corresponds to principal indices of refraction $n_i = \sqrt{\epsilon_{ii}}$. If $n_1 = n_2 \neq n_3$, the crystal is called uniaxial. Usually indices $n_1 = n_2 = n_o$ and $n_3 = n_e$ are called the ordinary and extraordinary indices. If $n_e < n_o$ the crystal is negative uniaxial, if $n_e > n_o$ it is positive uniaxial crystal.

If unpolarized light beam enters into uniaxial crystal, the beam will be split into two parts (ordinary and extraordinary), polarized at orthogonal to each other. In an ordinary beam the electric field will be polarized perpendicular to the optic axis and will have a phase velocity independent of the direction. In an extraordinary beam the electric field will be polarized in the same plane as the optic axis and will have a phase velocity depending on the direction of propagation.

Let us consider a positive uniaxial crystal on the axes x', y', z' shown in Fig. 3.4 (a) with its index ellipsoid given by

$$\frac{x'^2 + y'^2}{n_o^2} + \frac{z'^2}{n_e^2} = 1 \tag{3.8}$$

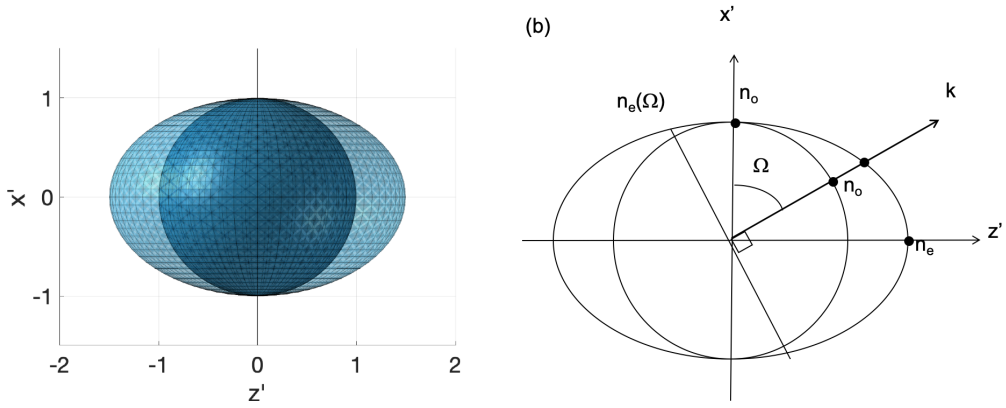

Figure 3.4: (a) Index ellipsoid of an uniaxial crystal shown on the $x' - z'$ perspective. (b) The ordinary and extraordinary indices defined on the index ellipse, where k shows a ray propagating at an angle Ω from x' axis.

Since we are discussing light diffracted in the $x' - z'$ plane, the . Solving for the index of refraction as a function of angle Ω between optical axis and direction of propagation $\hat{k}$ leads to

$$\frac{1}{n_e(\Omega)^2} = \frac{\cos^2\Omega}{n_o^2} + \frac{\sin^2\Omega}{n_o^2} \tag{3.9}$$

For the purpose of creating a phase retardation difference between two beams with different incident angles, we tilt the index ellipsoid x', y', z'coordinates by the angle Ω with respect to the x axis of the CDW placement. As shown in Fig. 3.4 (b), the tilted x'allows the incident E_L and E_R beams, splitted from the first CDW into angles θ_d above and below the z axis, to experience π and 2π phase retardation respectively. The π retardation switches the incident E_L beam to the orthogonal E_R polarization, and the 2π retardation allows the incident E_R beam to remain its polarization. The polarization of both beams are turned into E_R and the propagation angle remains the same.

In this three-layered composition, the unpolarized light is split into two diffracted

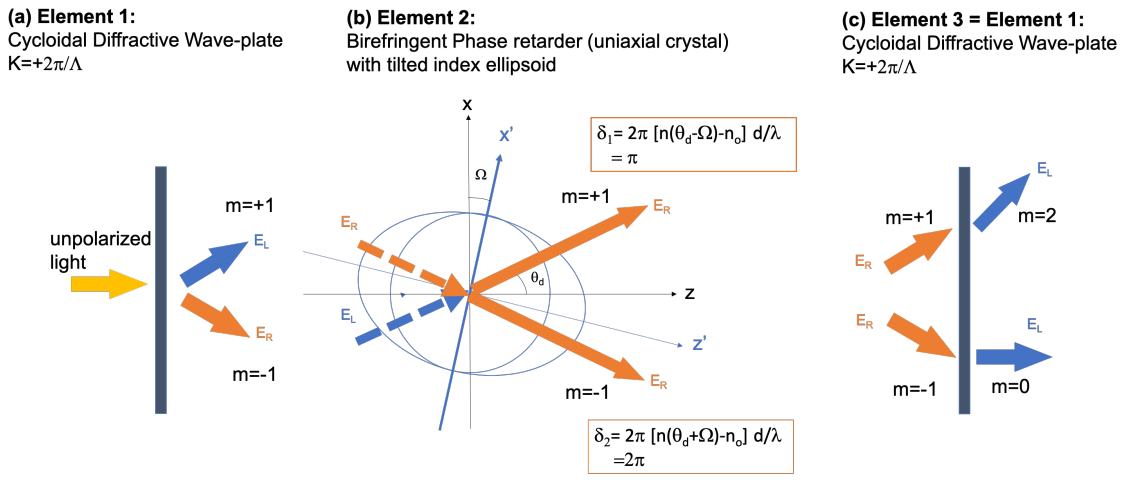

Figure 3.5: Ray propagating in a 3 layer anisotropic configuration for a polarization independent CDW diffractive sail.

beams with orthogonal polarizations (element 1, Fig. 3.5(a)) of $m = \pm 1$ orders, then both beams are turned into the same polarization (element 2, Fig. 3.5 (b)). Once the rays are both the same polarization, the tangential momentum transfer of a single CDW (element 3, Fig. 3.5 (c)) is equal on both rays. Thus the $m = \pm 1$ orders both raises up an order and becomes $m = 2$ and $m = 0$.

We may finally compare the momentum transfer between two three-layered systems. The polarization dependent case of a single CDW preceded with a linear polarizer and quarter wave plate; and the polarization independent case of two CDWs sandwiching an incident-angle selective birefringent retarder. Consider 0.5 of incident power goes to the two beams in the beam-splitting process, and unity efficiency for all other transfers. In the former case, half of the incident beams experiences momentum change $\mathbf{K}$ so the total momentum change is 0.5 $\mathbf{K}$; in the latter case, individual halves of the beam experience

$2\mathbf{K}$ and no change respectively, so the net momentum change is 1 $\mathbf{K}$. We show that under this three-layered composition, the momentum transfer efficiency has doubled, compared to using polarizer, quarter wave plate and CDW only to achieve 0.5 $\mathbf{K}$ momentum change.

3.2.2 Achromatic diffraction and force efficiency under the solar spectrum

In solar sailing, a broadened efficiency curve is desirable to better utilize the solar photons across the spectrum. We provide a how a single CDW spectral efficiency is, and then discuss the conditions where the diffractive efficiency curve may be broadened as achromatic diffraction, and how the solar force efficiency may be affected. For simplification purposes in the analysis below, we only focus the chromatic effects, and ignore the effects of polarization by assuming a single circularly-polarized input.

Let us consider a general Jones transfer matrix of a single CDW with a wave number dependent expression, using Eq. 2.33

$$M(\theta_C(\mathbf{K},x),\Gamma(k)) = \begin{pmatrix} \cos(\gamma) & 0 \\ 0 & \cos(\gamma) \end{pmatrix} - i\sin(\gamma) \begin{pmatrix} \cos(2\theta_C) & \sin(2\theta_C) \\ \sin(2\theta_C) & -\cos(2\theta_C) \end{pmatrix} \begin{pmatrix} \hat{x} \\ \hat{y} \end{pmatrix} \quad (3.10)$$

where $\gamma = \pi k/2k_0$ and $\theta_C = \mathbf{K}x/2 + \Delta\theta_C$, $k_0 = 2\pi/\lambda_0$ stands for the wave-number that matches the half-wave condition. As the thickness d remain fixed, a broad-band light source diffracting though this wave-plate would not meet the half-wave retardation condition at all wave numbers besides k_0. To characterize the retardation as a function of wavelength, we write

$$\Gamma(k) = k(n_e(k) - n_o(k))d \quad (3.11)$$

, where $k = 2\pi/\lambda$ and $d = \pi/k_0(n_e(k_0) - n_o(k_0))$.

For the entire section of chromatic diffraction discussion, we assume purely right-circular polarized incident light. The expression of a purely right-circular polarized input electric field at the designated wave number k_0, and its emerging field from a single cycloidal diffractive waveplate may be rewritten from Eq. 3.6b.

The emerging electric field may be generalized into $\tilde{\mathbf{E}}_{\text{out}}(\lambda, x) = M(\theta_x(\mathbf{K}, x), \Gamma(\lambda))\tilde{\mathbf{E}}_{\text{in}}$ for a broad-band input and a broad band output :

$$\tilde{\mathbf{E}}_{\text{out}}(k, x) = |E_L(k)|e^{i\phi_L(k,x)}\hat{L} + |E_R(k)|e^{i\phi_R(k,x)}\ \hat{R} \tag{3.12}$$

By Eq. 2.39, the diffraction amplitude of the m-th order

$$a_{m,L}(k) = \Lambda^{-1}\int_{-\Lambda/2}^{\Lambda/2} |E_L(k)|\exp(i\phi_L(k,x))\exp(im\mathbf{K}x)dx \tag{3.13a}$$

$$a_{m,R}(k) = \Lambda^{-1}\int_{-\Lambda/2}^{\Lambda/2} |E_R(k)|\exp(i\phi_R(k,x))\exp(im\mathbf{K}x)dx\ , \tag{3.13b}$$

thus the diffraction efficiency of m-th diffractive order may be expressed as

$$\eta_{m,L}(k) = |a_{m,L}(k|^2/|E_0|^2 \tag{3.14a}$$

$$\eta_{m,R}(k) = |a_{m,R}(k)|^2/|E_0|^2 \tag{3.14b}$$

$$\eta_m(k) = (|a_{m,L}(k)|^2 + |a_{m,R}(k)|^2)/|E_0|^2\ , \tag{3.14c}$$

which will be used in calculating force efficiencies.

With the diffraction efficiencies on cycloidal diffractive waveplate defined, we move on to consider the solar radiation pressure force on such diffractive devices. Consider black-

body spectral exitance from the sun in terms of frequency, $M(\nu) = (2\pi h\nu^3/c^2)/(\exp(h\nu/k_BT)-1)$, where h and k_B are the Planck and Boltzmann constants respectively, and $k = 2\pi\nu/c$, $\nu = ck/2\pi$. We can write $M(k) = (hck^3/(2\pi)^2)/(\exp(hck/2\pi k_BT) - 1)$ and $B(k) = (R_{sun}/r)^2 M(k)$ where $R_{sun} = 6.957 \times 10^8[m]$ is the solar radius and r it the distance between the sail and the sun. The total spectral exitance from the sun may be determined by $M_{\text{sun}} = \sigma T^4$ where σ is the Stefan-Boltzman constant, and $T = 5778$[K] is the temperature of the sun. The spectral range of $k = 1.1 \times 10^6 - 6.3 \times 10^7 \mu\text{m}^{-1}$, corresponding to $\lambda = 0.1\mu\text{m} - 6\mu\text{m}$ allows us to take 99.9 % of the solar spectral exitance into consideration (i.e., $\sum M(k)/M_{\text{sun}} = 99.9\%$). Within this spectral range, we choose a characteristic wave number of the solar spectrum by the weighted average $\bar{k} = \sum(k \cdot M(k))/\sum M(k) = 9.7\mu m^{-1}$, corresponding to a characteristic wavelength $\bar{\lambda} = 2\pi/\bar{k} = 0.65\mu$m to design our diffractive waveplate.

The radiation pressure force tangential and normal to a cycloidal diffractive waveplate can then be expressed respectively by

$$F_\phi = -\frac{A\cos\theta_i}{c}\sum_m \int B(k)\ \eta_m(k)\ (mK/k)\ dk \tag{3.15a}$$

$$F_r = \frac{A\cos\theta_i}{c}\sum_m \int B(k)\ \eta_m(k)\ \left(\cos\theta_i - (1-(mK/k-\sin\theta_i)^2)^{1/2}\right)dk \tag{3.15b}$$

where $k_{min} = 2\pi m/\Lambda(1+\sin\theta_i)$ is the cut-off wave number where a smaller wave-number will not be diffracted by the cycloidal diffractive waveplate. The solar momentum transfer efficiency on a diffraction grating can then be defined as radiation pressure force over the

total flux in the spectrum

$$\eta_\Phi = F_\phi / \int B(k)dk \ (A/c) \tag{3.16a}$$

$$\eta_r = F_r / \int B(k)dk \ (A/c) \tag{3.16b}$$

Next, we are able to perform a comparison of momentum transfer efficiencies between an ideal single-order diffraction grating, a single chromatic cycloidal diffractive waveplate, and a layered achromatic diffractive waveplate. The former two are designed to the characteristic wavenumber of $\bar{k} = 9.7\mu m^{-1}$ (corresponding wavelength $\bar{\lambda} = 0.65\mu$m). In all cases we assume a grating period of $\Lambda = 1\mu$m [147] where solar momentum is most efficiently used, and for the waveplates birefrigence is assumed as $\Delta n = n_e - n_o = 0.15$. We also assume a sun-facing diffractive sail of normal incidence $\theta_i = 0$ and $r = 1$ A.U. as the sail is launching from Earth.

An ideal single-order diffraction grating where the diffraction efficiency of a single m=+1 order is 100% across the spectral range, will be the perfect "gold standard" case. We may express $\eta_1(k) = 1$, $\eta_0(k) = 0$, $\eta_{-1}(k) = 0$, and the calculated force transfer efficiency $\eta_\phi = -0.22, \eta_r = 0.09$ would be the maximum transfer efficiency possible to achieve. We are particularly interested in the tangential component η_ϕ for this component is absence in a purely reflective sail.

A single chromatic cycloidal waveplate, with spectral efficiency curves $\eta_{+1}, \eta_0, \eta_{-1}$ plotted in Fig. 3.6(left) has momentum transfer efficiency. $\eta_\phi = -0.17, \eta_r = 0.07$, where the tangential component reaches 77% of the maximum transfer efficiency. The thickness of this single waveplate is $d = 2.2\mu$m.

Based on Pancharatnum's work in 1955, an achromatic waveplate is obtained by su-

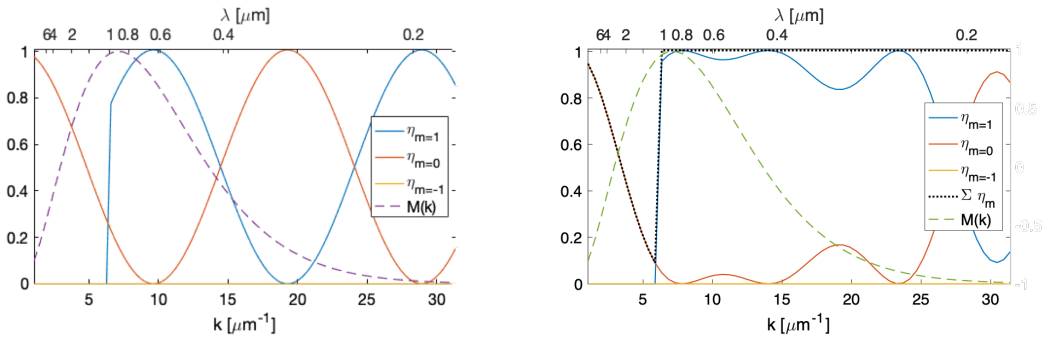

Figure 3.6: Spectral diffractive efficiency curves for chromatic (left) and achromatic CDWs (right) along with the solar spectral exitance. The diffraction cuts off at $k_{\min}$.

perposing three birefringent plates of the same material; the first and last should have the same retardation, and their fast vibration directions begin parallel to one another but inclined at a specific angle $\Delta\theta$ of the central plate. The desired range of achromatism determines the optimum values of retardation and $\Delta\theta$ [116, 117, 120]. The same principal may be applied onto cycloidal diffractive waveplates.

Since cycloidal diffractive waveplates need to meet the half-wave condition, the first and third waveplates are assumed to be half waveplates with a designed wave number k_{01}, k_{03} different from the central waveplate k_{03}. The outer waveplates having parallel fast axis while fast axes are rotating periodically, is realized by an added shift in the periodic liquid crystal cycloidal function, so that at every point along x there is a constant fast axis direction shift between the outer plates and the central plate, as depicted in Fig. 3.7. The white space in the central waveplate will still be filled with cycloidal liquid crystals, but left blank to show the shift in the cycloidal function. If the central plate has a liquid crystal cycloidal function of $\theta_2 = \mathbf{K}x/2$, then the first and third plates have a function of

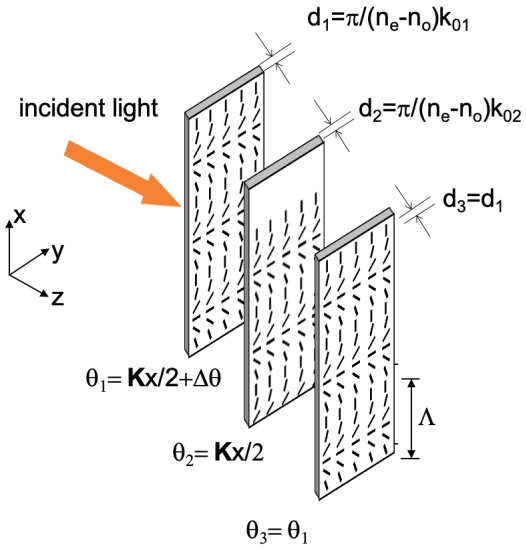

Figure 3.7: Achromatic Cycloidal diffractive waveplate with a three layered structure. The first and third wave plate has identical phase retardation and identical liquid crystal cycloidal functions in contrast to the center half waveplate.

$\theta_1 = \theta_3 = \mathbf{K}/2 + \Delta\theta$.

To achieve the maximum possible solar momentum transfer efficiency for grating period $\Lambda = 1\mu$m, we optimize over parameters and found that under the conditions of $\Delta\theta = \pi/4$, $k_{01} = k_{03} = 28\mu\text{m}^{-1}(\lambda_{01} = \lambda_{02} = 0.22\mu\text{m})$, $k_{02} = 7.8\mu\text{m}^{-1}(\ \lambda_{02} = 0.81\mu\text{m})$, the first-order diffraction efficiency $\eta_{+1}(k)$ could be raised much closer 1 across the high exitence regions of the solar spectrum, as the right side of Fig. 3.6 compares to the left. The momentum transfer efficiencies are $\eta_\phi = -0.218$ and $\eta_r = 0.094$, where the tangential transfer efficiency reaches 96% of the ideal situation. The thickness of first and third layer is $\text{d}_{01} = \text{d}_{03} = 0.75\mu$m, while the center layer $\text{d}_{02} = 2.68\mu$m, resulting in a total thickness of 4.2μm for the achromatic structure.

We show that an achromatic cycloidal diffractive waveplate structure is able to raise

the tangential momentum transfer efficiency from 77% to 96% by adding front and back layers to a single waveplate. However, there is a trade-off of almost doubling the thickness from 2.2μm to 4.2 μm.

Chapter 4

Experimental Setup and Measurements

The force measurements on a diffraction grating were conducted in a vacuum bell-jar, with a sensitive torsion pendulum to eliminate the effect of gravity which is perpendicular to the direction of torque on the pendulum. Under the effect of radiation pressure, the pendulum shifts in its equilibrium position and oscillation amplitude, which could be analyzed as a simple mechanical harmonic oscillator. A sensitive free-oscillating force measurement may be subject to convection force and photophoretic forces; possible thermal effects including absorption force and bolometric forces; and environment vibration noises. The system is carefully constructed to maintain sensitivity and avoid noise. In this chapter, the construction of this torsion pendulum and the configurations for force measurements is described. Besides using the pendulum to measure force magnitude, a large oscillation of the pendulum may be "cooled" by using the restoring force provided by optical radiation pressure on a diffractive beam-rider.

4.1 Torsion Oscillator for Radiation Pressure Measurements

4.1.1 Setup Construction and Experimental Process

The torsion oscillator shown in Fig. 4.5 was constructed of a $D = 25$ [μm] diameter, $L_f = 240$ [mm] long tungsten filament (Alfa Aesar 10405-H4), and a $2R = 220$ [mm], $D' = 1$ [mm] diameter twist-hardened copper torsion arm. This system was attached to a grounded aluminum support frame.

The diffraction grating and a balancing mass were attached to the two ends of the torsion arm. A small lightweight mirror was attached at the vertex of the torsion arm and filament to allow measurements of the angular displacement, $2\delta \approx S/L$, of a low power (less than 5 [mW]) HeNe tracking laser, where S is the linear displacement of the laser beam from its equilibrium position on a screen placed a distance $L = 1.92$ [m] from the pivot.

Time-lapse photographs (Canon 5D-III and Canon TC-80N3) of the screen were recorded at $\Delta t = 4$ [s] intervals. The position of the tracking beam was obtained by determining its centroid in each image.

The apparatus was placed on stand supported by a concrete-on-grade suburban basement floor that was remarkably free of vibrations and loading sag.

A grounded aluminum wire mesh was shaped into a 300 [mm] high cylinder to serve as a Faraday cage, shielding the oscillator from inadvertent electrostatic torques. The system was centered within a customized borosilicate bell jar of good optical quality. After evacuating air from within the bell jar to a pressure of 10^{-5} [hPa] (7.5×10^{-6} [Torr]), the disturbed oscillator was brought to near rest by means of radiation pressure from the forcing laser. At this pressure the mean free path of the remaining air molecules

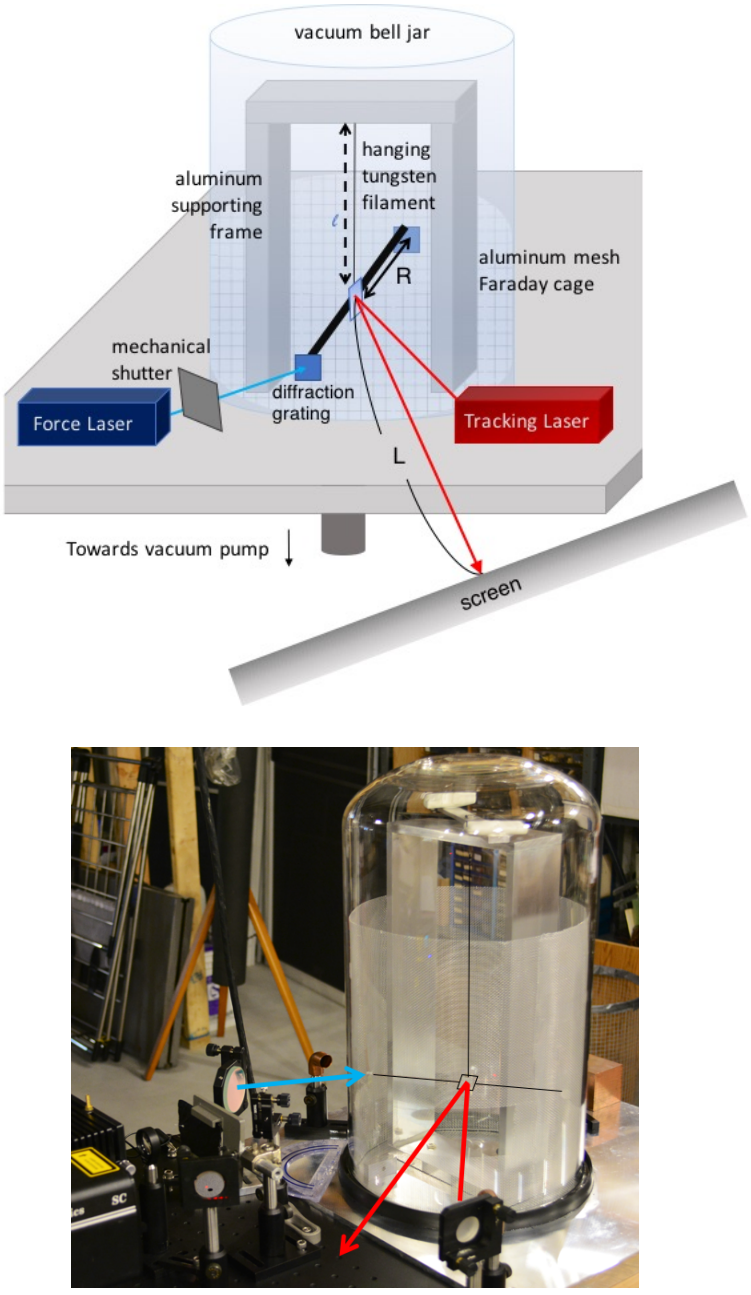

Figure 4.1: Schematic (top) and photo (bottom) of the torsion pendulum in a vacuum bell-jar, and the Faraday Cage covering the torsion pendulum.

exceeded the diameter of the bell jar. The system remained at rest for many hours – even while the vacuum system labored and people walked nearby.

4.1.2 Step Response

Based on the calculated moment of inertia, $I = 1.0 \times 10^{-5}$ [kg·m^2], and the measured period, the torsional spring constant of the filament was determined to be $\kappa = (2\pi/T_0)^2 I = 3.9 \times 10^{-8}$ [N·m/rad]. This value agreed well with the theoretical value obtained from a tabulated value of the Young's modulus $Y = 410$ [kN·mm^{-2}] [157]: $\kappa' = \pi Y D^4/32L_f = 6.6 \times 10^{-8}$ [N·m/rad]. The discrepancy between the two values is attributed to the actual value of Y which depends on the working history of the filament, and to the unknown variability of D along the length of the filament. We note that the radiation pressure force was not expected to induce significant linear pendular displacements of the total suspended mass $M = 2.4$ [g]. (In the worst case scenario with 5 [nN] applied to the deflection mirror rather than the grating, a linear pendulum would swing by only $FL_f/Mg \sim 50$ [nm].)

The equation of motion for angular displacement is

$$Id^2\delta/dt^2 + \gamma d\delta/dt + \kappa\delta(t) = FRu(t - t_0) \tag{4.1}$$

where $\gamma = 2I\alpha$ is a damping constant, $u(t - t_0)$ is a step function, and t_0 is the shutter release time. For small angular displacements, we assume the driving force, F is a constant. The solution of Eq. 4.1 is found via Laplace transform techniques: $\delta(t) = \delta_1(t) + \delta_2(t)\ u(t -$

t_0) where

$$\delta_1(t) = \mathrm{e}^{-\alpha\, t}\, \delta_0\, \cos(\omega_1 t + \phi_0) + \frac{\mathrm{e}^{-\alpha t}}{\omega_1}\left(\frac{\alpha}{2}\, \delta_0 + \delta_0'\right) \tag{4.2a}$$

$$\delta_2(t) = \frac{\mathrm{F}\, R}{\kappa}\left(1 - \mathrm{e}^{-\alpha\,(t-t_0)}\, \cos(\omega_1(t-t_0) + \phi_0)\right) \tag{4.2b}$$

and where $\delta_1(t)$ is the unforced solution of Eq. 4.1 for $t < t_0$, $\delta_0 = \delta(t=0)$, $\delta_0' = d\delta/dt\,|_{t=0}$, $\omega_0 = \sqrt{\kappa/I}$ is the natural oscillation frequency, $\omega_1 = \sqrt{\omega_0^2 - \alpha^2} = 2\pi/T_0 \approx \omega_0$ is the oscillation frequency, $T_0 = 100.6$ [s] is the measured oscillation period, $\alpha = 1/(80\ T_0)$ is the measured decay constant, and ϕ_0 is the initial phase at $t = 0$. Values of the unknown parameters are found by fitting δ_1 and δ_2 to the measured angular displacement data.

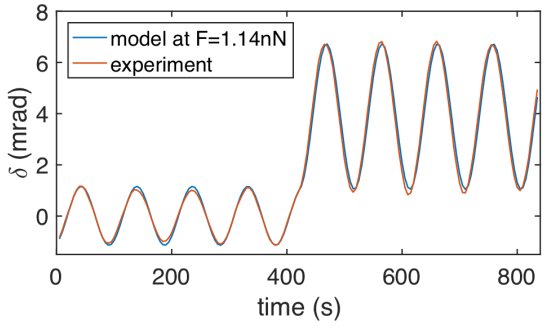

Figure 4.2: Example of measured and modeled pendulum angular displacement, as a step response to t: λ=808 nm, Λ = 540nm, P_0 = 345 mW, θ_i = 40°. Fitted parameters: shutter release time $t_0 = 420$ s, parallel force component magnitude $|F_p| = 1.14$ nN.

4.1.3 Uncertainty

A torsion pendulum is used in the fields of electrical science, biophysics, and gravitational science for precision measurement [55]. From the broad variations of measurements, the closest comparable and well-documented case will be torsion pendulum used

for the gravitational constant G constant measurement, as the reported uncertainty is down to the scale of 1×10^{-15} $\mathrm{m^3kg^{-1}s^{-2}}$. In the step response measurements, the angular displacement amplitude introduced by the laser radiation force is derived as $\delta_2(t_0) = FR/\kappa$, which helps us translate the pendulum angular displacement uncertainty and the torsion spring constant uncertainty into the uncertainty of the measured force $\Delta F/F = \sqrt{(\Delta\delta/\delta)^2 + (\Delta\kappa/\kappa)^2 + (\Delta R/R)^2}$.

Noise Spectrum of the Pendulum

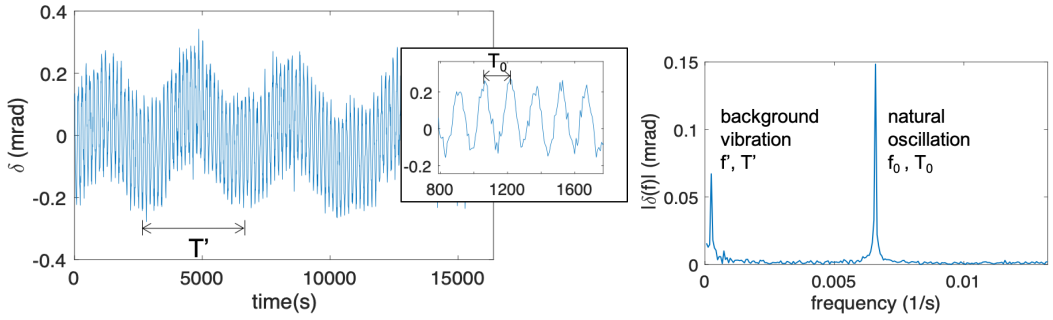

Figure 4.3: Left: Pendulum oscillation noise. Right: Noise spectrum indicates a white noise, containing the natural frequency and another environmental low-frequency noise.

The pendulum oscillation noise measurement is taken after letting the pendulum sit quietly under vacuum, untouched for 7 days (Fig. 4.3). The noise spectrum indicates a white noise distribution of the setup, containing both the natural frequency (f_0=0.006589 [Hz], T_0= 151.8 [s]) and another environmental low-frequency component (f'=0.000244 [Hz], T'=4098 [s]) , possibly caused by the compressed air circulation system that is running in the background introducing subtle and low-frequency vibration. The power spectral density of the noise will be an estimation of the average noise level, which is evaluated to be 0.016 [mrad]. [154].

Pendulum Torsion Constant The torsion tungsten filament used in our experiment (GoodFellow P/N W 005130) is $D = 25$ [μm] in diameter and $L_f = 240$ [mm] long. Unlike most filament that are either annealed or hard drawn, it is a stress relieved filament, where the stress relief temperature is below the annealing temperature.

The anelastcity of a tungsten fiber may cause the torsion constant to be frequency dependent, and attribute to a source of error. The error propagation from the frequency to torsion constant using can be $\Delta\kappa/\kappa = \sqrt{2(\Delta\omega/\omega)^2)}$, based on the relation: $\kappa = I\omega^2$. Other error sources for the torsion constant includes thermoelasticity and nonlinearity of the filament, but are analyzed to be less dominant [89].

Laser Heating and Reradiated Power Assuming tabulated values for fused silica, e.g., $C_p = 750$ [J/kg-m] (specific heat) and $\rho = 2 \times 10^3$ [kg/m^3] (density), a beam of power $P = 1$ [W] and waist $w_0 = 5$ [mm], and a worst case value of the absorption coefficient in the near ultraviolet range,$\alpha_0 = 10^{-2}$ [m^{-1}] [150], the rate of heating is given by $d\tilde{T}/dt = I\alpha_0/\rho C_p$, where $I = 2P/\pi w_0^2$ for a Gaussian beam. We therefore calculate a worse case temperature rise of less than $\Delta\tilde{T} = 0.02$ [K] over a single oscillation period of 100.6 [s]. The re-radiated power owing to this temperature excess is found from the Stefan-Boltzmann law: $\Delta P = \sigma((\tilde{T} + \Delta\tilde{T})^4 - \tilde{T}^4)\pi w_0^2$, where $\sigma = 5.67 \times 10^{-8}$ [J·s·K^4/m^2] and $\tilde{T} = 300$ [K]. The re-radiated power, $\Delta P = 4.8 \times 10^{-4}$ [W] is significantly less that the incident power of 1 [W]. Laser heating may therefore be ignored in our experiment.

Uncertainty component	Uncertainty
Background Vibration	$\Delta\delta = 0.016$ [mrad]
Torsion arm length	$\Delta R/R = 4.5 \times 10^{-3}$
Pendulum Spring constant	$\Delta\kappa/\kappa = 1.2 \times 10^{-4}$
Laser heating and re-radiated power (fused silica)	$\Delta F_h/F = 4.8 \times 10^{-4}$

Table 4.1: Major components for uncertainty for the torsion pendulum measurement are listed, assuming the incidence laser power is 1[W]. The uncertainties are listed as 1σ uncertainties.

4.2 Measurement Results

Let us first consider our interest in an ideal single-order diffraction grating—-having unity transfer efficiency into a single diffraction order, allowing only an incident wave and either a transmitted or reflected wave. The parallel and normal force components of radiation pressure force may be expressed by the use of Eq.s 2.10 and , respectively:

$$F_p = -(P_i/c)(m\lambda/\Lambda) \tag{4.3a}$$

$$F_n = (P_i/c)(\cos\theta_i \pm (1 - (m\lambda/\Lambda - \sin\theta_i)^2)^{1/2}) \tag{4.3b}$$

where the minus (plus) sign is for a transmissive (reflective) diffraction order, and $\lambda/\Lambda = K/k_i$ is the ratio of the grating momentum and photon momentum.

The parallel force $\vec{F_p}$ and $m\vec{K}$ are antiparallel as expected from conservation of momentum (e.g., see Fig. 1) That is, the value of $\vec{F_p}$ is directly related to the grating momentum $\vec{K}$. What is more, F_p is independent of the incident angle θ_i (assuming of course that the diffraction condition $|\theta_i| > |\theta_{i,c}|$ is satisfied). The normal component of force is positive below the Littrow diffraction angle, defined by the relation $2\sin\theta_{i,L} = m\lambda/\Lambda$. For $|\theta_i| > |\theta_{i,L}|$ the normal component of force is negative and the light source acts as a par-

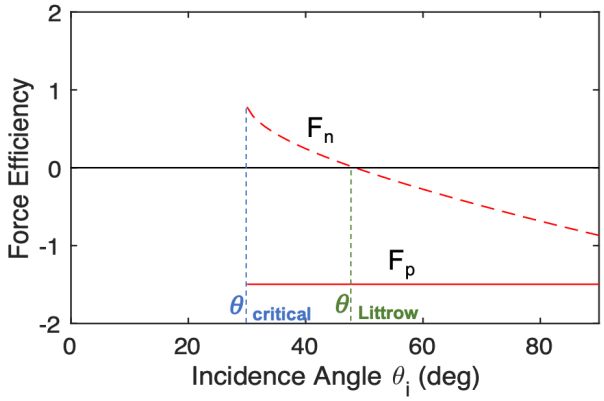

Figure 4.4: Force efficiency curve, described in Eq. 4.3b (P_i/c=1), for an example grating where λ = 808m, Λ=540nm, $\theta_{i,c}$= 30° and θ_L=54°

tial "tractor beam" [114, 119, 143, 144]. The force efficiency curve, defined by assuming $P_i/c = 1$ in Eq. 4.3b, for an example grating where λ = 808m, Λ=540nm, is plotted in 4.4, where $\theta_{i,c}$= 30° and θ_L=54°.

In practice, a grating may diffract multiple orders and also the diffraction efficiency of each may vary with the incident angle and wavelength. In such cases, the expression of force must account for the momentum imparted by each grating order, which may be reflective or transmissive in nature (as indicated by r and t subscripts below). If there is a dominant diffracted order, one may expect the force on the grating to be similar to the predictions described above. In general the force components for a non-absorbing grating may be expressed

$$F_p = -\frac{P_i}{c}\sum_m \left[(\eta_{m,r} + \eta_{m,t})\,(m\lambda/\Lambda)\right] \tag{4.4a}$$

$$F_n = \frac{P_i}{c}\sum_m \Big[\eta_{m,r}(\cos\theta_i + (1-(m\lambda/\Lambda - \sin\theta_i)^2)^{1/2}) + \eta_{m,t}(\cos\theta_i - (1-(m\lambda/\Lambda - \sin\theta_i)^2)^{1/2})\Big] \tag{4.4b}$$

where $\eta_{m,r} = P_{m,r}/P_i$ and $\eta_{m,t} = P_{m,t}/P_i$ are the efficiencies of the m^{th} order diffracted beams at the wavelength λ, and $\sum_m(\eta_{m,r}+\eta_{m,t}) = 1$ owing to the conservation of energy.

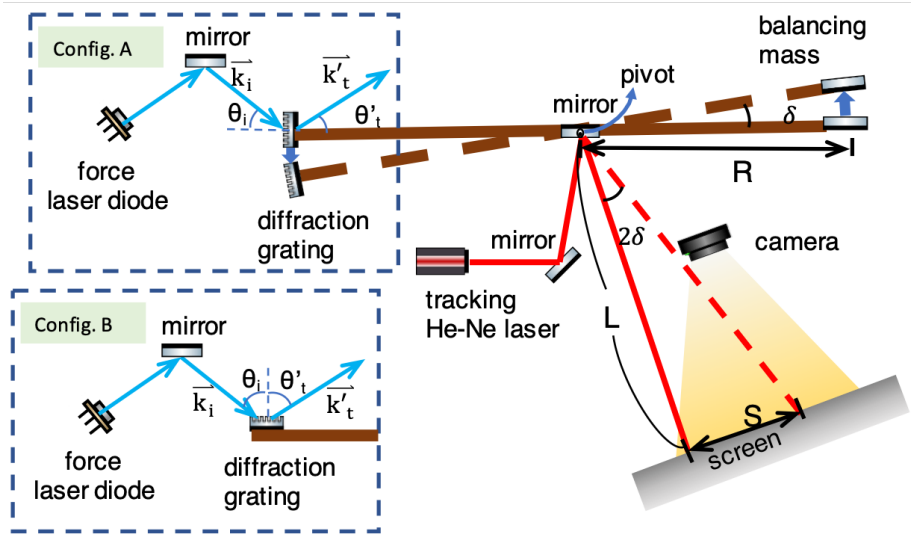

Figure 4.5: Top view schematic of torsion oscillator with moment arm of length R, angular displacement δ, forcing laser, tracking laser, camera, screen, and diffraction grating in Configuration A or B.

We selected a commercially available single order fused silica transmission grating (LightSmyth T-1850-800s-3210-93) having a period $\Lambda = 540$ nm. The diffraction grating

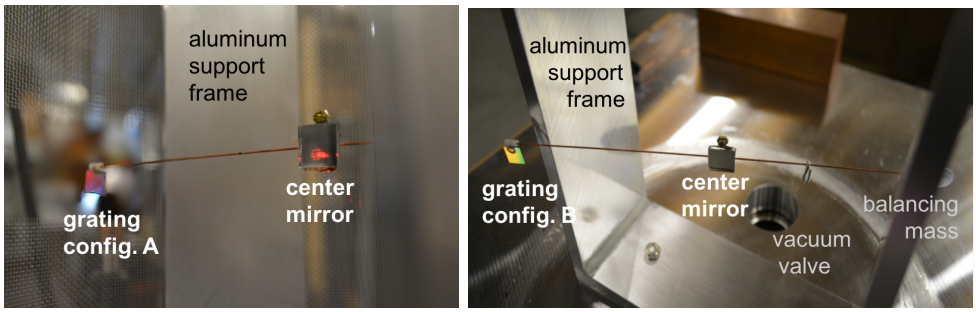

Figure 4.6: Left: Photo taken without the bell jar for Configuration A; Right: Configuration B, both corresponding to the schematic.

was ground to a thickness of 190 μm to minimize the moment of inertia (i.e., achieve larger angular displacements). The grating was attached to the torsion arm in one of two configurations: (A) with its surface normal parallel to the copper wire; (B) with its surface normal perpendicular to the copper wire (see insets of Fig. 4.5, and photos of setup in Fig. 4.4). A metallic balancing mass was placed on the other end of the copper torsion arm. For comparison and greater validation, we made use of two forcing lasers. The first laser ($\lambda = 808$ nm, $P_0 = 345$ mW) provided an efficient first order diffraction at the Littrow angle. The second laser ($\lambda = 447$ nm, $P_0 = 1.5$ W) allowed both a first order and second order Littrow angle. Weaker diffraction orders were also detected in both cases. The measured period of free oscillation of the torsion oscillator was $T_0 = 100.6$ s, and the characteristic decay time ($1/\alpha$) was roughly 80 T_0. Although the output power of the laser was constant, the power on the grating varied with incident angle owing to varied Fresnel transmission at the borosilicate bell jar surfaces. To account for this variability we calculated the transmission through the bell jar, $T_A(\theta_i)$ and $T_B(\theta_i)$, for both configurations (see Table 4.2) and determined the expected power at the grating, e.g., $P_i(\theta_i) = T(\theta_i)P_0$.

The diffraction grating was first mounted with its surface normal oriented parallel to

λ=808nm, n=1.51	θ_i	30°	40°	50°	60°		
Config. A	T_A	0.89	0.87	0.83	0.78		
Config. B	T_B	0.78	0.83	0.87	0.89		
Scatter	η_s	0.17	0.19	0.13	0.23		
λ=447nm, n=1.53	θ_i	15°	25°	35°	45°	55°	65°
Config. A	T_A	0.9	0.9	0.88	0.85	0.8	0.74
Scatter	η_s	0.21	0.33	0.36	0.23	0.29	0.27

Table 4.2: Calculated Fresnel transmission coefficients $T(\theta_i)$ for borosilicate bell jar, and deduced grating scattering fraction η_s=P_s/P_0.

the torsion arm, as depicted in Fig. 4.5, Config. A. The grating lines were transverse to the plane of incidence. With the bell jar removed, the oscillator was immobilized to allow measurements of the transmitted, diffracted, and reflected beams with the forcing laser ($\lambda = 808$ nm, and linear polarization transverse to the plane of incidence). The measured diffraction efficiencies and angles are depicted in Fig. 4.7(a) for four different angles of incidence between 30° and 60° (the incident wave vectors are shown without arrows). For this range, $\theta_i > \theta_{i,c}$ and the incident beam under-filled the grating surface. The corresponding force components (described below) are shown in Fig. 4.7(b) as round black data points. The transmitted first order diffraction efficiency was expected to be optimal near the Littrow angle $\theta_i = 48°$. In fact both the 40° and 50° incident angles provided measured peak diffraction efficiencies of roughly 60%. The total measured diffracted power amounted to $\sim 82\%$ of the input beam power, suggesting that $\sim 18\%$ of the beam power was diffusely scattered (listed as $\eta_s = P_s/P_0$ in Table 4.2). The scattering is attributed to power that does not diffract into allowed orders, but rather directly scatters or couples into guided waves and subsequently scatters [24, 25, 35, 77, 155].

Next we enclosed the oscillator within the bell jar, evacuated the chamber, and brought

the free oscillator to a near standstill. The forcing laser power was set to $P_0 = 345$ mW and a mechanical shutter was opened at time t_0 to provide a step function force on the grating, resulting in an angular displacement such as that depicted in Fig. 4.2.

This procedure was repeated three times for each of the four incidence angles described above. The time-varying angular displacement of the tracking laser upon the screen was extracted and fitted to the solution (Eq. 4.2) of well-known equation for a weakly damped harmonic oscillator (Eq. 4.1) from which we derived force values for F_p. The excellent agreement between the experimental data and the oscillator model in Fig. 4.2 (typical RMS angular displacement error $\sim 0.08\%$) confirms both the veracity of the harmonic oscillator model and the high degree of mechanical stability and repeatability of our apparatus.

The determined values of the tangential force F_p are plotted in Fig. 4.7(b), showing good agreement between the values of force that were measured with the torsion oscillator (dark circles with error bars) and the values predicted from the measured diffraction efficiencies using Eq. 4.4(a) (white circles).

To obtain values of the normal component of force we changed the orientation of the diffraction grating to Config. B (see Fig. 4.5) and recorded the laser-driven angular displacement of the torsion pendulum. The procedure described above was used to extract values of F_n, shown in Fig. 4.7 as dark squares with error bars. Again we find relatively good agreement with the values predicted from Eq.4.4 , shown as white squares in Fig. 4.7(b). As suggested above, the normal component of force is found to vanish; but unlike the case of a single order grating where it vanishes at the Littrow angle, here we find $F_n = 0$ at $\theta_i \sim 60^\circ$. Discrepancies between the measured values of force and the values predicted from efficiency measurements may be attributed to non-uniform scattering of

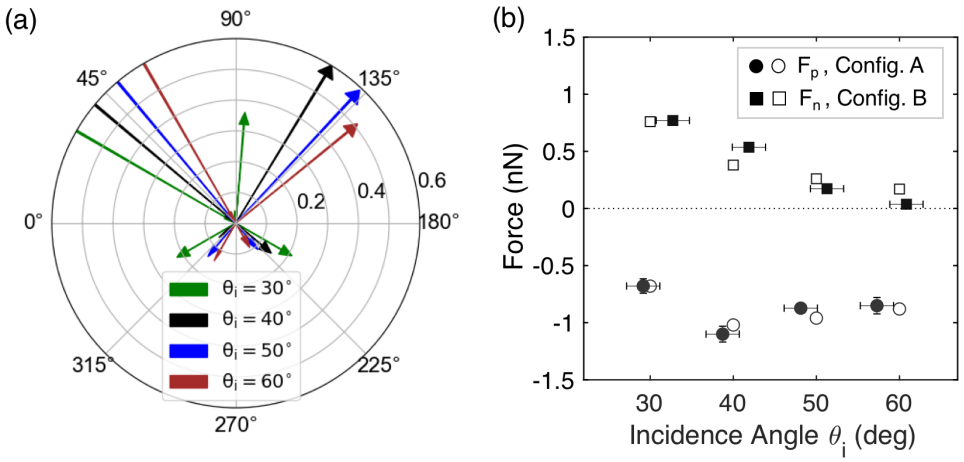

Figure 4.7: Measured (a) diffraction efficiencies and angles, and (b) force components, F_p and F_n, for $\lambda = 808$ nm, $P_0 = 345$ mW, and four angles of incidence. (a) The grating surface (not shown) is aligned along the 90° - 270° line. (b) Torsion oscillator measurements (dark). Predicted values based on efficiency measurements (white).

the guided waves, which also assert radiation pressure.

To assess the radiation pressure at a wavelength that supports two Littrow angles, one at $\theta_i = 24°$ for $m = 1$and another at 56° for $m = 2$, we substituted a laser having a wavelength $\lambda = 447$ nm and power $P_0 = 1.5$ W. If a single dominant diffraction order is produced at a given angle of incidence, we expect the value of F_p to scale with the value of m according to Eq. 4.3b(a). To verify this prediction, we mounted the grating in Config. A (see Fig. 4.5). The measured diffraction efficiencies of the transmitted and reflected beams are depicted in Fig. 4.8(a) for angles where there is a dominant first order beam, and in Fig. 4.8(b) for angles where there is a dominant second order beam (the incident wave vectors are shown without arrows). Values of force based on these efficiency values and Eq. 4.4(a) are depicted as white circles in Fig. 4.8(c), whereas those obtained from the torsion oscillator are shown as black circles. Accounting for the angle-dependent

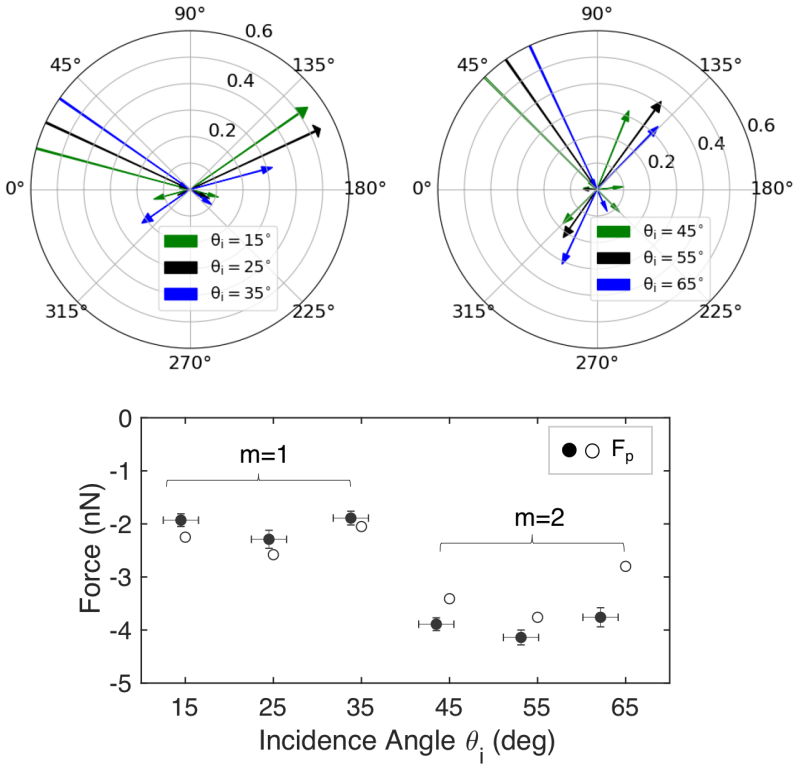

Figure 4.8: Diffraction efficiencies and angles, and radiation pressure at $\lambda = 447$ nm, $P_0 = 1.5$ W. (a) $m = 1$ set: Measured efficiencies at incident angles θ_i near the first order Littrow angle 24°. (b) $m = 2$ set: Same as (a) but near the second order Littrow angle 56°. (c) Measured (black circles) and predicted (white circles) values of F_p.

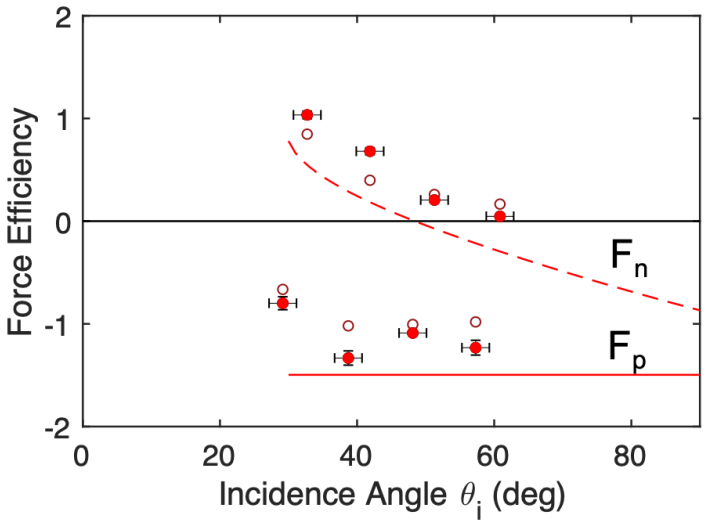

Figure 4.9: The calculated force efficiency of an ideal single order diffraction grating, compared to the measured force efficiency on a single-order dominnat mult-order diffraction grating.

transmission through the bell jar for the torsion oscillator experiments (see Table 4.2), the average force efficiency, $F_p c/TP_0$, was 0.99 for the $m = 2$ set, and 0.46 for the $m = 1$ set, providing a ratio (2.15) that was 8% higher than the value (2.00) that would have been expected for grating producing a single diffraction order (one near $\theta_i = 24°$ and the other near 56°). This agreement with the single order approximation is remarkably good, supporting the direct relationship between the grating order m and F_p. Discrepancies were found between the measured forces and those predicted from the multi-order model (black and white circles in Fig. 4.8(c), respectively). The differences, which are more pronounced than the 808 nm data, may be attributed to the wavelength dependent scattering and wave guiding. Scattering generally increases as the wavelength decreases. In fact the scattered powers listed in Table 4.2 are greater at $\lambda = 447$ nm than it is at 808 nm.

In summary we have used a vacuum torsion oscillator in two configurations at $\lambda = 808$ nm to measure the radiation pressure force both normal and parallel to a diffraction grating of period $\Lambda = 540$ nm. The grating produced a dominant transmitted diffraction order and a weaker transmitted and reflected order. The measured forces were qualitatively similar to those predicted for a grating producing a single diffractive order, and quantitatively in agreement with a multi-order model. The parallel component of force was relatively constant as the angle of incidence varied, whereas the normal component varied with angle, vanishing near the Littrow angle. An additional experiment at a shorter wavelength ($\lambda = 447$ nm) verified that the parallel component of radiation pressure force scales with the diffraction order, as expected when a single dominate order is diffracted. Experiments at both wavelengths confirmed that when there is a dominant diffraction order, the parallel component of force scales as the ratio of the optical wavelength and the grating period, λ/Λ – or equivalently, with the ratio of the grating momentum and wave momentum, K/k_i. That is, the so-called grating momentum, which is a construct from Fourier optics, has been verified to impart an equal and opposite mechanical momentum. Unlike a reflective surface that has only a normal component of radiation pressure force, a grating has been experimentally demonstrated to provide both normal and tangential components, thereby affording new optomechanical applications of diffractive materials.

Chapter 5

Radiation pressure on Diffractive Beam-Riders

5.1 Diffractive Beam-Riders

An optical beam rider making use of a light sail comprised of two opposing diffraction gratings is experimentally demonstrated for the first time. We verify that the illuminated space-variant grating structure provides an optical restoring force, exhibiting stable oscillations when the bi-grating is displaced from equilibrium. We further demonstrate parametric cooling by illuminating the sail with synchronized light pulses. This experiment enhances the technical feasibility of a laser-driven light sail based on diffractive radiation pressure.

5.2 A bi-grating beam-rider

A space variant grating such as a "bi-grating" [141], and variants thereof [62] may provide a position-dependent force. Thus a space variant grating may be designed to function as a "beam-rider". A laser-driven beam rider must produce self-action to both pull the sail into the beam path when disturbed and to inhibit tumbling [68, 92, 125, 159, 165].

Here we report a fundamental experiment that verifies the predicted opto-mechanical stability provided by a diffractive light sail. We demonstrate that a bi-grating comprised of two adjacent grating panels having equal and opposite grating vectors provides a position-dependent restoring force. Furthermore we prove that the system may be used as a parametric oscillator, allowing forced damping [21,36,54,163], excitation [23,28] or control [27, 162] by use of a time-varying laser beam. The latter opens new opportunities for both space and terrestrial applications such as energy harvesting, opto-mechanical cooling (described below), and photonic sensing [130, 132]. The bi-grating model in this report, which is constrained to one degree of freedom, may be generalized to a fully space-variant structure having three degrees of freedom, which is beyond the scope of this section for a bi-grating beam-rider.

5.2.1 Structure

The opto-mechanics of a bi-grating diffractive beam rider may be understood by examining Fig. 5.1(a,b) which depicts two diffractive panels (A and B), each of width L. Ideally each panel diffracts the incident beam of half-width w_0 into a single diffraction order, as depicted, resulting in positive (negative) components of radiation pressure force, F_x on Panel A (B). A stable equilibrium point is expected at $x = 0$, i.e., when the beam equally

illuminates both panels. Both panels experience the same longitudinal component of force F_z (not shown), which does not affect our experiment and is therefore ignored below [33].

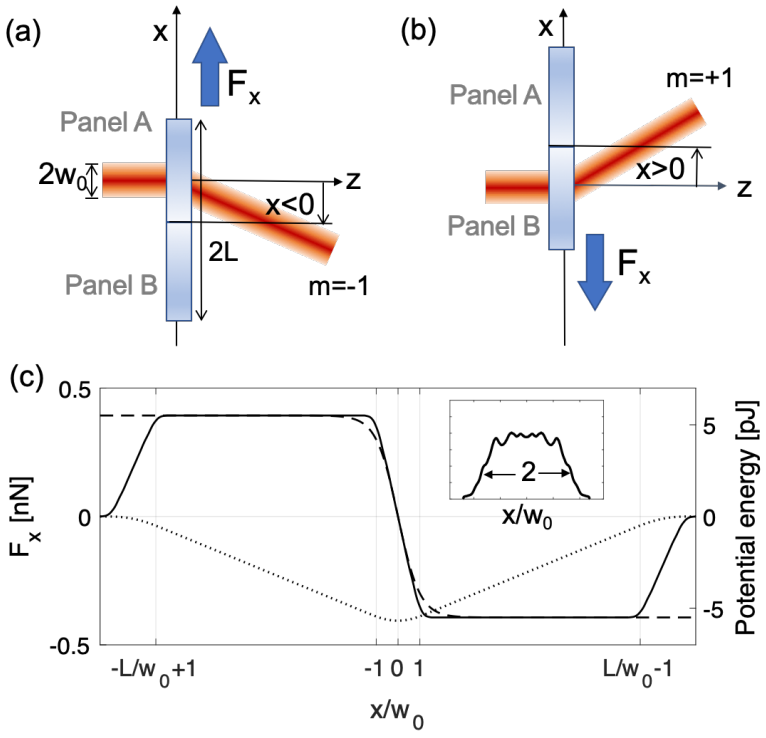

Figure 5.1: Transverse restoring force vs. displacement of the bigrating. Laser of radial size w_0 illuminating (a) Panel A ($x < 0$) and (b) Panel B ($x > 0$). (c) Position-dependent force profile calculated from Eq. 1 (solid) and "tanh" model (dashed). Potential energy landscape (dotted). Inset: Integrated beam profile of measured beam $\int g(x, y)dy$.

The position-dependent force profile on a given panel is related to the overlap integral of the measured beam intensity profile $I(x, y) = P_i g(x, y)$ across the respective panel, where P_i is the incident beam power and $g(x, y)$ is the normalized profile function: $\int g(x, y)dxdy = 1$. Assuming the beam-width is smaller than the panel size, $w_0 < L$, and

the beam is centered on the panels in the y-direction, the net force may be expressed:

$$F_x(x) = F_{x,A} + F_{x,B} \tag{5.1a}$$

$$F_{x,A} = F_0 \int_{-L}^{L} \int_{-L}^{0} g(x - x'; y) dx' dy \tag{5.1b}$$

$$F_{x,B} = -F_0 \int_{-L}^{L} \int_{0}^{L} g(x - x'; y) dx' dy \tag{5.1c}$$

$$F_0 = \eta \lambda P_i / \Lambda c \tag{5.1d}$$

where F_0 is a scaling force [146], c is the speed of light, and $\eta = \sum_{\mathrm{m}} \eta_{\mathrm{m}} \mathrm{m}$ is the diffractive force efficiency, where $\eta_{\mathrm{m}} = P_{\mathrm{m}}/P_i$ and P_{m} is the power diffracted into the m^{th} order (see Table 5.1). The force near the equilibrium point at $x = 0$ may be approximated

$$\tilde{F}_x(x) \approx -F_0 \tanh(x/\mathrm{w}_0) \tag{5.2}$$

as illustrated by the dashed line in Fig. 5.1(c). For the measurements described below, η=0.73, λ= 808 [nm] is the forcing laser wavelength, and Λ=6 [μm] is the grating period. For example, the position-dependent force depicted in Fig. 5.1(c) (solid) was determined for a beam of width w_0=2.1 [mm] and panels of widths L=12.7 [mm]. The potential energy associated with this force, plotted in Fig. 5.1(c) (dotted), indicates an equilibrium point at $x = 0$, as expected.

	η_{-2}	η_{-1}	η_0	η_1	η_2	$\eta_{r,0}$	η_s
panel A	0.006	0.773	0.015	0.051	0	0.107	0.048
panel B	0	0.051	0.015	0.773	0.006	0.107	0.048

Table 5.1: Experimentally determined fractional power for m^{th} order diffraction η_{m}, specular reflection $\eta_{r,0}$, and diffuse scattering η_s.

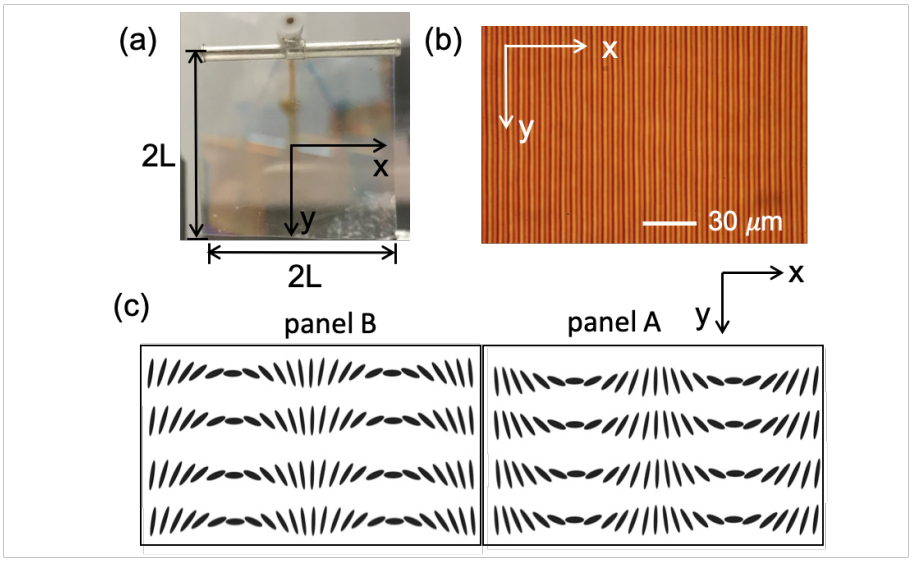

Figure 5.2: (a) Diffractive beam-rider mounted on the pendulum, under unpolarized white light. (b) A panel of the diffractive beam-rider under polarization microscope. (c) Director orientation in the cycloidal diffractive waveplates.

Near equilibrium the bi-grating experiences a restoring force with an approximate radiation pressure stiffness

$$K_{RP} = -dF_x/dx|_{x=0} \approx -d\tilde{F}_x/dx|_{x=0} = F_0/\mathrm{w}_0. \tag{5.3}$$

We find that the approximate stiffness value agrees with the experimentally determined value (described below) to within 4%: $K_{RP} = (1.9 \pm 0.2) \times 10^{-7}$ [N/m] for a beam of width $\mathrm{w}_0 = 2.1 \pm 0.05$ [mm].

We designed a micrometer thin space variant bi-grating comprised of nematic liquid crystals having its anisotropy axis -the director - rotated in the grating plane over a spatial period Λ (Fig. 5.2(a-b)). The cycloidal rotation directions are opposite in Panels A and

B (Fig. 5.2(c)), resulting in equal and opposite grating vectors [109] for a circularly polarized beam of light. The diffraction efficiency of such gratings theoretically reaches 100% for radiation wavelength meeting half-wave retardation condition. To provide structural support the layer was adhered to a 100μm thick polymer film. The net mass of the square 25.4×25.4 [mm^2] bi-grating was $M_g = 0.12$ [g]. Owing to the opposite handedness of the director rotation, a circularly polarized incident beam diffracts in opposite directions as depicted in Fig. 5.1(a,b). For a beam at normal incidence the dominant first order diffraction angles are given by $\theta_{\pm 1} = \pm sin^{-1}(\lambda/\Lambda) = \pm 7.74^{\circ}$. We get 91.5% of the unscattered, transmitted light into the ∓ 1 order for panels A and B.

To observe the reaction of the bi-grating to either a constant or a time-varying beam of light we attached it to one arm of a torsion oscillator at a vacuum pressure of 1.4×10^{-6} [Torr] $= 1.8 \times 10^{-4}$ [Pa], as depicted in Fig. 5.3 (the other half of the torsion arm which includes a balancing mass is not shown). The torsion arm of length $R = 0.11$ [m] was suspended by a 25 [μm] diameter tungsten filament of length 0.24 [m]. A small mirror was attached to the torsion arm at the pivot to provide a means of measuring the deflection angle 2ϕ of a low power tracking laser beam. Time lapsed photographs of the tracking beam were recorded on a screen at a distance D =1.75 [m]. A small angular displacement of the bi-grating, ϕ, produces a lateral displacement of the tracking beam S, which is also related to the linear displacement of the bi-grating, x: $\phi \approx S/2D \approx x/R$.

The torsional equation of motion of the mounted bi-grating subjected to a time-dependent force $F_x(t)$ may for convenience be expressed as a function of the displacement x rather than angle:

$$Jd^2x/dt^2 + 2(J/\tau)dx/dt + k_f x(t) = F_x(t)R^2 \tag{5.4}$$

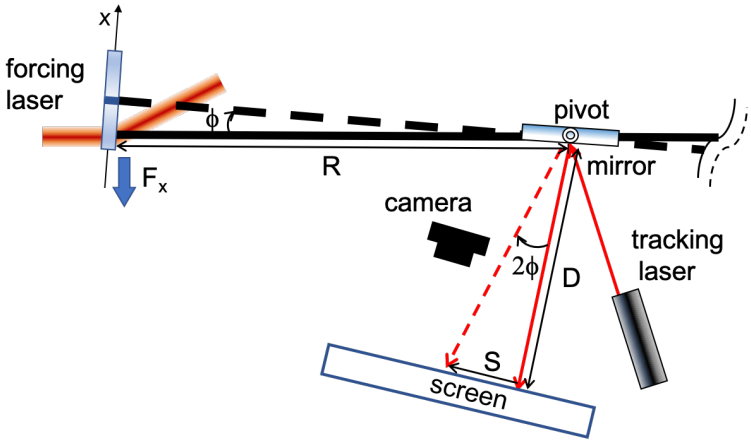

Figure 5.3: Partial top view of torsional pendulum with arm of length R that pivots from equilibrium owing to radiation pressure on a bi-grating from a forcing laser. Angular displacement ϕ is obtained from the recorded position on a screen of a tracking laser reflected from a mirror at the pivot.

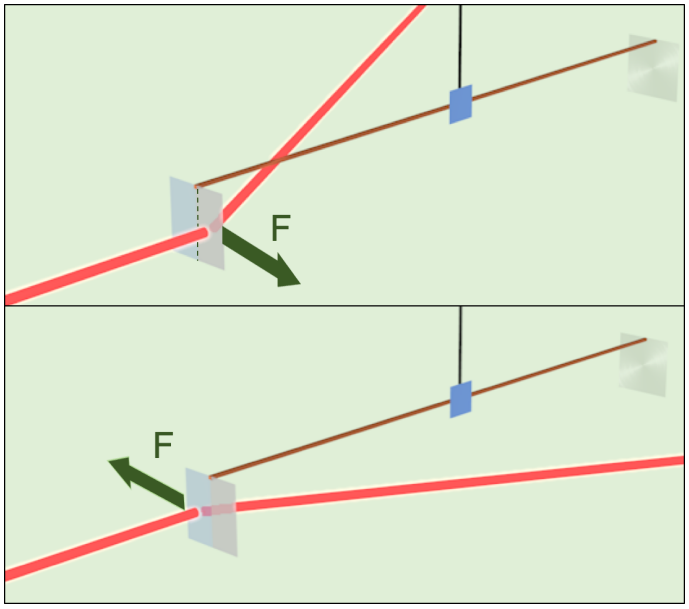

Figure 5.4: A 3-dimensional version of the experimental setup. The top half of this figure corresponds to Fig. 5.3, having the laser off-centered onto the right panel, and the beam-rider experiences a force pulling to the right, and vice versa.

where $J = (1.16 \pm 0.01) \times 10^{-5}$ [kg·m^2] is the calculated moment of inertia, $k_f = (2\pi/T_0)^2 J = (1.99 \pm 0.04) \times 10^{-8}$ [N·m/rad] is the torsional stiffness of the tungsten filament, $T_0 = 151.8 \pm 0.8$ [s] is the measured natural oscillation period when $F_x(t) = 0$, and $\tau = (568 \pm 5.5)\ T_0$ is the measured natural decay time.

The moment of inertia of the pendulum is determined by $J = M_b(2R)^2/12 + M_c(\mathrm{w}^2 + \mathrm{d}^2)/12 + M_r R^2 + M_1 R_1^2 + M_2 R_2^2 = (1.16 \pm 0.01) \times 10^{-5}$ [kg·m^2], where the torsion bar of mass $M_b = 0.38$ [g]; center pivot of mass $M_c = 1.05$ [g], width $w_c = 5$ [mm] and thickness d_c=1 [mm]; beam-rider with mounting tabs of mass M_r= 0.45 [g]; and two balancing masses on the balancing torsion arm (not shown in Fig. 3) of mass $M_1 = 0.37$ [g] at distance $R_2 = 0.01$ [m] away from the pivot and mass $M_2 = 0.48$ [g] at distance $R_2 = 0.098$ [m] away from the pivot, respectively. The total mass of the hanging components on the pendulum is 2.73 [g].

5.2.2 Step Response

To verify the existence of a light-induced restoring force we measured the step function response of the torsion oscillator, bringing the beam power from zero at $t < 0$ to a value of $P_i = 1.2$ [W] ($F_0 = 0.39 \pm 0.03$ [nN]) at $t > 0$, so that $F_x(t) = \tilde{F_x(x)}\ u(t)$ where $\tilde{F_x(x)}$ may be approximated by Eq. 5.2 and $u(t)$ is a step function. The instant $t = 0$ corresponds to the state where the excited oscillator passes through equilibrium, $x(t = 0) = 0$. In the linear regime where $|x/\mathrm{w}_0| << 1$, radiation pressure may be understood as an additional source of torsional stiffness: $k_{RP} = K_{RP} R^2 = (2.3 \pm 0.2) \times 10^{-9}$ [N·m/rad]. Thus we expect a corresponding frequency shift, $\Delta\omega = \omega' - \omega_0$, where $\omega_0 = \sqrt{k_f/J} = 2\pi/T_0 = (4.14 \pm 0.02) \times 10^{-2}$ was determined from a measurement of the free oscillation period T_0, and $\omega' = \sqrt{k'/J} = 2\pi/T'$, where $k' = k_f + k_{RP}$. We measured the period $T' = 141.8 \pm$

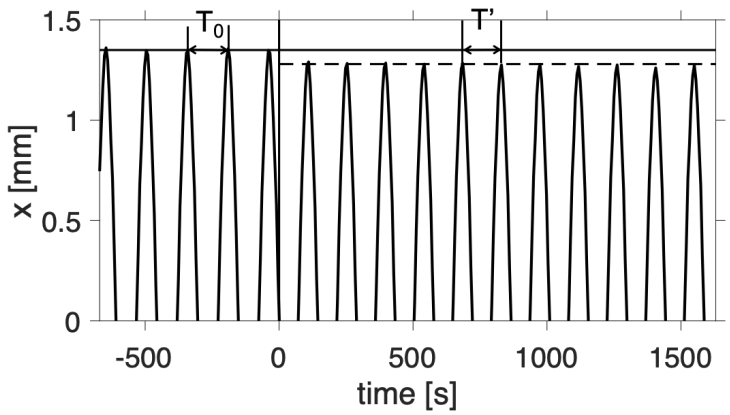

Figure 5.5: Pendulum step response to the light-induced restoring force, showing only the $(x > 0)$ parts the response. At $t = 0$, the oscillation $x = 0$, and the forcing laser turns on. As expected, the pendulum oscillated faster with a period T', with a smaller oscillating amplitude.

0.6 [s]. A comparison of these stiffness-based $(\omega'|_{k'}) = (4.37 \pm 0.34) \times 10^{-2}$[rad/sec] and period-based $(\omega'|_{T'}) = (4.43 \pm 0.02) \times 10^{-2}$[rad/sec] expressions of frequency are in good agreement.

As further evidence of a light-induced restoring force we compare the amplitude of oscillation before and after the optical step function described above. Instantaneous stiffening may be described as an energy conserving process [27]: $E_0 = (1/2)k_f\phi_{0,max}^2 = E' = (1/2)k'\phi_{max}'^2$, where $\phi_{0,max}$ and $\phi'_{max} = \phi_{0,max} - \Delta\phi$ are the respective oscillation amplitudes for $t < 0$ and $t > 0$. Assuming $\Delta\phi = \Delta x/R << 1$ we predict a decrease of the oscillation amplitudes:

$$\Delta\phi = \phi_{0,max}k_{RP}/2(k_f + k_{RP}) \tag{5.5a}$$

$$\Delta x = x_0K_{RP}/2(K_f + K_{RP}) \tag{5.5b}$$

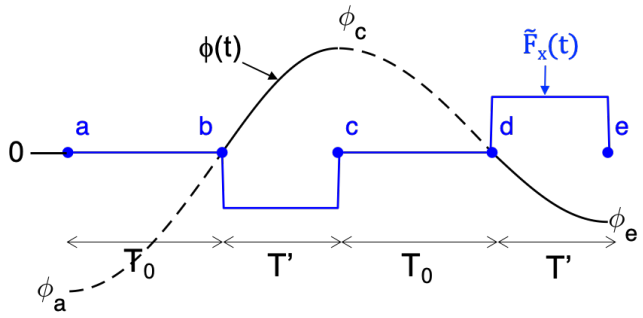

Figure 5.6: Radiation pressure force modulation $\tilde{F}_x(t)$ (blue, square) synchronized to the angular oscillation $\phi(t)$ (black, sinulsoidal) in a an oscillation cycle for parametric cooling. The oscillation is divided into 4 intervals by the points a,b,c,d,e, and the sinusoidal period alternates between T_0 and T' as it experiences zero and non-zero restoring force from the radiation pressure.

where $x_0 = R\phi_{0,max}$ is the oscillation amplitude for $t < 0$. Inserting foregoing stiffness values and the measured value $x_0 = 1.35$ [mm], we predict a value $\Delta x = 0.070 \pm 0.001$ [mm] (or 5.2% of x_0), which agrees with the measured value of $\Delta x_{meas} = 0.070 \pm 0.005$ [mm].

5.2.3 Parametric Cooling

As a final demonstration of the restoring force model of the bi-grating, we experimentally measured parametrically driven damping (or "cooling") by synchronizing laser illumination with the phase of the torsion oscillator. A square wave modulation of the laser power at twice the oscillator frequency was applied (see Fig. 5.6) at a beam power $P_i = 1.5$ [W] and beam size $w_0 = 3.1 \pm 0.05$ [mm] (i.e., $F_0 = 0.49 \pm 0.04$ [nN]). The light-induced torsional stiffness corresponds to $k_{RP} = (1.9 \pm 0.2) \times 10^{-9}$ [N·m/rad]. The forcing laser

was controlled to illuminate the beam-rider when the condition $x(t) \cdot v(t) > 0$ was satisfied:

$$\tilde{F}_x(t) = \begin{cases} \tilde{F}_x \text{ if } x(t) \cdot v(t) > 0 \\ 0 \quad \text{if } x(t) \cdot v(t) \leq 0. \end{cases} \tag{5.6}$$

where $v = \partial x / \partial t$. The modeled response (dotted line in Fig. 5.7) making use of Eq. 5.2 and the 4^{th} order Runge-Kutta numerical technique agrees with the measured displacement (solid line in Fig. 5.7), further validating our understanding of the system.

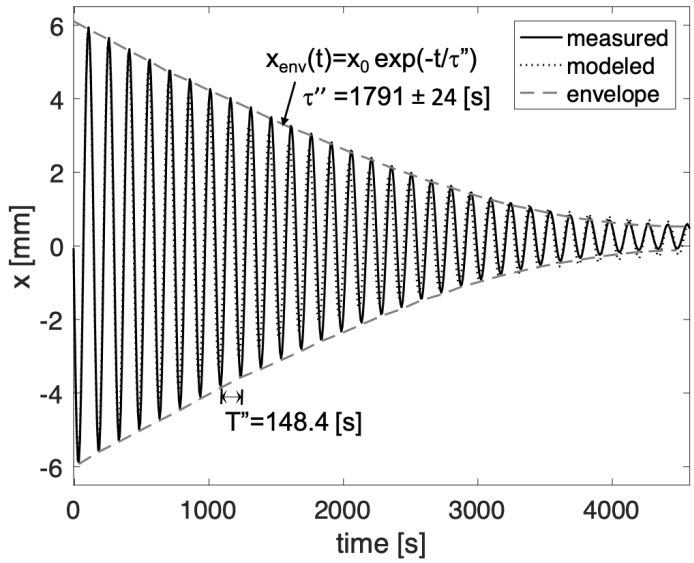

Figure 5.7: Parametric cooling of a bi-grating using square wave laser modulation at twice the oscillation frequency. Measured (solid line) and numerically modeled (dotted line) oscillations agree. The oscillation envelope (dashed line) shows exponential decay, with decay time τ". The average oscillation period T" agrees with the average of the unforced and forced period T_0 and T'.

The oscillation envelope of the parametrically driven bi-grating was found to exhibit

exponential decay (dashed line in Fig. 5.7):

$$x_{env}(t) = x_0 \exp(-t/\tau") \tag{5.7}$$

with a measured decay time $\tau" = 1791 \pm 24$ [s].

Again using energy arguments and a Hooke's law approximation, we predict the decay time for an arbitrary value of the scaling force, F_0 (or k_{RP}). Using the phased forcing protocol described by Eq. 5.7 and depicted in Fig. 5.6, we note the following sequence for one complete cycle, starting from an oscillation maximum, ϕ_a: (a-b) free oscillation for an interval $T_0/4$ with energy $E_{a,b} = (1/2)k_f\phi_a^2$; (b-c) stiffened oscillation for an interval $T'/4$, reaching an amplitude ϕ_c at point (c) and an energy $E_{b,c} = (1/2)(k_f + k_{RP})\phi_c^2 = E_{a,b}$; (c-d) free oscillation for an interval $T_0/4$ with energy $E_{c,d} = (1/2)k_f\phi_c^2$; (d-e) stiffened oscillation for an interval $T'/4$, reaching an amplitude ϕ_e at point (e) with energy $E_{d,e} = (1/2)(k_f + k_{RP})\phi_e^2 = E_{c,d}$. The period of the full cycle is given by $T" = (T_0 + T')/2$=148.4 [s]. The algebraic relation between ϕ_a and ϕ_e is readily found: $\phi_e = k_f\phi_a/(k_f + k_{RP})$. Setting $\phi_e = \phi_a \exp(-T"/\tau")$, we obtain the decay time

$$\tau" = T"/\ln(k_f/(k_f + k_{RP})) \tag{5.8}$$

which agrees well with our numerical model and experimental datum as shown in Fig. 5.8.

In summary we report experimental demonstrations of self-stabilizing attributes of a diffractive bi-grating beam rider. A radiation-pressure induced restoring force was predicted and experimentally observed by use of a vacuum torsion oscillator. Radiation pressure in effect stiffened the oscillator, resulting in a higher frequency and smaller amplitude of oscillation. What is more, we demonstrated parametric cooling by synchronizing the ra-

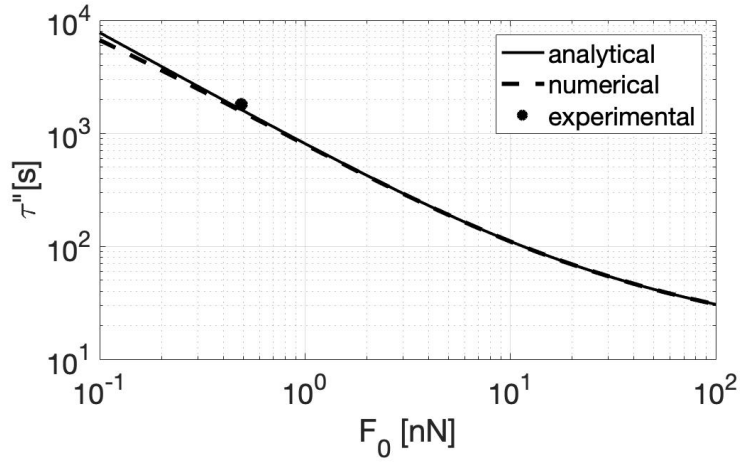

Figure 5.8: Parametric cooling decay time τ" as a function of the transverse radiation pressure force F_0.

diation pressure with the oscillator state. These results suggest an important technological step forward for the development of laser-driven sailcraft for in-space propulsion.

Our one-dimensional bi-grating may be generalized in future work to a radial grating or other space-variant designs to achieve three-dimensional opto-mechananical stability.

In general, self-stability may be achieved with either a reflective or transmissive grating structure, provided it diffracts light toward the center axis. Greater stability occurs for large diffraction angles, but at the expense of less longitudinal force along the axis of the incident beam. Owing to difficulties imposed by the small value of radiation pressure compared to the gravitational acceleration of the Earth, we propose demonstration missions either aboard the International Space Station or using CubeSat technology.

5.3 Axicon Beam-Rider

A light sail is a large optical film having a low mass-to-area ratio that harnesses photon momentum from a source such as the sun or a laser to provide in-space propulsion [40, 50, 65, 98, 145, 164]. The radiation pressure affords opportunities to achieve greater velocity changes compared to chemical rockets which are constrained by both the exhaust velocity and the relative mass of the rocket with and without propellant. In particular laser-driven sails may one day reach relativistic speeds, thereby enabling interstellar space travel [47, 51, 56, 78, 83, 95], allowing an opportunity for closeup views of our closest exoplanets around the host star Proxima Centauri [2, 16, 88, 121]. Mechanically stable propulsion free of tumbling and beam walk-off may be achieved by use of optical engineering whereby the sail is designed to have a net restoring force and torque. Such bodies include diffraction gratings and dielectric metasurfaces [34, 62, 64, 134, 139, 141, 142], and non-planar sails having spherical or conical shapes [18, 92, 125].

Experimental measurements of restoring force and dynamical motion of a laser-driven axicon diffraction grating are reported in this Letter, including demonstrations of both parametric amplification and parametric damping. A vacuum torsion oscillator with sub-nano-Newton sensitivity and a 1.5 [W] laser was used. The experimental results verify the principle that a diffractive sail such as an axicon can provide a transverse restoring force for beam-riding in space, as well as terrestrial applications such as solar energy harvesting, photonic sensing [17], and opto-mechanical damping, excitation, and control [91, 152].

We designed a diffractive axicon with radial period $\Lambda = 12.7$ [μm] and fabricated it using grayscale optical lithography in S1813 photopolymer [102]. A minimum feature width of 3 [μm], maximum feature height of 1.3 [μm] and 100 height-level discretization

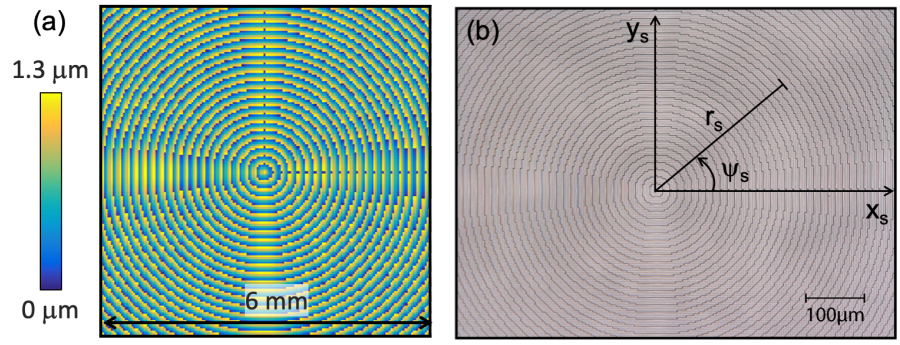

Figure 5.9: (a) Design profile of axicon grating (zoomed view of 18 [mm] $\times$ 18[mm] sample). (b) Optical micrograph of the fabricated axicon.

were used. The photopolymer was spun on a 100 [μm] thick sapphire support substrate at 1000 rpm for 60 [s], then baked in a convection oven at 110°C for 30 minutes. After exposure, it was developed in AZ developer 1:1 for 40 [s], rinsed with DI water and dried with N_2. An optically thin layer of Au-Pd was sputter-coated on the sample to provide a conductive ground, thereby mitigating spurious electro-static forces. For an incident beam with wavelength $\lambda = 808$ [nm], the diffraction cone angle is $\theta_d = -\sin^{-1}\lambda/\Lambda = -3.65°$, where the negative sign indicates diffraction toward the axicon axis. The grating momentum vector of the axicon having surface coordinates (x_s, y_s) may be expressed

$$\vec{K_s}(x_s, y_s) = -(2\pi/\Lambda)(\cos\psi_s\ \hat{x}_s + \sin\psi_s\ \hat{y}_s) \tag{5.9}$$

where ψ_s is the azimuth angle measured counter-clockwise from $\hat{x}_s$: $\cos\psi_s = x_s/r_s$, $\sin\psi_s = y_s/r_s$, and $r_s = (x_s^2 + y_s^2)^{1/2}$ as illustrated in Fig. 5.9.

A diode laser having a nearly uniform square irradiance profile of side 2w = 5.2 [mm] under-fills the square axicon grating of side $2L = 18$ [mm], producing arc or ring diffraction

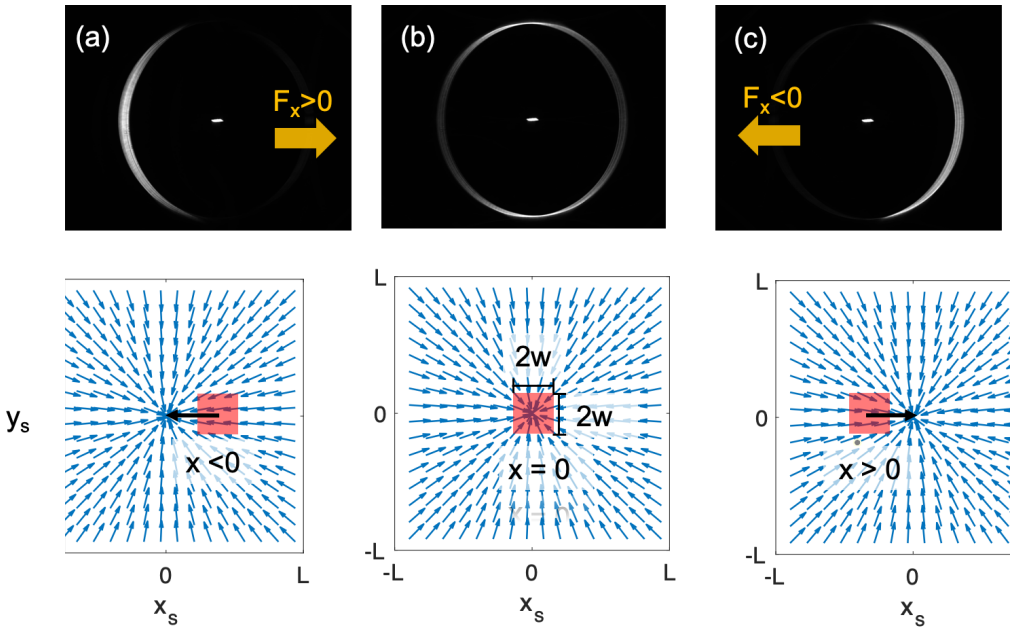

Figure 5.10: Top: Diffracted beam from axicon and transverse reaction force F_x for relative sail displacement with respect to a stationary beam: (a) $x < 0$, (b) $x = 0$, (c) $x > 0$, with corresponding black arrows (bottom). Bottom: Axicon of dimension $L = 9$[mm] and coordinates (x_s, y_s) with grating momentum vectors (blue arrows). Square laser beam (red) of dimension w = 2.6 [mm].

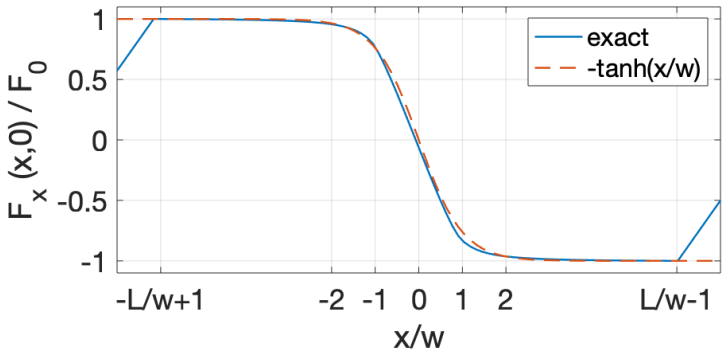

Figure 5.11: Force vs displacement of an axicon illuminated by a square beam with different beam half-widths w. Reported experiment: $w = 2.6$ [mm] and maximum displacement $x_{\max} = 4.5$ [mm]. Near equilibrium $F_x \approx -F_0 \tanh(x/w_2)$.

patterns as depicted in Fig. 5.10. For example a C-shaped arc is formed when the axicon is displaced a distance $x < 0$ from the optical axis of the laser beam, as shown in Fig. 5.10(a), in which case the transverse reaction force on the axicon, F_x, points in the positive $\hat{x}$ direction, resulting in a restoring force that draws the axicon back toward the beam axis.

If the entire incident beam is transmitted into the first order diffraction mode the radiation pressure force exerted by the square beam having its centroid displaced (x, y) relative to the axicon axis may be expressed as the overlap integral

$$\vec{F}(x,y) = \frac{\lambda P_i}{2\pi c} \iint_{-L}^{L} \vec{K}(x_s - x, y_s - y) g(x_s, y_s) dx_s \, dy_s \tag{5.10}$$

where $P_i = 1.5$ [W] is the incident beam power, c is the speed of light, and $g(x, y)$ is the normalized beam profile function with $\iint g(x,y)dxdy = 1$. As illustrated in Fig. 5.11 a uniform square beam of size $w = 2.6$ [mm] that under-fills an axicon constrained at $y = 0$

has a restoring force that may be approximated by

$$F_x(x,0) \approx -F_0 \tanh(x/\mathrm{w}) \tag{5.11}$$

where $F_0 = \eta\lambda P_i/\Lambda c = 1.8 \times 10^{-10}$ [N] is the theoretically expected magnitude of the radiation pressure force transverse to the grating surface normal, and where $\eta = (\eta_t - \eta_r)\eta_d$ is a net efficiency factor with $\eta_t = P_t/P_i = 0.65$, $\eta_r = P_r/P_i = 0.04$ and $\eta_d = 0.91$ the respective measured transmittance, reflectance and first order diffraction efficiencies, and P_t, P_r and $P_i = 1.5$ [W] are the respective transmitted, reflected, and incident beam powers. We observed that the transmitted and reflected beams respectively diffracted toward and away from the optical axis, and thus these two components produced opposing forces in our experiment, as represented by the factor $\eta_t - \eta_r$.

From Eq. 5.10, 5.11 and Fig. 5.11 we obtain a desired restoring force. Setting $F_x = -\tilde{k}_{rp}\ x$ near equilibrium, we obtain an expression for the radiation pressure induced stiffness $\tilde{k}_{rp} \approx F_0/w$, assuming the beam under-fills the sail ($w < L$). As illustrated in Fig. 5.11 the force vanishes near equilibrium when $w > 2L$. We note that the beam on a laser-propelled sail will vary in both size and shape owing to diffraction, and the general expression in Eq. 5.10 may be applied for an arbitrary space-variant grating vector distribution $\vec{K}(x_s, y_s)$, thereby providing opportunities to optimize the restoring force on the sail during the period when the beam under-fills the sail.

To measure sub-nano-Newton forces we constructed a torsion pendulum comprised of a $L_f = 0.24$ [m] tungsten filament of diameter 25 [μm] and placed it in a glass bell jar under a vacuum of 3×10^{-5} [Pa]. The perimeter of the axicon was surrounded with conducting foil that was electrically grounded via a twist-hardened 1 [mm] diameter copper torsion

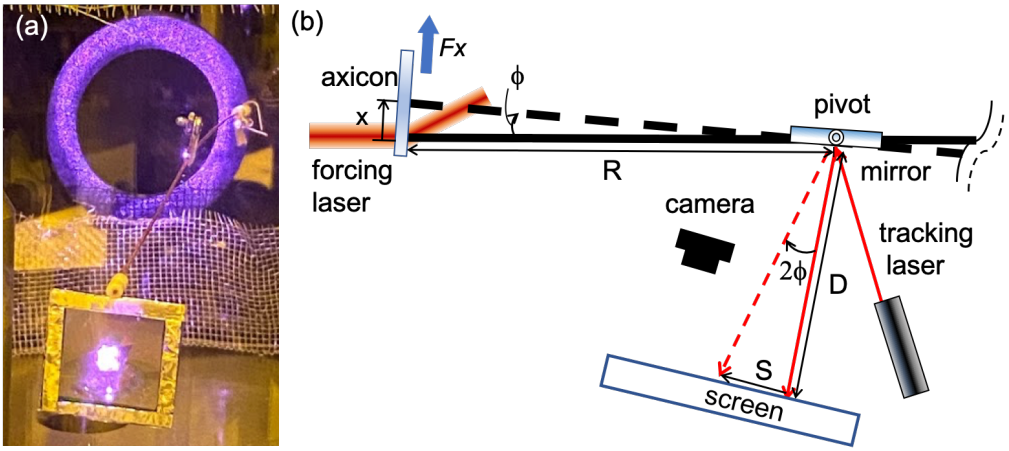

Figure 5.12: (a) Front view of the laser beam on the square axicon mounted on the torsion pendulum in a vacuum bell jar. The circular diffraction is reflected from the far side of the vacuum bell jar. (b) Torsion pendulum top view schematic.

arm of length $2R = 0.22$ [m], the tungsten filament, and conducting support structures. The axicon and a counterweight were mounted at the two ends of the torsion arm, with the suspension filament (pivot) at the mid-point (see Fig. 5.12). Motion was effectively constrained to one horizontal degree of freedom, with vertical see-saw motion stiff and readily damped, and motion along the beam axis unperturbed by radiation pressure owing to the comparatively large gravitational force on the system. Angular deviations $\phi(t)$ of a low power tracking laser reflected from a small low mass mirror at the pivot point were recorded to obtain the transverse displacement, x, of the axicon relative to the stationary forcing laser via the small angle relations $\phi \approx x/R \approx S/2D$, where $D = 1.75$ [m] is the distance from the mirror to the recording screen and S is the linear beam displacement from equilibrium on the screen. For adequate sampling, roughly 19 measurements of x were recorded per oscillation period.

The horizontal displacement of the axicon may be represented by a forced damped

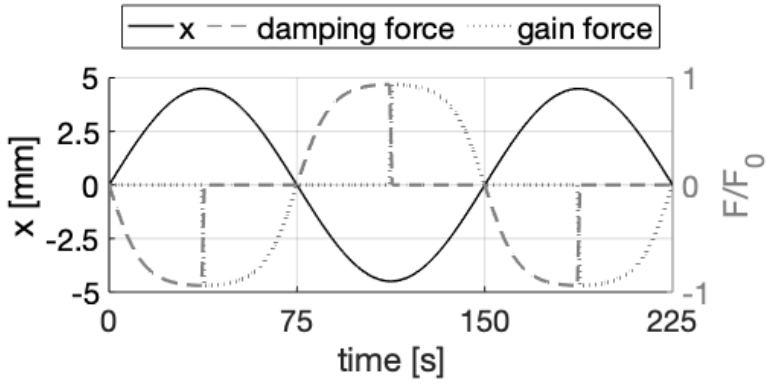

Figure 5.13: The parametric damping(dashed) and gain (dotted) force with respect to the phases of the axicon beam-rider oscillation$x$.

harmonic oscillator:

$$Jd^2x/dt^2 + 2(J/\tau_0)dx/dt + kx(t) = R^2\,F_x(t), \tag{5.12}$$

where $J = 1.3 \times 10^{-5}$ [kg $\cdot$ m^2] is the calculated moment of inertia, $k = (2\pi/T_0)^2 J = 2.2\times10^{-8}$[N$\cdot$m/rad] is the torsional stiffness of the tungsten filament, $T_0 = (152.0\pm0.1)$ [s] is the measured natural oscillation period when $F_x(t) = 0$, and $\tau_0 = (657.8 \pm 65.8)\,T_0$ is the measured natural decay time. For small displacements $|x| << w$ we expect the radiation pressure force to increase the torsional stiffness value from k to $k + \tilde{k}_{rp}R^2$, resulting in a 1.9% smaller oscillation period [34]. The moment of inertia of the pendulum is determined from $J = M_bR^2/3 + M_c(w_c^2+d_c^2)/12 + M_aR^2+M_{cb}R_{cb}^2$, with torsion bar mass $M_b = 0.38$ [g]; pivot mass, width and thickness $M_c = 1.05$ [g], $w_c = 5$ [mm] and $d_c = 1$ [mm]; axicon assembly mass $M_a = 0.50$ [g] at distance $R = 110$ [mm]; counter balance mass $M_{cb} = 0.52$ [g] at distance $R_{cb} = 106$ [mm]. The total mass suspended from the tungsten filament

is $M_{tot} = 2.45$ [g]. As stated above, the component of radiation pressure force along the beam path is negligible, displacing the hanging mass by less than $\Delta z \approx 2P_i L_f/cmg = 0.1$ [μm].

To enhance the effects of radiation pressure and provide a larger signal than that obtained by a small frequency shift, we made use of a parametric oscillator model whereby the forcing laser power was abruptly changed four times per oscillator period, allowing the amplitude of oscillation to increase or decrease over time. Parametric damping was recently reported in Ref. [34] for a linear bi-grating. An axicon grating provides the advantage of parametric control in two transverse directions. The large vertical stiffness of our apparatus prohibited us from demonstrating simultaneous two-dimensional control; instead we made separate measurements with the axicon mounted at two different orientations. Owing to the symmetry of the axicon the measurements were nearly indistinguishable.

Parametric damping (gain) of the axicon was experimentally verified by shuttering the forcing laser on and off, depending on the value of the product $x(t) \cdot v(t)$ where $v = \partial x/\partial t$ is the velocity of the axicon. Accordingly the radiation pressure force was modulated, as graphically illustrated in Fig. 5.13:

$$F_x(t) = \begin{cases} -F_0 \tanh(x/w) & \text{if } \sigma x(t) \cdot v(t) > 0 \\ 0 & \text{if } \sigma x(t) \cdot v(t) \leq 0 \end{cases} \tag{5.13}$$

where $\sigma = 1$ ($\sigma = -1$)for parametric damping (gain). To our knowledge a closed form solution of $x(t)$ for Eq.s 5.12, 5.13 does not exist. However, for weak parametric loss or gain, we found the measured displacement could be characterized by the function $x(t) \approx x_0 \exp(-t/\tau_{\mathrm{d,meas}}) \cos(2\pi t/T)$, where $\tau_{\mathrm{d,meas}}$ is the experimentally observed decay time

and x_0 is the oscillation amplitude at time $t = 0$.

For the case of parametric damping the decay time decreased from the free oscillation value of $\tau_0 = 10^5$ [s] to $\tau_{\mathrm{d,meas}} = (8.2 \pm 0.4) \times 10^3$[s] for motion parallel to the x_s axis, and $(9.2 \pm 0.5) \times 10^3$[s]) for motion parallel to the y_s direction. The y_s measurement was made by rotating the axicon by 90° so that the y_s sample axes was parallel x axis of the laboratory. We therefore achieved a damping rate roughly 11.5 times faster than the natural decay rate.

Combining Eq.s 5.12, 5.13 and making use of numerical integration, we predicted a shorter theoretical parametric decay rate of $\tau_{\mathrm{d,para}} \approx 4.4 \times 10^3$ [s]. We attribute the difference in measured and theoretical values to the errors in the on/off switching times which introduces an effective dephasing effect. We therefore set

$$1/\tau_{\mathrm{d,meas}} = 1/\tau_{\mathrm{d,para}} - 1/\tau_{\mathrm{d,deph}} + 1/\tau_0 \tag{5.14}$$

where $\tau_{\mathrm{d,para}}$ is the decay time owing to the precise time-varying force defined by Eq. 5.13 and $\tau_{\mathrm{d,deph}} \approx 8.0 \times 10^3$ [s] is the characteristic time attributed to the confounding effect of dephasing.

Parametric damping followed by parametric gain via modulated radiation pressure according to the scheme described in Eq. 5.13 (see also Fig. 5.13) is illustrated in Fig. 5.14. Here we instituted a systematic change from parametric damping ($t < 6000$ [s]) to free oscillation, and then to parametric gain ($t > 8000$ [s]), demonstrating the ease at which gain and decay may be activated. The magnitude of the experimentally measure gain rate was small than the numerical model predicted. As above the measured gain may be expressed by Eq. 5.14 after replacing the decay subscript (d) with a gain subscript

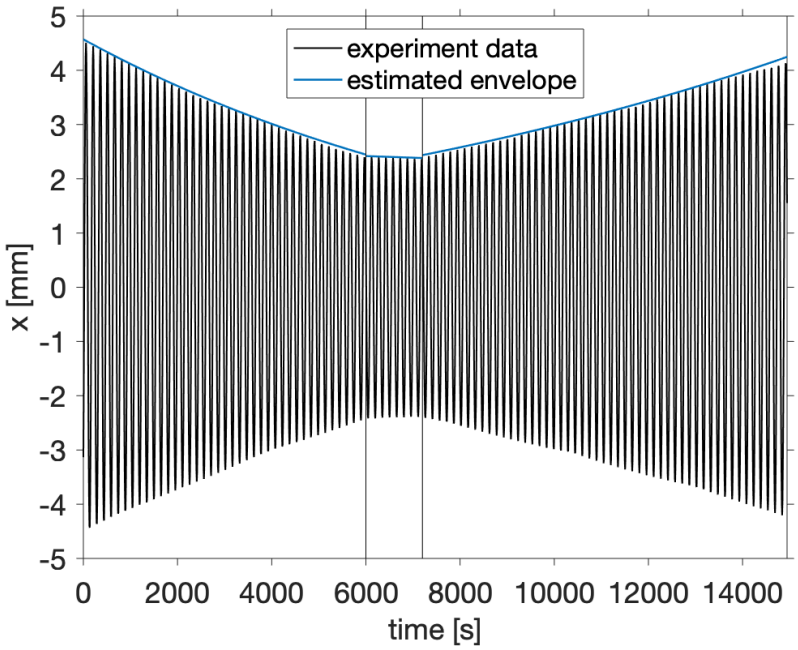

Figure 5.14: Radiation pressure induced parametric damping, followed by a pause, and then parametric amplification on the experimental torsion-oscillator-mounted axicon.

(g). The measured gain time was $\tau_{\mathrm{g,meas}} = (-13.9 \pm 0.1) \times 10^3$ [s], and the corresponding dephasing and parametric gain times were $\tau_{\mathrm{g,para}} \approx -4.0 \times 10^3$ [s] and $\tau_{\mathrm{g,deph}} \approx -6 \times 10^3$ [s].

In general we expect the dynamical motion to depend on both the ratio w/L as well as the amplitude of displacement, as suggested by Fig. 5.11. The measured displacements for the case $w/L = 0.29$ reported above did not exceed $x_{\max} = 4.5$ [mm], resulting in quasi-linear results. A complete analysis of the dynamical motion for other parameter values is beyond the scope of this Letter. Future work, however, should explore the displacement $x(t)$ as the beam size $w(t)$ increases with time, as would occur if the sail were accelerated in space along the axis of an expanding diffracted beam. An examination of Fig. 5.11 suggests that a significantly diminished restoring force is expected when the

beam overfills the sail. Methods to implement strong parametric damping during the stage when $w/L < 1$ (before the beam overfill the sail) should be explored to ensure that the sail does not wander from its desired trajectory.

In summary a miniature version of a laser-driven light sail comprised of an axicon grating has been shown to exhibit the transverse restoring force required of a full scale beam-riding light sail. A small magnitude of the transverse component of force, (~ 0.2 nano-Newtons) was found to be sufficient to excite parametric gain and damping. In principle parametric force modulation may also be achieved by use of an active electro-optically controlled grating, e.g., by use of a space-variant liquid crystal film [110,137,151], in which case on-board accelerometers could provide the required control signals. By describing the convolutional relationship between radiation pressure force and relative displacement of the beam and sail, we conclude that a laser-driven light sail may be readily controlled when the beam underfills the sail, i.e., where there is a significant restoring force.

5.3.1 Estimating the power of parametric damping

The measured decay(gain) time τ_{meas} does not equate to the damping(amplification) effects from time-modulated optical radiation pressure. We may use the damping(gain) time τ_{RP} to describe the damping effects solely by parametric damping from radiation pressure. In a real experiment, the de-phasing of the time modulation switching points may add a counter effect on the damping(gain) time. We consider the de-phasing of time modulation as a damping term described by τ_{dephase}, which may be incorporated into the equation of motion and considered as an effective damping term, τ_0^{eff}, instead of the vacuum damping.

$$\frac{1}{\tau_{\text{meas}}} = \frac{1}{\tau_0^{\text{eff}}} + \frac{1}{\tau_{\text{RP}}} \text{ , where } \frac{1}{\tau_0^{\text{eff}}} = \frac{1}{\tau_0} - \frac{1}{\tau_{\text{dephase}}} \tag{5.15}$$

The effective equation of motion may be written:

$$Jd^2x(t)/dt^2 + 2(J/\tau_0^{\text{eff}})dx/dt + kx = F_xR^2 \tag{5.16}$$

We estimate the value for τ_0^{eff} by matching the numerical solution to the experimentally measured oscillation data. With the value for τ_0^{eff} estimated, calculated value for τ_{RP} and τ_{dephase} using Eq. 5.15 is recorded in Table 5.2. Four total measurements are made, including three parametric damping and one parametric gain.

decay time [s]	τ_{meas}	τ_{dephase}	τ_{RP}
Parametric Damping	8.2E3	-8E3	4.2E3
	9.2E3	-7.5E3	4.3E3
	9.6E3	-8.5E3	4.7E3
Parametric Gain	-13.9E3	6E3	-4.0E3

Table 5.2: Calculated with J=1.3E-5

Chapter 6

Conclusion

Here we offer a final discussion summarizing the contribution of the dissertation's work on the research and science advancements of measuring radiation pressure on diffractive films, as well as the idea of using modern diffractive optical materials for light sail space propulsion. We follow with some recommendations from the author regarding experimental development and future experiments, such as a potential to demonstrate "pulling force".

6.1 Contribution Summary

The experimental measurement of radiation pressure on a grating served as an unprecedented verification for the idea of "grating momentum", which was viewed only symbolically in literature for Fourier Diffractive Theorems. Radiation pressure component tangential to the surface of a grating was verified to be independent of the incident angle and dominated by the constant grating momentum ($\mathbf{K} = 2\pi/\Lambda$). Near-zero force normal

to the grating was also demonstrated around Littrow-configuration ($\theta_1 = \pi - \theta_{in}$), in contrast to the zero tangential force on a purely reflective mirror surface where force was most widely studied. We also verified that momentum transfer on a grating is proportional to the grating diffractive order m.

The verification of radiation pressure force on diffractive films set foundation for diffractive light sails, and also stimulated ideas in emerging fields of study for refractive sails, meta-material sails, photonic crystal sails, all sharing a similar goal to bend light in different ways to produce both tangential and normal component of force to the sail surface. Our experiments show that to observe a large tangential force component, it is important to have a large diffractive angle, and to suppress higher diffractive orders as well as any other optical losses so that incident beam power diffracts into a single order. Therefore, high efficiency single-order diffraction gratings are sought after, which is achieved in modern advanced diffractive structures. Eyeing also the future needs of electo-optically switchable sails, liquid crystal Cycloidal Diffractive Waveplates (CDWs) in the form of light-weight diffractive films, with theoretically 100% diffractive efficiency in a single order serves as a strong candidate for diffractive sails. We developed a bi-grating sturcture with side-by-side grating panels of opposite diffractive orders with CDWs, and used it to experimentally verify the idea of a "diffractive beam-rider", which added to the feasibility of an diffractive light sail. Another strong candidate, mutli-level flat grating which could be made by single grayscale lithography exposure, is used to design and fabricate an axicon radial grating and experimentally demonstrated to provide restoring force along the two-dimensional plane. The demonstration of bi-grating and axicon beam riders both offered a strong solution to dampen the drifting of a light sail and from a propulsion beam path.

The torsional pendulum system, grounded with a long rod and soft torsion stiffness constructed in vacuum for this dissertation is successful in providing displacement observation in light-sail prototypes. It provided meso-scopic measurements of tangential displacements in a laboratory setting with sub nano-Newton sensitivity, compared to MEMS devices and AFMs that measure forces in pico-Newtons. The system enabled the demonstration of parametric cooling on one and two-dimensional diffractive beam-rider.

6.2 Experimental Recommendations

Two-Mode Pendulum for Horizontal and Vertical Motion

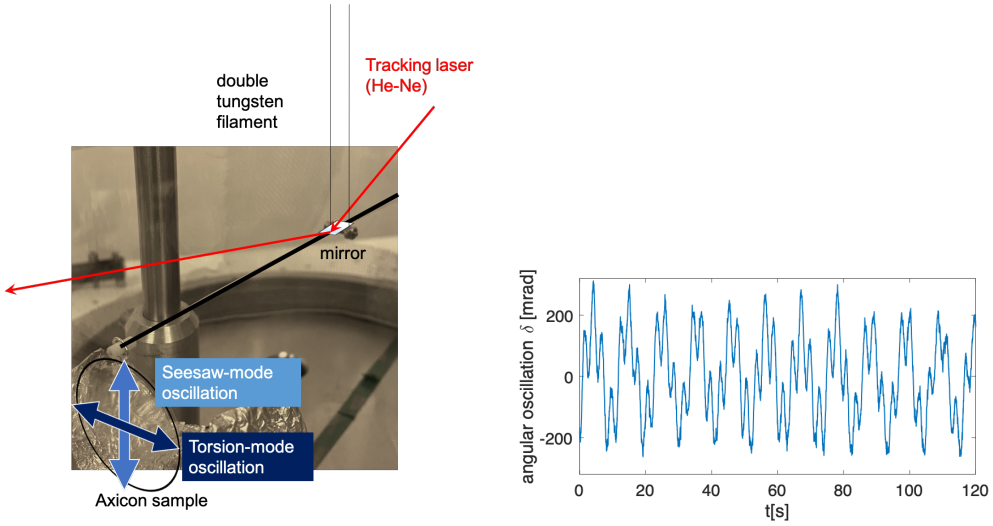

Figure 6.1: (a) A photo of a two-mode pendulum setup. (b) The recorded motion of a two-mode pendulum.

Here I provide a documentation of an attempt to develop an oscillator with the capability to exhibit motions along two degrees of freedom. The two-mode pendulum wasn't

implemented due to its unequal sensitivity across the two axes. I call mode 1 as "torsion mode" and mode 2 as "see-saw mode", which corresponds to the horizontal motion of the sample respectively. The measured period T_1=10.4[s] and T_2=2.7[s] indicates $k_1 = 6.8 \times 10^{-7}$ [Nm/rad] and $k_2 = 1.7 \times 10^{-4}$ [Nm/rad] for their respective moment of inertia $J_1 = 1.9 \times 10^{-6}$ [kg-m^2] and $J_2 = 3.13 \times 10^{-5}$ [kg-m^2]. The stiffness of $k_1$and k_2 are three orders of magnitude different, despite different central hanging mechanisms, including the bi-filar configuration that is shown in 6.1.

This configuration was developed to verify the restoring force on an axicon, or possibly any tangential force to the surface that does not limit to one degree of freedom. For an axicon beam-rider structure, it may be possible under this configuration, to still take a way energy via parametric damping, by shuttering the laser beam in when radial displacement and radial velocity $r \cdot r' > 0$, and shuttering the laser beam off when $r \cdot r' \leq 0$. However, it is not practical to demonstrate torsion pendulum stiffening, since the three orders of magnitude difference in k_1 and k_2 would cause the radiation pressure induced stiffness to be negligible in the vertical direction (k_2).

Demonstrating Pulling Force on a Diffractive Film

Future perspectives of this work involves demonstrating radiation pressure on modern "gratings" such as meta-materials as well as CDWs and grayscale flat diffractive optics. Different forms of radiation pressure, not only the tangential forces are of interest. For example, a beam-combining configuration may provide a "pulling" force as a tractor beam.

Figure 6.2 shows a reverse setup of a flat beam-splitter surface, where instead of having an incident beam splitting into two directions, two beams come in at opposite angles and combine to one. Two incident beams under-fill the surface, with incident k-vectors

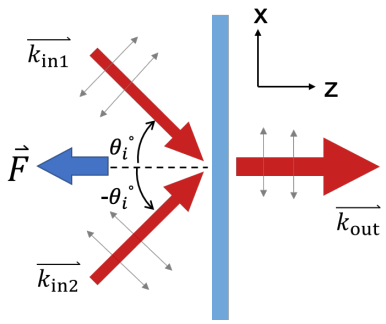

Figure 6.2: Incident and output k-vectors into a reverse beam-splitter resulting in an attractive force.

described as

$$\vec{k}_{in1} = 0.5P_i/c\ (-\sin\theta_i\hat{x} + \cos\theta_i\hat{z}) \tag{6.1a}$$

$$\vec{k}_{in2} = 0.5P_i/c\ (\sin\theta_i\hat{x} + \cos\theta_i\hat{z}), \tag{6.1b}$$

where P_i is the beam power of the laser, c is the speed of light, θ_i is the incident angle. The out-coming beam vector is then

$$\vec{k}_{out} = \eta P_i/c\ \hat{z} \tag{6.2}$$

where $\eta = P_{out}/P_i$ is the beam-combining efficiency, P_{out} is the power of the combined beam. The resulting radiation pressure force "attracts" the beam along the combined beam axis $\hat{z}$

$$\vec{F} = P_i/c(\cos\theta_i - \eta)\hat{z}, \tag{6.3}$$

for example if $\theta_i = 50°$, $\cos\theta_i = 0.64$ and $\eta = 0.9$, $\vec{F} = -0.26(P_i/c)\ \hat{z}$. An example experimental setup to measure this pulling force is shown in Fig. 6.3. This setup is

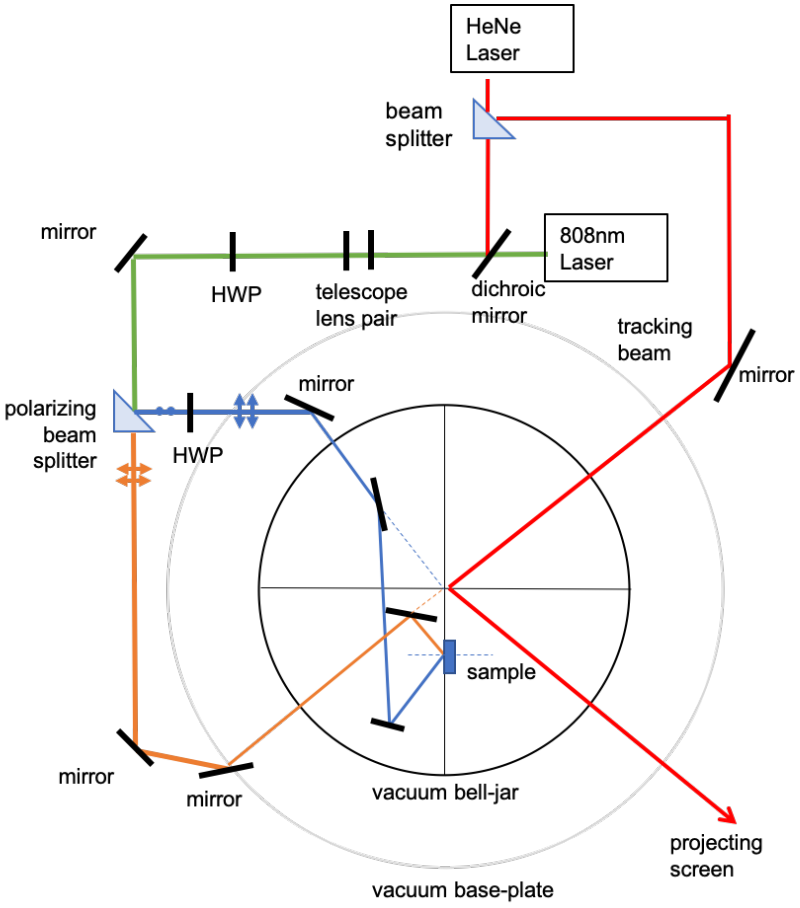

Figure 6.3: Top view cartoon example experiment design to demonstrate pulling force on a torsion pendulum in a vacuum belljar.

designed to have both incident beam polarization parallel to the plane of incidence (TM polarization), and normally incident to the vacuum bell-jar. To achieve this, the single forcing laser (808nm, 10W) is first split into two beams of even power with TM and TE polarizations respectively (shown as orange and blue rays) with a polarizing beam cube. Since the reflected beam out of the beam cube becomes TE polarized, a half wave-plate is placed on the beam path to ensure a TM polarization. A red, He-Ne laser is used both to track the oscillation motion, and also as an alignment laser which combines to the forcing laser beam path with a dichroic mirror.

Bibliography

[1]

[2] Breakthrough Starshot. https://breakthroughinitiatives.org/initiative/3. [Online; accessed 25-July-2021].

[3] New mission will take 1st peek at suns poles. https://www.nasa.gov/feature/goddard/2020/new-mission-will-take-first-peek-at-sun-s-poles. Accessed: 2021-05-26.

[4] Space Flight 101. Lightsail-a satellite overview. http://spaceflight101.com/spacecraft/lightsail-a/. (Accessed on 04/13/2019).

[5] Max Abraham. Zur elektrodynamik bewegter körper. *Rendiconti del Circolo Matematico di Palermo (1884-1940)*, 28(1):1–28, 1909.

[6] K Achouri, HC Wang, and OJF Martin. Optical force control using phase-gradient metasurfaces. In *2018 12th International Congress on Artificial Materials for Novel Wave Phenomena (Metamaterials)*, pages 007–009. IEEE, 2018.

[7] Karim Achouri and Christophe Caloz. Metasurface solar sail for flexible radiation pressure control. *arXiv preprint arXiv:1710.02837*, 2017.

[8] Karim Achouri, Mohamed A Salem, and Christophe Caloz. General metasurface synthesis based on susceptibility tensors. *IEEE Transactions on Antennas and Propagation*, 63(7):2977–2991, 2015.

[9] TR Albrecht, Pr Grütter, D Horne, and D Rugar. Frequency modulation detection using high-q cantilevers for enhanced force microscope sensitivity. *Journal of Applied Physics*, 69(2):668–673, 1991.

[10] Altechna. Plano-convex axicons. `https://www.altechna.com/products/plano-convex-axicons/`. Accessed on 2021-06-04.

[11] Viktar S Asadchy, Mohammad Albooyeh, Svetlana N Tcvetkova, Ana Díaz-Rubio, Younes Ra'di, and SA Tretyakov. Perfect control of reflection and refraction using spatially dispersive metasurfaces. *Physical Review B*, 94(7):075142, 2016.

[12] Viktar S Asadchy, Ana Díaz-Rubio, and Sergei A Tretyakov. Bianisotropic metasurfaces: physics and applications. *Nanophotonics*, 7(6):1069–1094, 2018.

[13] Theodor Asavei, Vincent LY Loke, Marco Barbieri, Timo A Nieminen, Norman R Heckenberg, and Halina Rubinsztein-Dunlop. Optical angular momentum transfer to microrotors fabricated by two-photon photopolymerization. *New Journal of Physics*, 11(9):093021, 2009.

[14] Arthur Ashkin. Acceleration and trapping of particles by radiation pressure. *Physical review letters*, 24(4):156, 1970.

[15] Arthur Ashkin, James M Dziedzic, JE Bjorkholm, and Steven Chu. Observation of a single-beam gradient force optical trap for dielectric particles. *Optics letters*, 11(5):288–290, 1986.

[16] Harry A Atwater, Artur R Davoyan, Ognjen Ilic, Deep Jariwala, Michelle C Sherrott, Cora M Went, William S Whitney, and Joeson Wong. Materials challenges for the starshot lightsail. *Nature materials*, 17(10):861–867, 2018.

[17] Chathura P Bandutunga, Paul G Sibley, Michael J Ireland, and Robert L Ward. Photonic solution to phase sensing and control for light-based interstellar propulsion. *JOSA B*, 38(5):1477–1486, 2021.

[18] Gregory Benford, Olga Gornostaeva, and James Benford. Experimental tests of beam-riding sail dynamics. In *AIP Conference Proceedings*, volume 664, pages 325–335. American Institute of Physics, 2003.

[19] Michael W Berns, Yona Tadir, Hong Liang, and Bruce Tromberg. Laser scissors and tweezers. In *Methods in cell biology*, volume 55, pages 71–98. Elsevier, 1997.

[20] Richard A Beth. Mechanical detection and measurement of the angular momentum of light. *Physical Review*, 50(2):115, 1936.

[21] M Bhattacharya and Pierre Meystre. Trapping and cooling a mirror to its quantum mechanical ground state. *Phys. Rev. Lett.*, 99(7):073601, 2007.

[22] Space Studies Board, National Research Council, et al. *Solar and space physics: A science for a technological society*. National Academies Press, 2013.

[23] David J Braun. Optimal parametric feedback excitation of nonlinear oscillators. *Phys. Rev. Lett.*, 116(4):044102, 2016.

[24] David L Brundrett, Elias N Glytsis, and Thomas K Gaylord. Normal-incidence guided-mode resonant grating filters:design and experimental demonstration. *Optics Letters*, 23(9):700–702, 1998.

[25] EN Bulgakov, DN Maksimov, PN Semina, and SA Skorobogatov. Propagating bound states in the continuum in dielectric gratings. *Journal of the Optical Society of America B.*, 35(6):1218–1222, 2018.

[26] Carlos Bustamante, Steven B Smith, Jan Liphardt, and Doug Smith. Single-molecule studies of dna mechanics. *Current opinion in structural biology*, 10(3):279–285, 2000.

[27] Eugene Butikov. A physically meaningful new approach to parametric excitation and attenuation of oscillations in nonlinear systems. *Nonlinear Dyn.*, 02 2017.

[28] Eugene I Butikov. Pendulum with a square-wave modulated length. *Int. J. Nonlinear. Mech.*, 55:25–34, 2013.

[29] Hans-Jürgen Butt, Brunero Cappella, and Michael Kappl. Force measurements with the atomic force microscope: Technique, interpretation and applications. *Surface science reports*, 59(1-6):1–152, 2005.

[30] Michelle D Chabot, John M Moreland, Lan Gao, Sy-Hwang Liou, and Casey W Miller. Novel fabrication of micromechanical oscillators with nanoscale sensitivity at room temperature. *Journal of Microelectromechanical systems*, 14(5):1118–1126, 2005.

[31] Haiwei Chen, Yishi Weng, Daming Xu, Nelson V. Tabiryan, and Shin-Tson Wu. Beam steering for virtual/augmented reality displays with a cycloidal diffractive waveplate. *Opt. Express*, 24(7):7287–7298, Apr 2016.

[32] Hsien Hui Cheng, Achintya K Bhowmik, and Philip J Bos. Concept for a transmissive, large angle, light steering device with high efficiency. *Optics letters*, 40(9):2080–2083, 2015.

[33] Ying-Ju Lucy Chu, Eric M. Jansson, and Grover A. Swartzlander. Measurements of radiation pressure owing to the grating momentum. *Phys. Rev. Lett.*, 121:063903, Aug 2018.

[34] Ying-Ju Lucy Chu, Nelson V. Tabiryan, and Grover A. Swartzlander. Experimental verification of a bigrating beam rider. *Phys. Rev. Lett.*, 123:244302, Dec 2019.

[35] Tina Clausnitzer, T Kämpfe, E-B Kley, A Tünnermann, Ulf Peschel, AV Tishchenko, and Olivier Parriaux. An intelligible explanation of highly-efficient diffraction in deep dielectric rectangular transmission gratings. *Optics Express*, 13(26):10448–10456, 2005.

[36] Pierre-François Cohadon, Antoine Heidmann, and Michel Pinard. Cooling of a mirror by radiation pressure. *Phys. Rev. Lett.*, 83(16):3174, 1999.

[37] Gregory P Crawford, James N Eakin, Marc D Radcliffe, Andrew Callan-Jones, and Robert A Pelcovits. Liquid-crystal diffraction gratings using polarization holography alignment techniques. *Journal of Applied Physics*, 98(12):123102, 2005.

[38] William Crookes. On attraction and repulsion resulting from radiation. *Philosophical transactions of the Royal society of London*, 164:501–527, 1874.

[39] Patricia Daukantas. Breakthrough starshot. *Optics and Photonics News*, 28(5):26–33, 2017.

[40] Artur R. Davoyan, Jeremy N. Munday, Nelson Tabiryan, Grover A. Swartzlander, and Les Johnson. Photonic materials for interstellar solar sailing. *Optica*, 8(5):722–734, May 2021.

[41] Jean Jacques de Mairan. *Traité physique et historique de l'aurore boréale.* De l'Imprimerie royale, 1754.

[42] K Dholakia and T Čižmár. Shaping the future of manipulation. *Nature photonics*, 5(6):335, 2011.

[43] Alan D. Kathman Dennis W. Prather Donald C. O'Shea, Thomas J. Suleski. *Diffractive Optics: Design, Fabrication, and Test.* SPIE Press Book, 2003.

[44] Arnau Farré and Mario Montes-Usategui. A force detection technique for single-beam optical traps based on direct measurement of light momentum changes. *Optics express*, 18(11):11955–11968, 2010.

[45] Furqan M Fazal and Steven M Block. Optical tweezers study life under tension. *Nature photonics*, 5(6):318, 2011.

[46] Shahin Firuzi and Shengping Gong. Refractive sail and its applications in solar sailing. *Aerospace Science and Technology*, 2018.

[47] Robert L Forward. Roundtrip interstellar travel using laser-pushed lightsails. *Journal of Spacecraft and Rockets*, 21(2):187–195, 1984.

[48] Augustin Fresnel. Note sur la repulsion que des corps échauffés execent sur les autres à des distances sensible. In *Annales de Chimie et de Physique*, volume 29, pages 57–62, 1825.

[49] Matthew C Friedenberg and C Mathew Mate. Dynamic viscoelastic properties of liquid polymer films studied by atomic force microscopy. *Langmuir*, 12(25):6138–6142, 1996.

[50] Louis Friedman and Mitch Gould. Starsailing: Solar sails and interstellar space travel. *Phys. Today*, 41:99, 1988.

[51] Robert H Frisbee. Limits of interstellar flight technology. *Frontiers of Propulsion Science*, 227:31–126, 2009.

[52] K. T. Gahagan and G. A. Swartzlander. Optical vortex trapping of particles. *Opt. Lett.*, 21(11):827–829, Jun 1996.

[53] Lucien P Ghislain, Neil A Switz, and Watt W Webb. Measurement of small forces using an optical trap. *Review of Scientific Instruments*, 65(9):2762–2768, 1994.

[54] Jan Gieseler, Bradley Deutsch, Romain Quidant, and Lukas Novotny. Subkelvin parametric feedback cooling of a laser-trapped nanoparticle. *Phys. Rev. Lett.*, 109(10):103603, 2012.

[55] GT Gillies and RC Ritter. Torsion balances, torsion pendulums, and related devices. *Review of scientific instruments*, 64(2):283–309, 1993.

[56] Paul Gilster. *Centauri dreams: imagining and planning interstellar exploration.* Springer Science & Business Media, 2004.

[57] David G Grier. A revolution in optical manipulation. *Nature*, 424(6950):810–816, 2003.

[58] Davide Guzzetti, Rohan Sood, Loic Chappaz, and Hexi Baoyin. Stationkeeping analysis for solar sailing the l 4 region of binary asteroid systems. *Journal of Guidance, Control, and Dynamics*, 42(6):1306–1318, 2019.

[59] Satoshi Hasegawa, Haruyasu Ito, Haruyoshi Toyoda, and Yoshio Hayasaki. Diffraction-limited ring beam generated by radial grating. *OSA Continuum*, 1(2):283–294, 2018.

[60] Christopher Hertlein, Laurent Helden, Andrea Gambassi, Siegfried Dietrich, and Clemens Bechinger. Direct measurement of critical casimir forces. *Nature*, 451(7175):172, 2008.

[61] Gareth W Hughes, Malcolm Macdonald, Colin R McInnes, Alessandro Atzei, and Peter Falkner. Sample return from mercury and other terrestrial planets using solar sail propulsion. *Journal of spacecraft and rockets*, 43(4):828–835, 2006.

[62] Ognjen Ilic and Harry A Atwater. Self-stabilizing photonic levitation and propulsion of nanostructured macroscopic objects. *Nature Photonics*, 13(4):289–295, 2019.

[63] Grace Jesensky, Dominic Dams, Oleksiy Khomenko, and Woo-Joong Kim. A simple table-top experiment demonstrating mechanical oscillation of a macroscopic object driven by radiation pressure. In *APS March Meeting Abstracts*, 2016.

[64] Weiliang Jin, Wei Li, Meir Orenstein, and Shanhui Fan. Inverse design of lightweight broadband reflector for relativistic lightsail propulsion. *ACS Photonics*, 7(9):2350–2355, 2020.

[65] L Johnson. Solar sails: Sneaking up on interstellar travel. *Journal of the British Interplanetary Society*, 68:44–47, 2015.

[66] Les Johnson. Solar sails for spacecraft propulsion. `https://ntrs.nasa.gov/archive/nasa/casi.ntrs.nasa.gov/20160005683.pdf`. (Accessed on 04/13/2019).

[67] Les Johnson, Mark Whorton, Andy Heaton, Robin Pinson, Greg Laue, and Charles Adams. Nanosail-d: A solar sail demonstration mission. *Acta Astronautica*, 68(5):571–575, 2011.

[68] Alex A Karwas. *An Unconditionally Stable Method for Numerically Solving Solar Sail Spacecraft Equations of Motion*. PhD thesis, University of Kansas, 2015.

[69] Satoshi Kawata and T Tani. Optically driven mie particles in an evanescent field along a channeled waveguide. *Optics letters*, 21(21):1768–1770, 1996.

[70] UF Keyser, J Van der Does, C Dekker, and NH Dekker. Optical tweezers for force measurements on dna in nanopores. *Review of Scientific Instruments*, 77(10):105105, 2006.

[71] Roman Ya Kezerashvili. Preface. solar sailing: Concepts, technology, and missions. *Advances in Space Research*, 48:1683–1686, 2011.

[72] Jihwan Kim, Matthew N Miskiewicz, Steve Serati, and Michael J Escuti. Nonmechanical laser beam steering based on polymer polarization gratings: design optimization and demonstration. *Journal of Lightwave Technology*, 33(10):2068–2077, 2015.

[73] Herbert J Kramer. *Observation of the Earth and its Environment: Survey of Missions and Sensors*. Springer Science & Business Media, 2002.

[74] Michael W. Kudenov, Michael J. Escuti, Eustace L. Dereniak, and Kazuhiko Oka. White-light channeled imaging polarimeter using broadband polarization gratings. *Appl. Opt.*, 50(15):2283–2293, May 2011.

[75] Philippe Lalanne, Simion Astilean, Pierre Chavel, Edmond Cambril, and Huguette Launois. Blazed binary subwavelength gratings with efficiencies larger than those of conventional échelette gratings. *Optics letters*, 23(14):1081–1083, 1998.

[76] Philippe Lalanne, Simion Astilean, Pierre Chavel, Edmond Cambril, and Huguette Launois. Design and fabrication of blazed binary diffractive elements with sampling periods smaller than the structural cutoff. *JOSA A*, 16(5):1143–1156, 1999.

[77] Philippe Lalanne, Jean Paul Hugonin, and Pierre Chavel. Optical Properties of Deep Lamellar Gratings: A Coupled Bloch-Mode Insight. *J. Lightwave Technol.*, 24(6):2442, Jun 2006.

[78] Geoffrey A Landis. Optics and materials considerations for a laser-propelled lightsail. *Proc. 40th Congress of the International of the International Astronautical Federation*, IAA-89-664, 1989.

[79] MA Lantz, SJ Oshea, and ME Welland. Force microscopy imaging in liquids using ac techniques. *Applied physics letters*, 65(4):409–411, 1994.

[80] PN Lebedev. Investigations on the pressure forces of light. *Ann. Phys*, 6:433–458, 1901.

[81] Kye-Sung Lee and Jannick P Rolland. Bessel beam spectral-domain high-resolution optical coherence tomography with micro-optic axicon providing extended focusing range. *Optics letters*, 33(15):1696–1698, 2008.

[82] Yun-Han Lee, Guanjun Tan, Tao Zhan, Yishi Weng, Guigeng Liu, Fangwang Gou, Fenglin Peng, Nelson V Tabiryan, Sebastian Gauza, and Shin-Tson Wu. Recent progress in pancharatnam–berry phase optical elements and the applications for virtual/augmented realities. *Optical Data Processing and Storage*, 3(1):79–88, 2017.

[83] PC Liewer, RA Mewaldt, JA Ayon, and RA Wallace. Nasas interstellar probe mission. *AIP Conference Proceedings*, 504(1):911–916, 2000.

[84] Shiyun Lin, Ethan Schonbrun, and Kenneth Crozier. Optical manipulation with planar silicon microring resonators. *Nano letters*, 10(7):2408–2411, 2010.

[85] Fenfei Liu, Seyedhamidreza Alaie, Zayd C Leseman, and Mani Hossein-Zadeh. Sub-pg mass sensing and measurement with an optomechanical oscillator. *Optics express*, 21(17):19555–19567, 2013.

[86] EG Loewen, Maystre Nevière, and D Maystre. Grating efficiency theory as it applies to blazed and holographic gratings. *Applied optics*, 16(10):2711–2721, 1977.

[87] R Loudon and C Baxter. Contributions of john henry poynting to the understanding of radiation pressure. *Proceedings of the Royal Society A: Mathematical, Physical and Engineering Sciences*, 468(2143):1825–1838, 2012.

[88] P Lubin. A roadmap to interstellar flight. *Journal of the British Interplanetary Society*, 69:40–72, 2016.

[89] Jun Luo, Qi Liu, Liang-Cheng Tu, Cheng-Gang Shao, Lin-Xia Liu, Shan-Qing Yang, Qing Li, and Ya-Ting Zhang. Determination of the newtonian gravitational constant g with time-of-swing method. *Physical review letters*, 102(24):240801, 2009.

[90] Dakang Ma and Jeremy N Munday. Measurement of wavelength-dependent radiation pressure from photon reflection and absorption due to thin film interference. *Scientific reports*, 8, 2018.

[91] Dakang Ma, Joseph Murray, and Jeremy N Munday. Controllable propulsion by light: steering a solar sail via tunable radiation pressure. *Advanced Optical Materials*, 5(4):1600668, 2017.

[92] Zachary Manchester and Abraham Loeb. Stability of a light sail riding on a laser beam. *The Astrophysical Journal Letters*, 837(2):L20, 2017.

[93] I Manek, Yu B Ovchinnikov, and R Grimm. Generation of a hollow laser beam for atom trapping using an axicon. *Optics communications*, 147(1-3):67–70, 1998.

[94] Shoji Maruo, Akira Takaura, and Yohei Saito. Optically driven micropump with a twin spiral microrotor. *Optics Express*, 17(21):18525–18532, 2009.

[95] George Marx. Interstellar vehicle propelled by terrestrial laser beam. *Nature*, 211(5044):22, 1966.

[96] Anatoly V Masalov. First experiments on measuring light pressure i (translated from pyotr nikolaevich lebedev). In *Quantum Photonics: Pioneering Advances and Emerging Applications*, pages 425–453. Springer, 2019.

[97] James Clerk Maxwell. *A treatise on electricity and magnetism*, volume 1. Clarendon press, 1881.

[98] Colin R McInnes. *Solar Sailing: Technology, Dynamics and Mission Applications*. Springer-Verlag, 2004.

[99] Colin R McInnes. *Solar sailing: technology, dynamics and mission applications*. Springer Science & Business Media, 2013.

[100] John H McLeod. The axicon: a new type of optical element. *JOSA*, 44(8):592–597, 1954.

[101] Leslie McNutt, Les Johnson, Dennon Clardy, Julie Castillo-Rogez, Andreas Frick, and Laura Jones. Near-earth asteroid scout. `https://ntrs.nasa.gov/archive/nasa/casi.ntrs.nasa.gov/20140012882.pdf`, publisher=American Institute of Aeronautics and Astronautics, note = (Accessed on 04/13/2019).

[102] Monjurul Meem, Apratim Majumder, and Rajesh Menon. Multi-plane, multi-band image projection via broadband diffractiveoptics. *Appl. Opt.*, 59(1):38–44, Jan 2020.

[103] Michael Metcalfe. Applications of cavity optomechanics. *Applied Physics Reviews*, 1(3):031105, 2014.

[104] Hermann Minkowski. Die grundgleichungen für die elektromagnetischen vorgänge in bewegten körpern. *Nachrichten von der Gesellschaft der Wissenschaften zu Göttingen, Mathematisch-Physikalische Klasse*, 1908:53–111, 1908.

[105] Cristina Mio, T Gong, A Terray, and DWM Marr. Morphological control of mesoscale colloidal models. *Fluid Phase Equilibria*, 185(1-2):157–163, 2001.

[106] Pritiraj Mohanty, Darrell A Harrington, and Michael L Roukes. Measurement of small forces in micron-sized resonators. *Physica B: Condensed Matter*, 284:2143–2144, 2000.

[107] Daniel Müller, OC St Cyr, Ioannis Zouganelis, Holly R Gilbert, R Marsden, T Nieves-Chinchilla, E Antonucci, Frédéric Auchère, D Berghmans, TS Horbury, et al. The solar orbiter mission-science overview. *Astronomy & Astrophysics*, 642:A1, 2020.

[108] Sarik R Nersisyan, Nelson V Tabiryan, Landa Hoke, Diane M Steeves, and Brian Kimball. Polarization insensitive imaging through polarization gratings. *Optics Express*, 17(3):1817–1830, 2009.

[109] Sarik R Nersisyan, Nelson V Tabiryan, Diane M Steeves, and Brian R Kimball. The promise of diffractive waveplates. *Optics and Photonics News*, 21(3):40–45, 2010.

[110] SR Nersisyan, NV Tabiryan, DM Steeves, and BR Kimball. Optical axis gratings in liquid crystals and their use for polarization insensitive optical switching. *Journal of Nonlinear Optical Physics & Materials*, 18(01):1–47, 2009.

[111] SR Nersisyan, NV Tabiryan, DM Steeves, and BR Kimball. The principles of laser beam control with polarization gratings introduced as diffractive waveplates. In *Liquid Crystals XIV*, volume 7775, page 77750U. International Society for Optics and Photonics, 2010.

[112] Ernest Fox Nichols and Gordon Ferrie Hull. A preliminary communication on the pressure of heat and light radiation. *Physical Review (Series I)*, 13(5):307, 1901.

[113] Ernest Fox Nichols and Gordon Ferrie Hull. The pressure due to radiation.(second paper.). *Physical Review (Series I)*, 17(1):26, 1903.

[114] Andrey Novitsky, Cheng-Wei Qiu, and Haifeng Wang. Single gradientless light beam drags particles as tractor beams. *Physical Review Letters*, 107(20):203601, 2011.

[115] University of Surrey. About cubesail. `https://www.surrey.ac.uk/surrey-space-centre/missions/cubesail`. (Accessed on 04/13/2019).

[116] Chulwoo Oh. *Broadband polarization gratings for efficient liquid crystal display, beam steering, spectropolarimetry, and Fresnel zone plate*. North Carolina State University, 2009.

[117] Chulwoo Oh and Michael J Escuti. Achromatic diffraction from polarization gratings with high efficiency. *Optics letters*, 33(20):2287–2289, 2008.

[118] NASA Mission Pages. Solar sail demonstrator (sunjammer). `https://www.nasa.gov/mission_pages/tdm/solarsail/index.html`. (Accessed on 04/13/2019).

[119] Darwin Palima, Andrew Rafael Bañas, Gaszton Vizsnyiczai, Lóránd Kelemen, Thomas Aabo, Pál Ormos, and Jesper Glückstad. Optical forces through guided light deflections. *Optics express*, 21(1):581–593, 2013.

[120] Shivaramakrishnan Pancharatnam. Achromatic combinations of birefringent plates. In *Proceedings of the Indian Academy of Sciences-Section A*, volume 41, pages 137–144. Springer, 1955.

[121] Kevin LG Parkin. The breakthrough starshot system model. *Acta Astronautica*, 152:370–384, 2018.

[122] Alessandro Peloni, Matteo Ceriotti, and Bernd Dachwald. Solar-sail trajectory design for a multiple near-earth-asteroid rendezvous mission. *Journal of Guidance, Control, and Dynamics*, pages 2712–2724, 2016.

[123] Carl Pfeiffer and Anthony Grbic. Metamaterial huygens surfaces: tailoring wave fronts with reflectionless sheets. *Physical review letters*, 110(19):197401, 2013.

[124] The planetary society. Lightsail- flight by light for cubesats. `http://www.planetary.org/explore/projects/lightsail-solar-sailing/`. (Accessed on 04/13/2019).

[125] Elena Popova, Messoud Efendiev, and Ildar Gabitov. On the stability of a space vehicle riding on an intense laser beam. *Mathematical Methods in the Applied Sciences*, 40(4):1346–1354, 2017.

[126] JH Poynting. Xvi. note on the tangential stress due to light incident obliquely on an absorbing surface. *The London, Edinburgh, and Dublin Philosophical Magazine and Journal of Science*, 9(49):169–171, 1905.

[127] Cheng-Wei Qiu, Darwin Palima, Andrey Novitsky, Dongliang Gao, Weiqiang Ding, Sergei V Zhukovsky, and Jesper Gluckstad. Engineering light-matter interaction for emerging optical manipulation applications. *Nanophotonics*, 3(3):181–201, 2014.

[128] O Ren and Reginald Birngruber. Axicon: a new laser beam delivery system for corneal surgery. *IEEE journal of quantum electronics*, 26(12):2305–2308, 1990.

[129] Marc Rioux, R Tremblay, and Pierre-Andre Belanger. Linear, annular, and radial focusing with axicons and applications to laser machining. *Applied Optics*, 17(10):1532–1536, 1978.

[130] B. Rodenburg, L. P. Neukirch, A. N. Vamivakas, and M. Bhattacharya. Quantum model of cooling and force sensing with an optically trapped nanoparticle. *Optica*, 3(3):318–323, Mar 2016.

[131] Gerald Roosen and Christian Imbert. Absolute measurement of laser beam energy using its radiation pressure force. *Optical Engineering*, 20(3):203437, 1981.

[132] I. Ryger, A. B. Artusio-Glimpse, P. Williams, N. Tomlin, M. Stephens, K. Rogers, M. Spidell, and J. Lehman. Micromachined force scale for optical power measurement by radiation pressure sensing. *IEEE Sens. J.*, 18(19):7941–7948, Oct 2018.

[133] Ivan Ryger, Alexandra B Artusio-Glimpse, Paul Williams, Nathan Tomlin, Michelle Stephens, Kyle Rogers, Matthew Spidell, and John Lehman. Micromachined force scale for optical power measurement by radiation pressure sensing. *IEEE Sensors Journal*, 18(19):7941–7948, 2018.

[134] Mohammad Mahdi Salary and Hossein Mosallaei. Photonic metasurfaces as relativistic light sails for doppler-broadened stable beam-riding and radiative cooling. *Laser & Photonics Reviews*, 14(8):1900311, 2020.

[135] H Sarkissian, B Park, N Tabirian, and B Zeldovich. Periodically aligned liquid crystal: potential application for projection displays. *Molecular Crystals and Liquid Crystals*, 451(1):1–19, 2006.

[136] Keiji Sasaki, Hideki Fujiwara, and Hiroshi Masuhara. Optical manipulation of a lasing microparticle and its application to near-field microspectroscopy. *Journal of Vacuum Science & Technology B: Microelectronics and Nanometer Structures Processing, Measurement, and Phenomena*, 15(6):2786–2790, 1997.

[137] Svetlana V Serak, David E Roberts, Jeoung-Yeon Hwang, Sarik R Nersisyan, Nelson V Tabiryan, Timothy J Bunning, Diane M Steeves, and Brian R Kimball. Diffractive waveplate arrays. *JOSA B*, 34(5):B56–B63, 2017.

[138] Bing Shao, Sadik C Esener, Jaclyn M Nascimento, Elliot L Botvinick, and Michael W Berns. Dynamically adjustable annular laser trapping based on axicons. *Applied optics*, 45(25):6421–6428, 2006.

[139] Joel Siegel, Anthony Y Wang, Sergey G Menabde, Mikhail A Kats, Min Seok Jang, and Victor Watson Brar. Self-stabilizing laser sails based on optical metasurfaces. *ACS Photonics*, 6(8):2032–2040, 2019.

[140] Steven B Smith, Yujia Cui, and Carlos Bustamante. optical-trap force transducer that operates by direct measurement of light momentum. In *Methods in enzymology*, volume 361, pages 134–162. Elsevier, 2003.

[141] Prateek R Srivastava, Ying-Ju Lucy Chu, and Grover A Swartzlander. Stable diffractive beam rider. *Opt. Lett.*, 44(12):3082–3085, 2019.

[142] Prateek R Srivastava and Grover A Swartzlander. Optomechanics of a stable diffractive axicon light sail. *The European Physical Journal Plus*, 135(7):1–16, 2020.

[143] S Sukhov and A Dogariu. On the concept of "tractor beams". *Optics Letters*, 35(22):3847–3849, 2010.

[144] S Sukhov and A Dogariu. Negative nonconservative forces: optical "tractor beams" for arbitrary objects. *Physical Review Letters*, 107(20):203602, 2011.

[145] Grover Swartzlander, Les Johnson, and Bruce Betts. Light sailing into the great beyond. *Opt. Photon. News*, 31(2):30–37, Feb 2020.

[146] Grover A Swartzlander. Radiation pressure on a diffractive sailcraft. *JOSA B*, 34(6):C25–C30, 2017.

[147] Grover A Swartzlander. Radiation pressure on a diffractive sailcraft. *JOSA B*, 34(6):C25–C30, 2017.

[148] Grover A Swartzlander Jr. Flying on a rainbow: A solar-driven diffractive sailcraft. *J. Br. Interplanet. Soc.*, 71:130–132, 2018.

[149] Grover A Swartzlander Jr, Timothy J Peterson, Alexandra B Artusio-Glimpse, and Alan D Raisanen. Stable optical lift. *Nature Photonics*, 5(1):48, 2011.

[150] Randall T Swimm, Yiming Xiao, and Michael Bass. Calorimetric study of optical absorption of suprasil w-1 fused quart at visible, near-ir, and near-uv wavelengths. *Applied Optics*, 24(3):322–323, 1985.

[151] Nelson V Tabiryan, David E Roberts, Zhi Liao, Jeoung-Yeon Hwang, Mark Moran, Olena Ouskova, Andrii Pshenichnyi, Justin Sigley, Anna Tabirian, Rafael Vergara, et al. Advances in transparent planar optics: Enabling large aperture, ultrathin lenses. *Advanced Optical Materials*, 9(5):2001692, 2021.

[152] Yuki Takao, Osamu Mori, and Junichiro Kawaguchi. Self-excited oscillation of spinning solar sails utilizing solar radiation pressure. *Astrodynamics*, 4(3):177–192, 2020.

[153] Thorlabs. Diffraction gratings tutorial. `https://www.thorlabs.com/newgrouppage9.cfm?objectgroup_id=9026`. Accessed on 2020-07-29.

[154] YL Tian, Y Tu, and CG Shao. Correlation method in period measurement of a torsion pendulum. *Review of scientific instruments*, 75(6):1971–1974, 2004.

[155] Alexandre V Tishchenko and Alexey A Shcherbakov. General analytical solution for the electromagnetic grating diffraction problem. *Optics Express*, 25(12):13435–13447, 2017.

[156] DM Todorović. Photothermal and electronic elastic effects in microelectromechanical structures. *Review of scientific instruments*, 74(1):578–581, 2003.

[157] Engineering Toolbox. Modulus of elasticity or young's modulus - and tensile modulus for common materials. `https://www.engineeringtoolbox.com/young-modulus-d_417.html`. Accessed on 2017-12-21.

[158] Yuichi Tsuda, Osamu Mori, Ryu Funase, Hirotaka Sawada, Takayuki Yamamoto, Takanao Saiki, Tatsuya Endo, Katsuhide Yonekura, Hirokazu Hoshino, and Jun'ichiro Kawaguchi. Achievement of ikarosjapanese deep space solar sail demonstration mission. *Acta Astronautica*, 82(2):183–188, 2013.

[159] Yuichi Tsuda and IKAROS Demonstration Team. How ikaros shape is designed: Attitude stability of spinning solar sail. In *Advances in Solar Sailing*, pages 45–56. Springer, 2014.

[160] H Ueyama, Y Sugawara, and S Morita. Stable operation mode for dynamic noncontact atomic force microscopy. *Applied Physics A: Materials Science & Processing*, 66:S295–S297, 1998.

[161] Merel Vergaaij and Jeannette Heiligers. Solar-sail trajectory design to planetary pole sitters. *Journal of Guidance, Control, and Dynamics*, 42(6):1402–1412, 2019.

[162] L. Guillermo Villanueva, Rassul B. Karabalin, Matthew H. Matheny, Eyal Kenig, Michael C. Cross, and Michael L. Roukes. A nanoscale parametric feedback oscillator. *Nano Lett.*, 11(11):5054–5059, 2011.

[163] Jamie Vovrosh, Muddassar Rashid, David Hempston, James Bateman, Mauro Paternostro, and Hendrik Ulbricht. Parametric feedback cooling of levitated optomechanics in a parabolic mirror trap. *J. Opt. Soc. Am. B*, 34(7):1421–1428, 2017.

[164] Giovanni Vulpetti, Les Johnson, and Greg Matloff. *Solar Sails: A Novel Approach to Interplanetary Travel*. Copernicus, 2008.

[165] Giovanni Vulpetti, Les Johnson, and Gregory L Matloff. *Solar sails: a novel approach to interplanetary travel*. Springer, 2014.

[166] Paul Williams, Joshua Hadler, Frank Maring, Robert Lee, Kyle Rogers, Brian Simonds, Matthew Spidell, Michelle Stephens, Ari Feldman, and John Lehman. Portable, high-accuracy, non-absorbing laser power measurement at kilowatt levels by means of radiation pressure. *Optics express*, 25(4):4382–4392, 2017.

[167] Paul A Williams, Joshua A Hadler, Robert Lee, Frank C Maring, and John H Lehman. Use of radiation pressure for measurement of high-power laser emission. *Optics letters*, 38(20):4248–4251, 2013.

[168] Jerome L Wright. *Space sailing*. Taylor & Francis, 1992.

[169] Tao Wu, Timo A Nieminen, Samarendra Mohanty, Jill Miotke, Ronald L Meyer, Halina Rubinsztein-Dunlop, and Michael W Berns. A photon-driven micromotor can direct nerve fibre growth. *nature photonics*, 6(1):62, 2012.

[170] CW Zöllner. *Das Lehrgebäude der Volks-Wirthschaft.* Theobald Grieben, 1877.

Appendices

Appendix A

Radiation Pressure Force on Diffracted Photon

The momentum of a single photon of wavelength λ is given by the vector $\hbar\vec{k}$ where $k = 2\pi/\lambda$ is the magnitude of the wave vector, $c = \omega/k$ is the speed of light, and ω is the angular frequency. The energy of the photon is given by $E = \hbar\omega = \hbar ck$. A packet of N such photons passing through a plane over a time Δt carries a net momentum $N\hbar\vec{k}$. If the packet is elastically deflected by a material in another direction characterized by the wave vector $\vec{k'}$, the net momentum changes to $N\hbar\vec{k'}$. From Newton's third law, the force on the material is therefore

$$\vec{F} = \hbar N(\vec{k} - \vec{k'})/\Delta t = (P/ck)(\vec{k} - \vec{k'}) \tag{A.1}$$

where $P = EN/\Delta t$ is the power of the beam of photons.

If instead the packet is elastically deflected in multiple directions, each characterized by

a wave vector $\vec{k}_m$ and energy $N_m\hbar\omega$, where conservation of energy provides $\sum_m N_m = N$, then the above argument may be generalized:

$$\vec{F} = \hbar(N\vec{k} - \sum_m N_m\vec{k}_m)/\Delta t \tag{A.2a}$$

$$= (EN/ck)(\vec{k} - \sum_m (N_m/N)\vec{k}_m)/\Delta t \tag{A.2b}$$

$$= (P/ck)(\vec{k} - \sum_m \eta_m\vec{k}_m) \tag{A.2c}$$

where $\eta_m = N_m/N$ is the efficiency of scattering into the $\vec{k}_m$ direction. Conservation of energy and elastic scattering requires $\sum_m \eta_m = 1$ and the power of the m^{th} beam is $P_m = N_m E/\Delta t = \eta_m P$.

Appendix B

Momentum and Energy Transfer from Photon to Object

In Appendix A we consider the radiation pressure force on a material solely by the net photon momentum change. The definitions of photon momentum and energy are also provided in Appendix A. Here we consider the momentum transfer from an incident photon with momentum $\hbar\vec{k}$ on to an object with mass m and initially moving with velocity of $\vec{v}$ along $\hat{z}$- direction in Fig. B.1 (a). After the light hits the object, photon get reflects

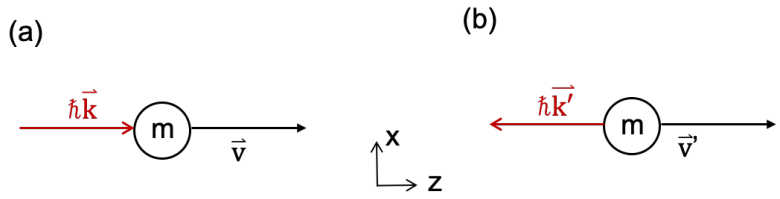

Figure B.1: Initial and final photon momentum of $\hbar\vec{k}$ and $\hbar\vec{k}'$for a momentum transfer to an object with mass m with initial and final velocity of $\vec{v}$ and $\vec{v}'$.

towards $-\hat{z}$ direction with the momentum $\hbar\vec{k}'$, and the object velocity becomes $\vec{v}'$, as in Fig.B.2. (b). The motion of this momentum transfer is all along the single dimension of $\hat{z}$.

If the object was still $\vec{v}$=0 before the momentum transfer, from the conservation of momentum $mv + \hbar k = mv' - \hbar k'$, we obtain

$$\hbar(k + k') = mv'. \tag{B.1}$$

From the conservation of energy $(1/2)mv^2 + \hbar ck = (1/2)mv'^2 + \hbar ck'^2$, we obtain

$$\hbar c(k - k') = (1/2)mv'^2. \tag{B.2}$$

Combining both Equations B.1 and B.2, we may express the velocity that the object picked up from the photon

$$v' = -c \pm c\ (1 + 4\hbar ck/mc^2), \tag{B.3}$$

where for a photon with wavelength $\lambda = 1 \times 10^{-6}$[m], $\hbar c = 3 \times 10^{-26}$[J-m], $k = 2\pi/\lambda$, and an object of 1 gram $m = 10^{-3}$[kg], we take the positive velocity $v' \approx 2.4 \times 10^{-24}$[m/s].

The energy transfer from the incident photon to the kinetic energy of the object may be defined as an energy transfer ratio of $\zeta = (1/2)mv'^2/\hbar ck = 1.5 \times 10^{-32}$, which is so small it could be ignored. We could consider $N = 10^{32}$ incident photons, where one would need to shine a 100 GW laser for 200 seconds such that the total incident energy $E = N\hbar ck = 2 \times 10^{13}$[J] , and the kinetic energy transferred to an 1 gram object is only a minor portion $E'_{obj} = E\zeta = 3 \times 10^{-19}$[J], resulting $v' = 2.5 \times 10^{-8}$[m/s]. Plugging the value of ζ back into Eq. (B.2), we may also deduct $k \approx k'$that the wave number (wavelength)

change could be ignored in this process.

Therefore, it is safe to use the expressions provided in Appendix A, where radiation pressure can be determined solely by the incident and final photon momentum vectors, $k = k'$ was assumed, and the effect on the object was ignored. Using Eq. (A.1) with the values above (P=100 [GW] for the duration of 200 seconds, $\lambda = 1 \times 10^{-6}$[m], $m = 10^{-3}$[kg]), we can determine radiation pressure force $F = 0.1$N, acceleration $a = F/m = 100$ m/s^2 , and the still object undergoing this acceleration will reach $v' = 1/2at^2 = 2 \times 10^6$[m/s] in 200 seconds. This calculation provide proof and validation for the scale of the laser power, duration, and speed that are considered in laser sail projects.